REPORT DOCUMENTATION PAGE

Form Approved
OMB No. 0704-0188

AD-A231 834

2. Report Date.	3. Report Type and Dates Covered.
31 Aug 1988	Contract Report 31 Aug 1988

Application Of Acoustic Signal Processing Techniques For Improved Underwater Source Detection And Localization

5. Funding Numbers.
Program Element No. 0602435N
Project No. 3502
Task No. JOB
Accession No. DN259007

6. Author(s).
Dr. George E. Ioup, Dr. Juliette W. Ioup and
Dr, Grayson H. Rayborn

7. Performing Organization Name(s) and Address(es).
Department of Physics, University of New Orleans
Department of Physics and Astronomy, University of Southern Mississippi

8. Performing Organization Report Number.
CR N00014-87-K-6002

9. Sponsoring/Monitoring Agency Name(s) and Address(es).
Naval Ocean R&D Activity/Office of Naval Res rch
Room 528-Federal Building
300 East 8th Street
Austin, Texas 78701-3273

10. Sponsoring/Monitoring Agency Report Number.

11. Supplementary Notes.

12a. Distribution/Availability Statement.
Approved for public release; Distribution is unlimited.

12b. Distribution Code.

13. Abstract *(Maximum 200 words).*

14. Subject Terms.
normal mode filtering and nonorthogonality, deformed hydrophone array performance

15. Number of Pages.
102

16. Price Code.

17. Security Classification of Report.	18. Security Classification of This Page.	19. Security Classification of Abstract.	20. Limitation of Abstract.
Unclassified	Unclassified		

APPLICATION OF ACOUSTIC SIGNAL PROCESSING TECHNIQUES FOR IMPROVED UNDERWATER SOURCE DETECTION AND LOCALIZATION

U.S. DEPARTMENT OF THE NAVY CONTRACT NUMBER N00014-87-K-6002

FINAL REPORT

31 Aug 1988

Dr. George E. Ioup, Principal Investigator
Dr. Juliette W. Ioup, Principal Investigator
Department of Physics
University of New Orleans
New Orleans, LA 70148

Dr. Grayson H. Rayborn, Principal Investigator
Department of Physics and Astronomy
University of Southern Mississippi
Hattiesburg, MS 39401

APPLICATION OF ACOUSTIC SIGNAL PROCESSING TECHNIQUES FOR IMPROVED UNDERWATER SOURCE DETECTION AND LOCALIZATION

The subject contract was issued to the University of New Orleans (UNO) from 13 Jan 1987 through 31 Aug 1988. Drs. George and Juliette Ioup served as Principal Investigators. A subcontract was issued to the University of Southern Mississippi (USM), where Dr. Grayson Rayborn served as Principal Investigator. At UNO Mr. Ken Barnes was hired as a Research Associate, and Mr. George Frichter was hired as a Research Assistant. During the period of performance the Principal Investigators were also supported as Navy/ASEE Senior Summer Faculty Fellows. Parts of the research summarized in this report were performed on these appointments.

Much of the research performed for the contract has been reported at national meetings and/or written up in manuscript form for publication. A listing of these items follows. Beside each is noted whether a copy is included with this Final Report. For each item not included with this report, information is given on the availability of the document.

1. Grayson H. Rayborn, George E. Ioup, Juliette W. Ioup, and Janet C. Carr, "Normal-mode filtering with orthogonal functions to avoid mode leakage," paper presented to the Acoustical Society of America, Anaheim, CA, December 1986. Abstracted in J. Acous. Soc. Am. Suppl. 1, Vol. 80, S113 (1986).
This research was performed prior to the start of the contract, but it provides an introduction to the contract-supported research. A copy of this abstract is included in this report.

2. Deanna M. Caveny, Donald R. Del Balzo, Jeffrey L. Becklehimer, and George E. Ioup, "Performance of sinusoidally deformed line arrays," paper presented to the Acoustical Society of America, Anaheim, CA, December 1986. Abstracted in J. Acous. Soc. Am. Suppl. 1, Vol. 80, S26 (1986).

This research was performed prior to the start of the contract, but it provides an introduction to the contract-supported research. A copy of this abstract is included in this report.

3. Deanna M. Caveny, Donald R. Del Balzo, Jeffrey L. Becklehimer, and George E. Ioup, "Array shape estimation via piecewise subarray beamforming," paper presented to the Acoustical Society of America, Anaheim, CA, December 1986. Abstracted in J. Acous. Soc. Am. Suppl. 1, Vol. 80, S26 (1986).

This research was performed prior to the start of the contract, but it provides an introduction to the contract-supported research. A copy of this abstract is included in this report.

4. Grayson H. Rayborn, George E. Ioup, and Juliette W. Ioup, "Nonorthogonality of measured normal modes in shallow water," paper presented at the fall meeting of the Acoustical Society of America, November 1987, Miami, FL. Abstracted in J. Acous. Soc. Am. Suppl. 1, Vol. 82, S72 (1987).

A copy of this abstract is included in this report.

5. Juliette W. Ioup, George E. Ioup, Grayson H. Rayborn, Donald R. Del Balzo, and Christopher Feuillade, "Effects of measured mode nonorthogonality on conventional matched field processing," paper presented at the fall meeting of the Acoustical Society of America, November 1987, Miami, FL. Abstracted in J. Acous. Soc. Am. Suppl. 1, Vol. 82, S73 (1987).

A copy of this abstract is included in this report.

6. James H. Leclere, Donald R. Del Balzo, Deanna M. Caveny, George E. Ioup, Jeffrey L. Becklehimer, and Donald A. Murphy, "Performance of Sinusoidally Deformed Planar Arrays," paper presented to the Acoustical Society of America, Indianapolis, IN, May 1987. Abstracted in J. Acous. Soc. Am. Suppl. 1, Vol 81, S85 (1987).

A copy of this abstract is included in this report.

7. Effects of Noise on Pressure and Modal Amplitude Matched Field Processing, George M. Frichter, IV, Juliette W. Ioup, George B. Smith, George E. Ioup, Christopher Feuillade, Grayson H. Rayborn, Donald Del Balzo, paper presented at the March Meeting of the American Physical Society, 21-25 Mar 1988, New Orleans, abstracted in Bull. Am. Phys. Soc. 33, 705 (1988).

A copy of this abstract is included in this report.

8. Least-squares and single-filter always-convergent iterative deconvolution of transient signals for correlation processing, James H. Leclere, George E. Ioup, Juliette W. Ioup, and Robert L. Field, paper presented at the fall meeting of the Acoustical Society of America, 14-18 Nov 1988, Honolulu, HI, and abstracted in Jour. Acous. Soc. Am. 84, S17 (1988).

This paper reports work completed and submitted for a conference during the contract period, but the paper will not be presented until after the expiration of the contract. A copy of the abstract is included in this report.

9. Comparison of double and triple cross correlation for arrival time identification of amplitude- and frequency-modulated acoustic transient signals, Juliette W. Ioup, George E. Ioup, Robert L. Field, and James H. Leclere, paper presented at the fall meeting of the Acoustical Society of America, 14-18 Nov 1988, Honolulu, HI, and abstracted in Jour. Acous. Soc. Am. 84, S17 (1988).

This paper reports work completed and submitted for a conference during the contract period, but the paper will not be presented until after the expiration of the contract. A copy of the abstract is included in this report.

10. Deanna M. Caveny, George E. Ioup, Donald R. Del Balzo, and James H. Leclere, "Performance Evaluation of Sinusoidally Deformed Hydrophone Arrays," manuscript submitted to Jour. Acoust. Soc. Am., June, 1988.

This manuscript has been accepted for publication subject to revision. A copy of the

manuscript in its current form is included in this report.

11. Grayson H. Rayborn, George E. Ioup, and Juliette W. Ioup, "Nonorthogonality of Measured Normal Modes in a Shallow Water Waveguide," manuscript submitted to Jour. Acoust. Soc. Am., May, 1988.
A copy of the manuscript is included with this report.

12. Juliette W. Ioup, George E. Ioup, Grayson H. Rayborn, Donald R. Del Balzo, and Christopher Feuillade, "Effects of measured mode nonorthogonality on conventional matched field processing," manuscript in preparation.
Copies of the manuscript in its current form are available from the Principal Investigators.

13. George M. Frichter, IV, 1987, Underwater Acoustic Pressure to Modal Amplitude Mapping for Wind Generated Noise ir a Waveguide, M. S. Thesis, University of New Orleans.
A copy of this thesis has been given to the Scientific Program Officer. Additional copies may be requested from Mr. Frichter or the Principal Investigators.

14. Weiping Pan, 1988, An Application of a Perturbative, Approximate Method to the Study of Sound Propagation by Normal Modes in Shallow Water, M. S. Thesis, University of Southern Mississippi.
Mr. Pan was not supported by contract funds, but his research was supervised by Dr. Rayborn during the contract period, and may be of interest. A copy has been supplied to the Scientific Program Officer. Additional copies are available.

15. Grayson H. Rayborn, A study of the literature of reverberation and scattering in a wedge environment and from wedges in a general ocean environment.
This report was written for and previously submitted to the replacement Scientific Program Officer, Dr. Anas Abo-Zena. A copy is included in this report.

16. James H. Leclere, Donald R. Del Balzo, and George E. Ioup, A Brief Introduction to BEAMSTATPAK with Sample Calculations of Array Performance on Multiple Line Systems.

This 47-page report was prepared for NORDA. A copy in draft form is available from the authors. The report is currently being expanded and revised to describe recent changes in BEAMSTATPAK by Dr. Rick Slater and Mr. Howard Chandler of NORDA.

Most of the research supported by this contract has been reported in the above listed publications. Smaller research projects which have been performed have been reported directly to the Scientific Program Officer. Funding will be sought by the Principal Investigators to continue research in promising areas in the future.

with free-falling ocean bottom seismometers (OBS). Since the ship's position and its towed signal sources (air gun, uniboom) or explosives are fairly well known based on high-precision navigation systems, one can determine the geophone positions indirectly from their response to the source excitation. Here, a newly developed source parameter estimation code [A. B. Baggeroer, W. A. Kuperman, and H. Schmidt, J. Acoust. Soc. Am. Suppl. 1 79, S56 (1986)] is first used to determine the performance bounds for a localization based on seismic interface waves. Then, an actual shear speed profile is determined by inversion of a new data set obtained using explosive sources, and a maximum-likelihood estimation of the geophone position is performed. By comparing the results with the actual experimental geometry, it is demonstrated that in spite of the fairly long wavelength of the interface waves, a reasonable resolution can be achieved by such a technique.

10:30

AAA9. Simulations of matched-field processing in a deep-water Pacific environment. Michael B. Porter, Ronald L. Dicus, and Richard Fizell (Code 5120, Naval Research Laboratory, Washington, DC 20375)

Matched-field processing is a signal processing technique for arrays in which field vectors for assumed source positions (range and depth) are substituted for plane-wave steering vectors in conventional linear and nonlinear beamformers. The field vectors are computed by standard acoustic field models (FFP, normal mode, etc.) which take into account propagation effects in an oceanic waveguide. The output is an ambiguity surface over possible source positions in which a peak is expected at the true source position. Accuracy of the computed fields is limited in large part by our knowledge of the environment. This environmental mismatch causes degradation in localization performance, sometimes leading to large errors in estimation of source position. In order to assess the significance of this effect, simulations were performed in which a measured field is synthesized using a slightly different environmental model from that used for the steering vectors. The differences were introduced to simulate expected errors in sound-speed profile, sediment thickness, and elastic wave speed. Calculations were made for a cw source operating at 10 Hz and depths of 25 and 250 m in a 500 m-deep ocean. The receiver was a 16-element vertical array at ranges of 25 (shadow zone) and 100 km (second convergence zone). A typical Pacific sound velocity profile was assumed. The bottom was modeled by a thin (50-m) sediment layer overlying an elastic subbottom. Degradation in localization performance due to environmental mismatch will be discussed both quantitatively and qualitatively.

10:45

AAA10. Preliminary results of matched-field localization using a vertical array in the Tufts Abyssal Plain. R. G. Fizell (Code 5120, Naval Research Laboratory, Washington, DC 20375)

PACIFIC ECHO was an experiment conducted jointly by the Naval Research Laboratory (NRL) and Defence Research Establishment, Pacific (DREP) in May–June 1986. Vertical array measurements of a 15-Hz cw signal projected by the NRL Mk-VI source, towed at a depth of 100 m on a circular arc of radius 3 nmi, were analyzed with matched-field processing. The DREP array was 675 m long with the top hydrophone at 400-m depth. Matched-field processing between theoretical and measured fields was accomplished by linear correlation and by a nonlinear maximum-likelihood method (MLM) estimator. Theoretical fields were computed using a normal-modes program, the measured sound velocity profile, and an assumed thick-sediment bottom. Successful localization of the source was achieved with both estimators. Sidelobes produced by the MLM estimator were significantly below the main peak but, for the linear estimator, sidelobes were sufficiently large to be taken as false targets.

11:00

AAA11. Sensitivity of the matched-field source localization technique in shallow water to mismatch of geoacoustic parameters. Donald R. Del Balzo (NORDA Code 244, NSTL, MS 39529), Christopher Feuillade, and Mary M. Rowe (ODSI Defense Systems, Inc., 6110 Executive Boulevard, Rockville, MD 20852)

The accuracy of matched-field techniques for source localization in a shallow-water waveguide is dependent upon realistic modeling of the geoacoustic environment. A study was conducted to investigate the sensitivity of source localization to erroneous estimates of the geoacoustic properties (sound speed, density, and attenuation) of the sediment. A range-independent normal-mode computer program was used to calculate acoustic fields from a midwater source received on a vertical array of 21 hydrophones spanning the water column. Errors in estimates of range and depth are presented as a function of mismatch of each geoacoustic property.

11:15

AAA12. Wave-height fluctuation effects on matched-field detection and localization in shallow water. Donald R. Del Balzo (NORDA Code 244, NSTL, MS 39529), Christopher Feuillade, and Mary M. Rowe (ODSI Defence Systems, Inc., 6110 Executive Boulevard, Rockville, MD 20852)

Sea surface wave-height fluctuations cause a time-dependent mismatch in environmental conditions and therefore effect the detection and localization performance of a matched-field processor. A sensitivity study was conducted to examine this mismatch phenomenon for an idealized, range-independent, Pekeris channel of 100-m depth, with a 150-Hz source, using a centrally positioned vertical array of 21 hydrophones spanning 50% of the water column. Variations in the sea surface height of + 3.5 m were considered as an extreme, but realistic, case, and the output signal-to-noise ratio (SNR) and predicted range and depth of the source were determined from a series of range-depth maximum-likelihood ambiguity surfaces. Surface height variation caused a systematic error in range estimation, such that when the depth was increased due to a wave crest, the target range appeared shorter than the actual range. The opposite held for a wave trough. The corresponding calculations of target depth were consistently biased towards greater depth. Calculations indicated that small (1%) variations in surface height can cause a loss of up to 15 dB in detection performance at a single time. However, when the computations are properly normalized and then averaged over time throughout a complete cycle of the wave-height variations, the resulting detection is dominated by the zero wave-height maximum-likelihood surface, and localization estimates based upon the position of the main peak are unambiguous.

11:30

AAA13. Normal-mode filtering with orthogonal functions to avoid mode leakage. Grayson H. Rayborn (Department of Physics and Astronomy, University of Southern Mississippi, Hattiesburg, MS 39406-5165 and NORDA, NSTL, MS 39529), George E. Ioup, Juliette W. Ioup (Department of Physics and Geophysical Research Laboratory, University of New Orleans, New Orleans, LA 70148 and NORDA, NSTL, MS 39529), and Janet C. Carr (NORDA, NSTL, MS 39529)

Propagation of sound in shallow water is commonly analyzed in terms of trapped normal modes. The process of normal-mode detection by adjustment of the response of individual hydrophones in a vertical array to match the pattern of a particular normal mode is normal-mode filtering. Despite the nonorthogonality of the normal modes in the water column, normal-mode filtering is based on the assumption that the modes are orthogonal. The error induced by this assumption is known as leakage. It has been estimated to range from 3% to 10% of a measured mode. In this paper, the error involved in treating the modes as orthogonal for a variety of bottom types, water depths, and source frequencies is analyzed, and a method for avoiding the error is demonstrated. Density and sound-speed ratios are selected from models fitted to experimentally measured values. To render the results indicative of a broad range of water depths and frequencies, use is made of dimensionless variables. Leakages as large as 19% are calculated.

result demonstrates that the sensitivity of the MHD transducer is just that given by the simple application of Faraday's law, in contrast to recent measurements indicating otherwise [P. H. Moose and R. F. Klaus, J. Acoust. Soc. Am. 74, 1066 (1983)]. This reciprocity technique should be applicable to calibration of a wide range of transducers, including hydrophones and accelerometers. [Work supported by the Office of Naval Research.]

2:00

L3. Design model of large, uniform, conformal arrays of bender bar and flextensional transducers. G. A. Brigham (Aquasonics, Inc., Anaheim, CA 92806)

The single element design technology of flextensional and bender bar transducers is several decades old but use of either type of transducer in conformal arrays presents newer and more formidable design problems. When the array is very large the effects of edge diffraction on the outer elements can be ignored to generate a zeroth ordered waveguide design model to estimate radiation loading at any steering angle. Highly eccentric shelled flextensionals and bender bar transducers are then included in one common format. Since both types are largely flexural, they are resonant at frequencies where the interelement spacing is much smaller than a wavelength in water and only the low-frequency inertial and plane-wave volume flow components of loading need be determined. Several array geometries have been studied and the reactive loadings calculated. This paper shows both the theoretical and numerical results of various mass loadings as functions of array and element geometry. [Research supported by the Naval Underwater Systems Center, New London; the Naval Ocean Systems Center, San Diego; the Electric Boat Division of General Dynamics.]

2:15

L4. Analysis of radiating flexural shell sonar transducers using the finite element method. B. Hamonic, J. C. Debus, J. N. Decarpigny (Institut Supérieur d'Electronique du Nord, 41 boulevard Vauban, 59046 Lille Cedex, France), D. Boucher, and B. Tocquet[a] (Groupe d'Etude et de Recherche de Détection Sous-Marine, Le Brusc, 83140 Six Fours les Plages, France)

New flexural shell transducers for low-frequency applications are currently developed which are characterized by a large volume velocity and a drastic reduction of their resonance frequencies as soon as they are flooded, due to added mass effect. To design these transducers, a finite element modeling is very useful, because it can accurately handle the assembling of three-dimensional and shell parts in the same structure, the piezoelectric driving force, the fluid–structure interaction as well as the radiation damping. This paper describes the analysis of a test axisymmetric transducer with the ATILA code [J. N. Decarpigny *et al.*, J. Acoust. Soc. Am. 78, 1499 (1985)] using dipolar damping elements and a new extrapolation method to obtain the transducer farfield characteristics [R. Bossut *et al.*, J. Acoust. Soc. Am. Suppl. 1 79, S51 (1986)]. In-air resonance modes, transmitting voltage response and directivity patterns are computed and compared to measurements, displaying a satisfactory agreement. Finally, the modeling of a transducer that is built with a glass-reinforced plastic shell is described, and the corresponding problems and results are discussed. [a] Currently at Thomson-Sintra, Chemin des travails, 06802 Cagnes sur mer, France.

2:30

L5. Array shape estimation via piecewise subarray beamforming. Deanna M. Caveny, Donald R. Del Balzo, Jeffrey L. Becklehimer (NORDA, Code 244, NSTL, MS 39529), and George E. Ioup (Department of Physics and Geophysical Research Laboratory, University of New Orleans, New Orleans, LA 70148)

Deformation produced when towing a linear array can remove L–R ambiguities in conventional beam patterns, provided the beamformer knows the deformed array shape. In practice, however, this shape is usually unknown. Thus it is desirable to have a processor that determines the shape and uses this information to form the beams. A method which accomplishes this goal forms beams for subapertures separately assuming that they are approximately linear. A maximum likelihood estimation method [M. J. Hinich and W. Rule, J. Acoust. Soc. Am. 58, 1023–1029 (1975)] has previously been used to associate an angle with each of the subapertures. Given the subarray bearing angle they calculated a mean and a median to estimate the full array bearing angle. In this study, after the main angle was determined, using conventional methods, a piecewise linear array was constructed by placing the subarrays together with estimated correction angles. To test the performance of the approximated array shapes, beamforming was carried out using the new piecewise linear array and the modeled data for the original deformed array. Systematic errors were investigated as well as various methods for smoothing the piecewise linear array.

2:45

L6. Performance of sinusoidally deformed line arrays. Deanna M. Caveny, Donald R. Del Balzo, Jeffrey L. Becklehimer (NORDA, Code 244, NSTL, MS 39529), and George E. Ioup (Department of Physics and Geophysical Research Laboratory, University of New Orleans, New Orleans, LA 70148)

Previously it has been shown [M. J. Hinich and W. Rule, J. Acoust. Soc. Am. 58, 1023–1029 (1975); W. S. Hodgkiss, IEEE J. Ocean. Eng. OE-8, 120–130 (1983)] that deformations of towed arrays from a straight line shape can produce significant distortions in beam patterns and errors in bearing estimation if the beamforming assumes linearity. It has also been shown that a deformed array helps to remove left/right ambiguities in the beam patterns, provided the beamforming is done with the correct array configuration. In this work these two effects are studied for undamped and damped sinusoidally deformed arrays (as observed in practice) of one, two, and three half-cycles with relatively small array amplitudes. By use of fixed arc length separations along the array, the phone (x, y) coordinates are determined numerically for each sinusoidal shape. The complex pressure fields are modeled for sources at various locations. Then beamforming is carried out (1) with the known array configuration, and (2) assuming that the array is linear. Degradations resulting from assuming linearity and the ability to remove left/right ambiguities are discussed in terms of reduced gain, angular resolution, and bearing errors.

3:00

L7. On the design technology of the uncompensated class IV flextensional transducer. G. A. Brigham (Aquasonics, Inc., Anaheim, CA 92806)

The air-backed flextensional transducer is stress constrained both in the shell and the electromechanical bar driver. When Navy type III hard lead zirconate–titanate ceramic is used, the total amount of bar preload for depth and power cannot exceed 10 kpsi with allocation an interative process in the design. The math model consists of three radiating shell modes together with the bar end velocity at the shell–bar interface. The design starts with a stress analysis of shell and bar which yields the relative dimensions of both. These are input to (a) the shell–bar equation for mechanical resonance in water to get the shell major axis width, and (b) the resonant half-power bandwidth equation to get the shell length. All remaining parameters follow from the sizing, e.g., effective coupling, weight, and peak acoustic power. This paper shows the design sequence, the results for a uniform elliptic ring used as a baseline, and application to designing various flextensionals for several new major Navy sonar transmit array programs.

3:15

L8. Fringe counting demodulator for fiber optic interferometric sensors. C. M. Crooker and S. L. Garrett (Physics Department, Code 61 Gx, Naval Postgraduate School, Monterey, CA 93943)

A demodulation scheme for high sensitivity (1–10 krad regime) fiber optic interferometric sensors which is based on fringe rate has been developed. The technique is similar to that utilized in optical shaft encoders.

A wearable multichannel signal processor for stimulation of single-electrode cochlear implants has been field tested with two patients. Each channel in the processor, which is implemented in a digital signal processing chip, consists of a resonator followed by an instantaneous compressive nonlinearity. The channel outputs are digitally mixed for use with single-electrode implants. The resonators perform a spectral-to-temporal transformation of the input signal and the nonlinearities limit output level to emulate the response characteristics of normal auditory neurons. The resonator and nonlinearity parameters are adjusted to accommodate both the acoustic properties of speech sounds and the electrical dynamic range of the patient. Several processor configurations with different resonator and nonlinearity designs have been evaluated. The results of psychophysical tests, used to fit each processor configuration to the patient and measure speech performance in quiet and noise with each configuration, will be reported.

11:30

HH12. Backward and forward masking for direct electrical stimulation of the VIIIth nerve in two profoundly deaf subjects. L. J. Dent and B. S. Townshend (Stanford Electronics Laboratories, Stanford, CA 94305)

Two profoundly deaf multielectrode implant subjects were required to detect a probe signal (10 ms in duration) in a temporal gap between two pulse-train maskers (each 300 ms in duration). The detection threshold was measured for a probe centered temporally in the gap, as well as for a probe offset from center by up to 97.5%. Also presented were the pure backward and pure forward masking cases. Qualitatively, both subject's forward and backward masking functions approximated those observed for normal hearing subjects [L.L. Elliott, J. Acoust. Soc. Am. 34, 1116–1117 (1962)] in that forward masking decayed more gradually than backward masking as a function of probe-masker separation. Because mechanical (cochlear) contributions to masking [H. Duifhuis, J. Acoust. Soc. Am. 54, 1471–1488 (1973)] can be excluded in the case of direct VIIIth nerve stimulation, these data support the attribution of nonsimultaneous masking phenomena to VIIIth nerve or higher neural mechanisms. [Work supported by NIH.]

11:45

HH13. Channel interactions measured by forward-masked "place" tuning curves with multichannel electrical stimulation. Virginia M. Kirby (Hearing Research Laboratory, 270-4S-11, 3M Center, Saint Paul, MN 55144), David A. Nelson (Hearing Research Laboratory, University of Minnesota, Minneapolis, MN 55455), Sigfrid D. Soli (Hearing Research Laboratory, 270-4S-11, 3M Center, Saint Paul, MN 55144), and Todd W. Fortune (Hearing Research Laboratory, University of Minnesota, Minneapolis, MN 55455)

Simultaneous stimulation of multichannel intracochlear electrodes can give rise to peripheral and central channel interactions. The ability to eliminate or predict and control the interactions produced by a given electrode geometry is a processing goal for optimizing performance with a multichannel cochlear implant. Previous studies have used *loudness* summation and forward-masking pattern techniques to estimate interactions between channels of electrical stimulation. In this study, interactions between bipolar channels of analog electrical stimulation were estimated using a forward-masking paradigm with a fixed-level, fixed-location probe. By varying the electrode location of a 200-Hz, 300-ms sinusoidal masker and determining the level of the masker at each location necessary to just mask a 200-Hz, 10-ms probe, a "*place*" tuning curve was derived. The level of masker required at a given location to mask the probe depends on the amount of excitation produced by the probe and reflects, in part, the degree to which there is overlap of neural populations responding to each stimulus. These "place" tuning curves, which display interactions as a function of masker location were determined for several probe levels and probe locations. Results and implications for speech processing strategies will be discussed.

THURSDAY MORNING, 19 NOVEMBER 1987 UMS 4 AND 5, 8:30 A.M. TO 12:00 NOON

Session II. Underwater Acoustics VI. Signal Processing for Underwater Acoustics (Précis-Poster Session)

Thomas G. Muir, Chairman
NATO SACLANT Centre, La Spezia, Italy

Chairman's Introduction—8:30

Contributed Papers

Following presentation of the précis, posters will be on display until 12:00 Noon.

8:35

II1. Nonorthogonality of measured normal modes in shallow water. Grayson H. Rayborn (Naval Ocean Research and Development Activity, NSTL, MS 39529-5004 and Department of Physics and Astronomy, University of Southern Mississippi, Hattiesburg, MS 39406), George E. Ioup, and Juliette W. Ioup (NORDA, NSTL, MS 39529 and Department of Physics and Geophysical Research Laboratory, University of New Orleans, New Orleans, LA 70148)

The importance of surmounting the nonorthogonality of measured normal modes and processing shallow-water data in such a way that modal compositions are effectively recovered for matched field processing has been demonstrated by several investigators. The potential for improvement using this technique is greatest when the nonorthogonality of the measured modes is largest. The amount by which the normal modes fail to be orthogonal for a variety of ocean bottoms, array lengths and discretizations, and array positions for the Pekeris model has been studied. Environments are selected to reflect sediment types characteristic of the continental shelf. It has been found that the nonorthogonality is greatest for water depths and frequencies at and just above modal onsets, for sound-speed ratios close to 1, and for arrays which span only a fraction of the water column. Judicious placement and length selection for short arrays, however, can give orthogonal measured modes for some combinations of frequencies and environments when a small number of modes are pres[illegible].

8:39

II2. Effects of measured mode nonorthogonality on conventional matched field processing. Juliette W. Ioup, George E. Ioup (Naval Ocean Research and Development Activity, NSTL, MS 39529-5004 and Department of Physics, University of New Orleans, New Orleans, LA 70148), Grayson H. Rayborn (NORDA, NSTL, MS 39529 and Department of Physics and Astronomy, University of Southern Mississippi, Hattiesburg, MS 39406), Donald R. Del Balzo (NORDA, NSTL, MS 39529), and Christopher Feuillade (ODSI Defense Systems, Inc., 6110 Executive Boulevard, Suite 320, Rockville, MD 20852)

As discussed by Rayborn *et al.* (preceding abstract), the potential improvement achievable from the use of modal filtering in matched field processing is greatest when the measured modes are least orthogonal. To assess the ability of matched field processing using a conventional cross-correlation estimator to realize this potential, ambiguity surfaces for a Pekeris waveguide have been constructed employing (a) the pressure fields at the hydrophones and (b) the amplitudes resulting from modal filtering. The quality of the surfaces is quantified utilizing measures that compare the height of the source peak above the mean and the height of the source peak above the standard deviation of the surface. The results indicate that modal filter processing, for a given array of hydrophones, offers the most improvement when bottom depth, bottom type, and frequency combine to produce measured modes that are the least orthogonal, and yields no improvement when the measured modes are orthogonal.

8:43

II3. Effects of correlated noise on the cross-spectral matrix in modal composition space. George B. Smith, Christopher Feuillade (ODSI Defense Systems, Inc., 6110 Executive Boulevard, Rockville, MD 20852), and Donald R. Del Balzo (Naval Ocean Research and Development Activity, Code 244, NSTL, MS 39529-5004)

Computer simulations of hydrophone cross-spectral matrices in a shallow-water waveguide were generated for signals with different mixtures of correlated and white noise. These matrices were then mapped to modal composition space, a space populated by vectors whose elements are the amplitudes for the trapped modes. It was found that, in modal composition space, the cross-spectral matrix is not sensitive to the difference between correlated and white noise, but is sensitive to the difference between noise and signal. While the distribution of signal and white noise among the elements of the cross-spectral matrix is similar before and after the mapping to modal composition space, the distribution of correlated and white noise is not. Temporally discrete noise sources, which are correlated at the hydrophones, but not from sample to sample, make little or no contribution to the off-diagonal elements of the cross-spectral matrix in modal composition space. This fact has significant implications for matched field processing in low signal-to-noise situations.

8:47

II4. Adaptive beamforming or matched field processing in media with uncertain propagation conditions. A. B. Baggeroer, H. Schmidt (Massachusetts Institute of Technology, Cambridge, MA 02139), W. A. Kuperman (Naval Research Laboratory, Washington, DC 20375), and E. K. Scheer (Woods Hole Oceanographic Institute, Woods Hole, MA 02543)

Adaptive beamforming or matched field processing provides high resolution with sidelobe control if accurate replica fields can be generated. The generation of these replica fields is a formidable problem requiring knowledge of the complex ocean propagation environment. On the other hand, the detection problem in the ocean may not require high resolution, whereas sidelobe control is still an important issue. Relaxing resolution requirements suggest that a certain tolerance incorporating uncertainty of the propagation conditions is permissible, or even desirable, because of the difficulties both in specifying the medium exactly and in identifying global peaks. This possibility of lowering the requirements on our knowledge of the environment is investigated with two methods: (1) by constructing multiple beam (constraint) algorithms and (2) by considering stochastic blurring by the medium. These two approaches are applied to plane-wave beamforming and matched field processing.

8:51

II5. Spatial matched processing for multipath propagation. Matthew Dzieciuch and T. G. Birdsall (Communication and Signal Processing Laboratory, 4242 EECS Building, Department of Electrical Engineering and Computer Science, The University of Michigan, Ann Arbor, MI 48104)

Underwater acoustic propagation is characterized by multipath or multimode propagation. Ray theory and mode theory are not fully adequate for modeling physical reality. Impulse responses can be more accurately calculated using Gaussian beam theory. Signal processors can be designed to take advantage of the channel complexity if the propagation is actually known so that detectability is increased. The proposed technique, channel matched filtering, synthetically backpropagates the wave front to a hypothesized source location. Accurate passive estimates of source location can be made without knowledge of the signal characteristics. GB theory can easily accommodate a range-dependent deep water environment. [This research supported by the Office of Naval Research.]

8:55

II6. A new technique of acoustic mode filtering in shallow sea. Harish M. Chouhan and G. V. Anand (Department of Electrical Communication Engineering, Indian Institute of Science, Bangalore 560 012, India)

A new technique of filtering acoustic normal modes, which overcomes many of the drawbacks of the earlier techniques, is presented in this paper. It is based on the fact that each normal mode in an isovelocity channel comprises a pair of plane waves with characteristic directions of propagation symmetrically disposed with respect to the channel axis. A vertical array of equispaced hydrophones is shaded so as to steer nulls in the directional response of the array along the directions of arrival of plane waves corresponding to the unwanted modes. All the shading coefficients are real, leading to simplicity in the hardware realization of the processor. The shading coefficients are invariant to a shift in the position of the array. The array need not span the entire depth of the ocean. Efficient filtering is possible even when the eigenfunctions of the modes have a significant penetration into the bottom. [Work supported by DOE, Government of India.]

8:59

II7. Matched catastrophe deconvolution with application to the inversion of marine seismic refraction data. Michael G. Brown (Rosenstiel School of Marine and Atmospheric Science, University of Miami, 4600 Rickenbacker Causeway, Miami, FL 33149) and Paul E. Bullwinkel (Applied Measurement Systems, Inc., 1415 S.W. 21st Avenue, Fort Lauderdale, FL 33312)

The problem of extracting accurate estimates of the travel times of unresolved arrivals (e.g., the second and third arrivals within a triplication) from a set of noisy bandlimited measurements of a time-dependent acoustic wavefield is addressed. The method of solution presented is based on the assumption that the underlying caustic structure (or, equivalently, the travel time curve structure) of the wavefield is known. Because generic caustics associated with causal wavefields take on only certain forms, this is a weak assumption. Additionally, it is assumed that the medium

source localization techniques based on mode filtering have been developed for stratified waveguides. In this paper, some problems of source localization in almost-stratified waveguides are discussed. Specifically, the Prony method is proposed for source bearing in range-dependent waveguides. It is found that the Prony method only requires a "local almost-stratified" condition, which means that within the data sampling aperture length the field can be treated as adiabatic modes. For most of the practical interesting cases, this condition can be satisfied quite easy.

2:20

LL4. Extraction of average under-ice reflection amplitudes and phases with matched field processing. E. Livingston and O. Diachok (Naval Research Laboratory, Code 5120, Washington, DC 20375-5000)

Average low-frequency under-ice reflection amplitudes and phases in the central Arctic were extracted from long-range (259 km) signals from fixed cw sources detected on a long (1 km) vertical array (the FRAM IV experiment) using conventional [H. Bucker, J. Acoust. Soc. Am. 59, 368 (1976)] and maximum likelihood [R. Fizell, J. Acoust. Soc. Am. (to be published)] matched field processing methods. Theoretical computation of amplitudes and phases for all assumed ranges and depths were based on the Porter–Reiss [J. Acoust. Soc. Am. 77, 1760–1767 (1985)] normal mode code. Under-ice reflection amplitudes and phases were incorporated into the propagation code and varied iteratively to achieve maximum signal gain and minimum range and depth errors. The resultant best data-fitting amplitudes and phases will be compared with expectations based on under-ice scattering theories and laboratory-scale model experiments.

2:35

LL5. Ventriloquism and spurious sound sources in underwater acoustics. Ian Roebuck (Admiralty Research Establishment, Portland, Dorset DT5 2JS, England)

With the increased use of active noise control has come wider awareness that the source distributions generating prescribed sound fields are not unique. In particular, the possibility of precisely reproducing the field due to a time-varying monopole by a multipole source (of infinite order) located elsewhere, has been established. In this paper, the fundamental physical limitations of carrying out such an "underwater ventriloquism act" in practice—developing a "constructive" algorithm for the various multipole coefficients and criteria for truncating the process are examined. It is shown that this is closely related to earlier ideas on the effective size of "point" sources [I. Roebuck, J. Acoust. Soc. Am. Suppl. 1 69, S87 (1981)] and further that acoustic efficiency limits the extent to which the transmitting multipole elements can be compacted without destructive mutual interaction. The manner in which the greater effective size of the "spurious" multipole source limits the potential for deception in the presence of varying boundaries is also analyzed.

2:50

LL6. Space-time processing, environmental–acoustic effects. W. M. Carey (Naval Underwater Systems Center, New London, CT 06320) and W. B. Moseley (Naval Ocean Research and Development Activity, NSTL, MS 39529)

The processing of acoustic waveforms by arrays requires an understanding of the temporal and spatial characteristics of signal and noise fields. Temporal and spatial processing schemes are analogous transforms that can employ a variety of windows (such as Hann, Hamming, etc.). However, the ocean environment is a filter that introduces variability to a signal in both spatial and temporal domains. This randomness is superimposed on an ambient sound channel characteristic. In the case of static source and receiver combinations, the limits on horizontal broadside array resolution are due to volume scattering and surface scattering as long as the time scale is less than the signal correlation time. However, in the case of a moving source–receiver, the temporal and spatial scales are coupled through the sound channel characteristic and the fluctuation effects due to multipath or modal variations must also be considered. This paper reviews fundamental environmental effects and their influence on arrays in the deep ocean sound channel. [Work performed while at NORDA.]

3:05

LL7. Passive synthetic arrays. W. M. Carey (Naval Underwater Systems Center, New London, CT 06320)

Passive-synthetic apertures [W. Carey and N. Yen, J. Acoust. Soc. Am. Suppl. 1 75, S62 (1984)] were formed with experimental towed hydrophone data in a sound channel that supported RR and RSR transmission. These apertures were formed with lengths up to 95λ with coherent temporal processing gains approaching 0.75 of theoretical. These results and those of previous investigators [R. Fitzgerald, J. Acoust. Soc. Am. 60, 752–753 (1976); R. Williams, J. Acoust. Soc. Am. 60, 60–73 (1976)] indicate that synthetic apertures can be formed by the coherent summation of the phase-corrected summation of either hydrophone or subaperture beams over successive time samples when the synthetic aperture length is less than the spatial coherence length and the processing time is less than the temporal coherence length. The evaluation of synthetic apertures requires comparisons with conventional and other high-resolution techniques. Comparisons between conventional array processing and high-resolution techniques [maximum entropy (ME) and maximum likelihood (ML) methods] are performed by use of the analytical expressions developed by A. T. Parsons (AUWE, TN 700/83) for the determination of the array, integration, and the net processing gains. Analytical comparisons between conventional and synthetic aperture arrays formed with either the same number of hydrophones or with the same effective length but a different number of hydrophones, show that, when the spatial processing gain exceeds the loss in integration gain, then the use of synthetic apertures is advantageous. [Work performed while at NORDA.]

3:20

LL8. Performance of sinusoidally deformed planar arrays. James H. Leclere, Donald R. Del Balzo, Deanna M. Caveny (NORDA, Code 244, NSTL, MS 39529), George E. Ioup (University of New Orleans, New Orleans, LA 70148 and NORDA, NSTL, MS 39529), Jeffrey L. Becklehimer, and Donald A. Murphy (NORDA, NSTL, MS 39529)

The investigations of Caveny *et al.* [J. Acoust. Soc. Am. Suppl. 1 80, S26 (1986)] are extended for the cases of horizontally and vertically towed planar arrays. Horizontal and vertical arrays of three lines (64 hydrophones each) and nine lines (28 phones each) are included. In addition, a nine-line array with five horizontal and five vertical lines (with the middle line of each in common) is also examined. Horizontal sinusoidal deformations of one-half cycle (and in some cases two and three half-cycles) are applied to each line. Complex pressure fields are modeled for various source directions for each array using the code BEAMSTATPAK of Collier (private communication). Beamforming is then done with the known array configuration and with the assumption that the array is planar (for selected cases). Degradations resulting from assuming planarity and the ability to remove left/right ambiguity are summarized as a function of the source location and the amount of array deformation in terms of reduced gain and angular resolution. Array performance is also examined in the presence of a realistic vertical noise distribution. [Research sponsored by NUSC.]

3:35

LL9. Sidelobe suppression in correlated multipath estimates. Peter C. Mignerey (U.S. Naval Research Laboratory, Code 5122, Washington, DC 20375-5000)

Some environments cause a propagating signal to split along several different paths. When such multipath propagation occurs, the covariance among signals traveling along rays emanating from a common source is expected to be larger than the covariance between signals generated by independent sources. An estimate of the covariance between signals arriving from two different directions is shown to be a bilinear form. The ability of the bilinear form to distinguish a correlated arrival from an indepen-

Anderson and Munson [J. Acoust. Soc. Am. 35, 1162–1168 (1963)] showed that the directivity index (DI) of an infinitely densely populated spherical shell array was about equal to that of a sphere. Extrapolating to discrete elements, this means the shell requires far fewer elements. They did not compute DI using amplitude shading, due to the impractical cost of such systems at that time. Today's technology removes that constraint. This work revisits the problem with shading, using an approach for choosing the amplitude shading coefficents that maximizes DI [H.S.C. Wang, J. Acoust. Soc. Am. 57, 1076–1084 (1975)]. Calculations have been made for the DI of shaded cubic volumetric arrays, forming beams perpendicular to one of its faces, in the presence of isotropic noise. Results show that for 27 and 125 element arrays with element matrix spacings of 1/2 wavelength, a full 10 log (number of elements) can be obtained for DI. Work is underway to investigate larger arrays and smaller spacings. The approach will also be extended to nonisotropic noise fields. [Work supported by NORDA and NOSC exploratory development programs.]

9:00

117. Least-squares and single-filter always-convergent iterative deconvolution of transient signals for correlation processing. James H. Leclere, George E. Ioup,[a] Juliette W. Ioup,[a] and Robert L. Field (Code 244, NORDA, Stennis Space Center, MS 39529)

Correlation processing for distributed sensors is most accurate for short pulses and those whose autocorrelation is sharply spiked. For longer transient signals, multipath arrivals at each sensor have significant interference with each other, and it is difficult to identify individual arrival times. Deconvolution of the received signal to sharpen the transients is one method to decrease the overlap and increase the accuracy with which travel times can be identified. Deconvolution can also be applied after cross correlation to sharpen the autocorrelation of the transients. Least-squares deconvolution is the most commonly used approach for acoustic signals. It has the disadvantage of being computer intensive when filters for long transients are needed. An alternative approach, the single-filter application of the always-convergent iterative technique, is faster and provides variable control for noise. The two techniques are compared for actual underwater acoustic multipath transient signals. Single filter application of always-convergent iterative noise removal is compared to the use of a modified Blackman–Harris window for noise control. [a] Also at the Department of Physics, University of New Orleans.

9:05

118. Comparison of double and triple cross correlation for arrival time identification of amplitude- and frequency-modulated acoustic transient signals. Juliette W. Ioup,[a] George E. Ioup,[a] Robert L. Field, and James H. Leclere (Code 244, NORDA, Stennis Space Center, MS 39529)

The triple cross correlation of three signals is a simultaneous function of two lags. It is an alternative to cross correlations taken two at a time for determining the lags for a given source at three distributed sensors. It should offer improvement in arrival time identification only when the statistics of the signal have significant third moment components. In this study, amplitude- and frequency-modulated snythetic transient signals are propagated over several possible paths to three sensors, and the triple correlation of the received pulses computed, as well as the cross correlations of the same three signals two at a time. The efficacy of these two approaches is compared for a variety of amplitude- and frequency-modulated transient signals and multipath interference conditions. [a] Also at the Department of Physics, University of New Orleans.

9:10

119. *In situ* acoustic calibration for a large aperture array. Barbara J. Sotirin (Marine Physical Laboratory A-005, Scripps Institution of Oceanography, La Jolla, CA 92093)

During September 1987, a large aperture acoustic array was deployed vertically in the Northeast Pacific to study low-frequency noise in the ocean. Coherent combination of the 120-channel outputs requires knowledge of individual element amplitude and phase response for accurate results. Two *in situ* methods of array calibration are described and results from the September experiment are presented. The first method used transmissions from a low-frequency source of known location and power level. Simulating the conditions encountered during the transmission, the power arriving at the array was predicted by several acoustic propagation models. By comparing the array response at specific frequencies to the response predicted by the models, an absolute calibration was obtained. An error curve for the phase data was generated by unwrapping the phase, accounting for a sampling offset in the array, and subtracting a multiple linear regression curve. The second method determines relative amplitude levels by examining the average ambient noise power output of a specified frequency band across the array. Using spectral, coherence, and directionality plots, the level of self-noise in the array was shown to be below that of the ambient noise being measured. These two independent methods provide a consistent set of element calibration values used for array beamforming. [Work supported by ONT.]

9:15

1110. Abstract withdrawn.

9:20

1111. Matched-mode processing corrections for array tilt and bottom type. James A. Mercer (Applied Physics Laboratory, University of Washington, Seattle, WA 98105)

In a related effort, Homer Bucker has shown that matched-mode processing for an unknown sound-speed environment can be significantly improved if correction factors for the mode-line amplitude functions can be determined. The correction factors are obtained when a source with known location is available to calibrate the system. This paper describes the results of applying the same techniques for simulated cases of unknown array tilt and bottom characteristics.

9:25

1112. Self-consistent modeling of signal and noise in a three-dimensional environment. John S. Perkins, W. A. Kuperman, and F. Ingenito (U.S. Naval Research Laboratory, Code 5160, Washington, DC 20375-5000)

Previous propagation work is extended to model surface noise, shipping, and signal sources in a fully three-dimensional environment. The noise cross-spectral density matrix for a vertical array is computed as the sum of a local contribution and propagation from distant small patches of ocean surface. Propagation from any point to the array is made efficient

(2) how much analog precision is needed in the connections in the network, (3) the number of training examples the network must see before it can be expected to form reliable generalizations, and (4) the efficiency with which a network extracts information from the training data.

John Denker, Daniel Schwartz, Ben Wittner, Sara Solla, John Hopfield, Richard Howard, and Lawrence Jackel, Complex Systems, in press (1987).

14:42

An Analog VLSI System for Neural Network Learning Experiments DANIEL B. SCHWARTZ and RICHARD E. HOWARD AT&T Bell Laboratories.

Because the complexity available from standard VLSI has grown far beyond our ability to simulate it, it has become interesting in its own right. Adaptive neural network models are an example of a class of complex systems where a mapping directly onto VLSI is of great practical and fundamental interest. However, the continuously variable connections required for adaption are not easily represented in a digital world. We are building a collection of analog circuits from standard digital CMOS with variable strength analog connections based upon charge storage by a pair of MOS capacitors. The capacitors are tied together by a string of FETs, allowing the connection strength to be monotonically varied by moving charge between them. Our current designs have 7 bits of analog depth of both polarities. The chips have about 10^3 connections and can easily be cascaded to make larger networks. The available computational speed is dominated by i/o bandwidth of the host controller. We will discuss use of such chips and their limitations.

14:54

O18 3 Specific Heat for a Boson System with Anharmonicity. M.S. Wartak, C.Y. Fong, Department of Physics, University of California, Davis.--We used the model Hamiltonian

$$H = \sum_{i=1}^{N} \left[\epsilon b_i^+ b_i - \Gamma_i b_i^+ b_i^+ b_i b_i + \Delta \left(b_{i+1}^+ b_j + b_{i+1} b_i^+ \right) \right]$$

to study the thermodynamic properties of the one-dimensional boson system with on-site anharmonicity, and with Δ much smaller than ϵ. For the calculation of partition function we have used the path-integral method. The Dyson equation is solved in the nearest-neighbor approximation. The resulting expression for the free energy is evaluated in the static approximation using the steepest descent method. The behavior of specific heat for different values of Γ and Δ is examined.

15:06

O18 4

Color Induced Transitions in the Presence of a Nonlinear Potential, G. P. TSIRONIS, P. GRIGOLINI, University of California, San Diego.-- We show that the negative diffusion coefficients exhibited by current approaches to the Fokker-Planck equation for non-Markovian and bistable processes result from assuming that the system reaches a conventional steady state[1]. By lifting this assumption[2] we show that when a critical value of the noise correlation time τ is exceeded, the process of escape over a barrier agrees with an exact prediction for the large-τ regime and thus that the linear response approximation behind our theory produces exact results for arbitrary correlation times.

1. G. P. Tsironis, P. Grigolini, "Rate processes activated by color noise: Bridging two exact limits', UCSD preprint

2. J. Masoliver, B. J. West, K. Lindenberg, Phys. Rev. A 35, 3086 (1987)

15:18

O18 5 Surface Loss in a Parabolic-Equation Model. MARTHA P.M. HEAD and W. JOBST, Naval Oceanographic Office and ELEANOR S. HOLMES, Science Applications International Corporation. — Ocean-surface loss of acoustic energy is often given as a function SL(θ) of the grazing angle θ. If p(z) is the complex acoustic-pressure field (from a parabolic-equation model) as a function of depth z near the surface, a Fourier transform F(K) of p(z) yields pressure as a function of the vertical wave number K. K is proportional to sin θ, thus F(K) is a function G(θ) of θ. We account for the surface loss by multiplying G(θ) by a loss function L(θ) — related to SL(θ) — before transforming back to physical space. The method also is applicable to bottom loss. Numerical implementation, angular resolution, and limitations of the method are discussed. Numerical examples are presented.

15:30

O18.6 Effects of Noise on Pressure and Modal Amplitude Matched Field Processors.* GEORGE M. FRICHTER, IV, JULIETTE W. IOUP, Univ. of New Orleans,** GEORGE B. SMITH, Xavier Univ., GEORGE E. IOUP,** Univ. of New Orleans, CHRISTOPHER FEUILLADE, Syntek, GRAYSON H. RAYBORN, Univ. of Southern Miss.,** and DONALD DEL BALZO, NORDA--Modal amplitude matched field processing for acoustic signals received by a vertical array of hydrophones is used to determine the effects of spatially correlated and uncorrelated noise fields on pressure and modal amplitude matched field processors. Various amounts of white isotropic noise and spatially correlated noise as calculated by a normal mode noise model are combined with the field due to a submerged acoustic source to produce simulated cross spectral matrices. A phone-to-mode space mapping is then used to obtain the corresponding cross amplitude correlation matrices. Both conventional and maximum likelihood processing are used. Results show that spatially uncorrelated noise degrades modal amplitude processors more than spatially correlated noise.

**Supported in part by ONR/NORDA Contract N00014-87-K-600

15:47

O18.7 A Review of Underwater Acoustic Propagation Models Emphasizing Coupled Full-Wave Range-Dependent Propagation. JOSEPH E. MURPHY, University of New Orleans, New Orleans, LA 70148; STANLEY A. CHIN-BING, Naval Ocean Research and Development Activity, NSTL, MS 39529-5004. -- Underwater acoustics is usually not discussed at APS meetings, but rather is confined to peer review meetings. However, given the close proximity of the Navy's lead ocean environmental RDT&E laboratory, the Naval Ocean Research and Development Activity (NORDA) located 45 miles from New Orleans, we take this opportunity to present a review of ocean acoustic propagation modeling. In the ocean, the index of refraction is variable; acoustic transmission paths are curved and the coupling of the refracted, reflected, and diffracted acoustic fields from boundaries give rise to complicated classical physics problems. The prominent acoustic models are based on normal mode, parabolic approximation, FFT, and modified ray methods. Each of these include a limited number of physical mechanisms. We have therefore developed a coupled full-wave range-dependent ocean acoustic propagation and scattering model based on the finite element method. This model is superior especially at low frequencies. Numerical simulations will be presented showing the effect of a fractal under-ice interface with ice keel on the fully coupled range-dependent underwater acoustic field.

15:54

O18 8 Determination of Instrumentation Parameters for Optimum Resolution with Deconvolution. GEORGE E. IOUP, ABOLFAZL M. AMINI, and JULIETTE W. IOUP, Univ. of New Orleans**--An important design and parameter selection

PERFORMANCE OF SINUSOIDALLY DEFORMED LINE ARRAYS

Deanna M. Caveny,* George E. Ioup,† Donald R. Del Balzo, and James H. Leclere
Naval Ocean Research and Development Activity
NSTL, MS 39529

ABSTRACT

Previously it has been shown that deformations of towed arrays from a straight line shape can produce significant distortions in beam patterns and errors in bearing estimation if the beamforming assumes linearity, and that a deformed array helps to remove left-right ambiguities in the beam patterns, provided the shape is known. In this work these two effects are studied for undamped and damped sinusoidally deformed arrays with small deformation amplitudes. By use of fixed arc length separations along the array, the phone (x,y) coordinates are determined numerically. The error in assuming equal x spacing is shown. The complex pressure fields are modeled using BEAMSTATPAK of Collier. Then beamforming is carried out (1) with the known array configuration, and (2) assuming that the array is linear, and array responses are shown for each. Degradations resulting from assuming linearity and the ability to remove left-right ambiguities are discussed in terms of reduced gain, angular resolution, and bearing errors. Performance is reported as a function of deformation, s/l, from 0.0 to 0.3. True peak-ambiguous peak signal gain differences range to 9 dB for sources at broadside and to just over 2.5 dB for arrivals near endfire. Shape-unknown degradation ranges to 7 dB at broadside but is less than 1 dB near endfire.

---

* Present address: Department of Mathematics, University of Colorado, Boulder, CO 80309.
† Also at Department of Physics and Geophysical Research Laboratory, University of New Orleans, New Orleans, LA 70148.

INTRODUCTION

Hinich and Rule,[1] Hodgkiss,[2] Bouvet,[3] Ginzkey,[4] and Butler[5] have shown that deformations from a straight line shape in the horizontal plane of towed arrays can produce significant distortions in array response patterns and errors in bearing estimation if the beamformer assumes linearity. Hinich and Rule[1] use approximate undamped and damped sinusoidal shapes and report the case of three and one half cycles of the sinusoid. For the damped case, the damping is such that the deformation increases as one moves away from the towing platform. Hodgkiss[2] employs a single circular arc beginning and ending at a node on the nominal array axis. He discusses errors in passive ranging as well as those of bearing estimation. Bouvet[3] develops a model for large random array variations with fixed intersensor separations (non- elastic array). He applies the model to an array in the shape of a circular arc. Bouvet also gives a helpful brief review of related literature. Ginzkey[4] studies the effects of small two-dimensional random position errors. Butler[5] uses a sinusoidal deformation model which assumes equal x spacing of the phones.

In this work the performance of arrays with mainly small deformations in the horizontal plane into shapes which are commonly observed to occur in practice is examined. The model developed is capable of treating large deformations as well. The physical basis for the undamped or damped sinusoidal shape model derives from a harmonically driven damped oscillator. The small steering corrections of the towing platform provide the driving force. The attachment point of the neutrally buoyant horizontal array is the origin for this model and it is approximated to be a fixed node. Because it serves as a useful point of reference, the name tow point will be used for this node. Since the acoustically active part of the towed array is generally attached to the towing cable by a vibration isolation module (VIM), the model does not place the first hydrophone at the tow point but locates it such as to allow for the VIM. The model permits any realistic whole or fractional number of cycles, amplitude, and damping factor for the array. A drogue is assumed to be attached to the aft end of the array and thus the damping in this model decreases the deformation as one moves away from the tow point, in contrast to the model of Hinich and Rule.[1] The reader is referred to the works of Lee,[6] Ketchman,[7] and Brandenburg[8] for a more detailed discussion of array deformation models.

To approximate a sinusoidal shape, Hinich and Rule[1] use straight line segments between hydrophones. To calculate the locations of hydrophones for the sinusoidal models without approximation, however, it is necessary to fix the hydrophone spacing along the array curve for the determination of the x and y (horizontal plane) coordinates. This model[5] an elastic array with varying intersensor separations, overcoming the limitation discussed by Bouvet.[3] Figure 1 shows a sample half cycle sine deformation and the x and y coordinates for the 75th of 128 phones. The vertical variable z is assumed zero for this study. The method for determining the coordinates

involves the numerical evaluation of the arclength integral. In the limit of small sinusoid amplitudes, the hydrophones may be assumed to have equally spaced x locations, greatly simplifying the calculation. A summary of the error in this approximation versus amplitude is given. For the present work, only the arclength integral method is used, and neither the Butler assumption of equally spaced x locations nor the Hinich and Rule assumption of straight line segments between phones is employed.

All acoustic field modeling and beamforming for this study are performed using BEAMSTATPAK, a package constructed by Collier.[9] The package generates model cross spectral matrices for arbitrary hydrophone locations in three dimensions. Although several beamforming options are available in BEAMSTAPAK, only conventional beamforming is chosen for all comparisons discussed below.

DETERMINATION OF HYDROPHONE X-Y LOCATION

The natural dimensions for scaling position variables and other length measures in the study of the deformation of equally spaced hydrophone arrays are the array element spacing, d, and the design wavelength, $\lambda = 2d$. Length variables can easily be converted to meters once the wavelength is specified, e.g., for a design frequency of 1000Hz and a sound speed of 1500m/s, $\lambda = 1.5$m and $d = 0.75$m. We assume that the forward VIM has an arclength of 6d, that the VIM is followed by 128 hydrophones, and that the active array is followed by a drogue for stability. The first hydrophone is at an arclength d/2 from the point where the VIM connects to the active array. Therefore the first sensor lies at an arclength of 6.5d along the array from the tow point origin. Each succeeding sensor is separated by an arclength d along the curve from the previous one. In Fig. 1 the coordinates are in units of the phone spacing for a half cycle deformed array. A deformation amplitude of 10d is chosen for the figure to render more apparent the details of the shape, although this deformation is much larger than those tested in this work.

We then state the problem as follows. Assume that the towed array takes the shape of an undamped or damped sinusoid. Given a specific number of cycles, the undamped amplitude, and the amount of damping, determine the (x,y) coordinate location of each phone. An equation for the array shape can be written as:

$$y(x) = A\ e^{-ax} \sin\left(\frac{\pi}{w} x\right) , \qquad (1)$$

where the undamped amplitude, A, and the amount of damping, a, are specified. The third parameter, w, although fixed by the number of cycles, is not known initially. It is to be determined before the coordinates are calculated.

Consider an undamped sine curve of p cycles. Let L denote the total array length, which is (N + 5.5) d if there are N phones and the VIM is 6d. Then the arclength between two adjacent nodes for an undamped array is L/2p. The arclength integral is given by

$$\int_0^u [1 + A^2q^2\cos^2qx]^{1/2}\, dx\,, \qquad (2)$$

where $q = \pi/w$ and u and w are to be determined. As an initial guess, we choose $u = L/2p$ and $w = u$ in expression (2). Using a numerical integration routine, we evaluate the arclength integral. The calculated arclength is then compared to the known (desired) arclength to the first node, and u is adjusted successively, with $w = u$, until the difference between the calculated and the known arclength, L/2p, is less than a specified tolerance.

In the damped case, the equal spacing of the zero-crossings (or nodes) is preserved, but the array length between any two adjacent nodes is no longer a constant. The arclength integral is given by

$$\int_0^u [1 + A^2e^{-2ax}(a^2\sin^2qx - 2aq \sin qx \cos qx + q^2 \cos^2 qx)]^{1/2}\, dx\,. \qquad (3)$$

In this case, the upper limit of the arclength integral (i.e., the unknown value u) is chosen to be the x-coordinate of the last phone. Then the known arclength is the total array length. Initially u is taken to be L and $w = u/2p$. The arclength expression (3) is evaluated and u is adjusted, with $w = u/2p$, until the integral is close enough to L.

The x-coordinate of each phone is found in a similar fashion except that w is now determined and u gives the phone x coordinate. The integration is initially from the tow point to the first

phone, or generally from the last known phone location to the adjacent unknown location. The corresponding y-coordinates are easily calculated from Eq. (1).

If instead one assumes that the x-coordinates are equally spaced with spacing d, the numerical integration could be avoided. For sine curves with small amplitudes, this assumption may introduce only small errors. But the magnitude of the error grows with increasing phone number and increasing array deformation amplitudes. The assumption of this equal spacing always shifts the x-coordinates in a positive direction, making the array appear longer than it actually is, and the accumulated error increases more rapidly when the tangent line to the sine curve is steeper. Figure 2 illustrates the absolute value of the error in the x coordinate of each phone as a function of phone number for arrays with one half cycle distortion of various deformation amplitudes. The cumulative effect of the equal spacing assumption is evident, especially for the larger array amplitudes. The deviations of the true x positions from equal x spacing do not become larger than 0.1d (0.05λ), however, until the deformation of the array is greater than 2.0d for a half cycle sine array of 128 phones. Differentiation of Eq. (1) shows that the error in y is less in magnitude than the x error.

EXAMPLES OF BEAMFORMING IN PLACE AND AS IF LINEAR

Hodgkiss[2] investigates plane wave beamforming for various source locations and increasing circular arc array bows. His results are given as array response plots for a beamformer containing the actual phone locations and corresponding plots for a beamformer which assumes that the element locations are linear. He does not consider left-right ambiguity removal and his array response patterns go over only 180°. Similar studies are conducted here for arrays having undamped and damped sinusoidal geometries, with the addition of an examination of left-right ambiguity removal and the calculation of performance curves. Figure 3 illustrates the various array geometries considered in this study: a) a linear array for reference; b) an undamped half-cycle deformation with amplitude of 2.13 phone spacings; c) an undamped full cycle deformation with amplitude of 1.47 phone spacings; d) an undamped cycle and a half deformation with amplitude of 0.87 phone spacings; e) a damped half cycle deformation with maximum amplitude of 1.55 phone spacings (A = 2.13d and a = 0.0069); and f) a more highly damped half cycle deformation with maximum amplitude of 0.95 phone spacings (A = 2.13 $\propto$ and a = 0.020). These amplitude and damping factor values were chosen to produce a value for the undamped cases of 0.3 in the array shape statistic, σ/λ, with σ the rms shape distortion as measured from a best fitting straight line, and values of 0.2 and 0.1, respectively, for the damped cases. The figure shows the first and last phones and every eighth phone. The first phone is not at zero because of the VIM.

The source azimuths considered in this study are 90°, 45°, and 10° from endfire (broadside = 90°), all at the design frequency and all initially in the horizontal plane. The issue of out-of-plane arrivals is briefly discussed later, and these arrivals are shown to produce essentially the same results as the in-plane arrivals. Figure 4 illustrates the array response patterns of these sources for a linear array over the full 360° azimuthal sector. Note the standard results of beam broadening away from broadside and the occurance of grating lobes as the signal approaches endfire. Figures 5-7 contain array response patterns for sinusoidally deformed arrays. In each of the latter cases, beamforming is done with (1) the actual phone locations known and (2) with the incorrect assumption that the array geometry is linear. The responses shown in Fig. 4 are included so that the deformed array responses may be compared. Beam powers for all figures are referenced to zero dB for the linear array response maximum at a given source direction. None of the responses is given below -30 dB.

In Fig.5, the response for the array shown in Fig. 3b, a half cycle sine curve with A = 2.13d, $\sigma/\lambda = 0.3$, is given for sources at (a) and (b) 90°, (c) and (d) 45°, and (e) and (f) 10°. In Figs. 5(a), (c), and (e) the array shape is assumed known and the actual element locations are used in the beamforming. Because the array has almost the same total aperture as the linear array, the forward (true) peak is almost identical to the linear response. The ambiguous (false) peak, however, does not have the same phase delays for the deformed array as the forward peak does, so it is significantly changed. It has less signal gain, is broader, and is broken up to several local maxima for the sources at 90° and 45°. While the false peak at -10° (corresponding to a source at 10°) is somewhat reduced and broadened, it is not broken up in the same way as the others. This is due to two factors: a) the array has less resolution (wider beams) near endfire than at broadside and b) a plane wave arriving in a direction close to endfire sees a smaller array deformation than one arriving at broadside. If, as is generally the case, the array shape is unknown and beamforming is done assuming the shape to be linear, the responses of Figs. 5(b), (d), and (f) result. The signal gain is reduced, especially at 90° and 45°, where the response peaks are also split. At 10°, the reduction in gain is small and the main peak shape is close to that of the linear response, again because the deformation looks smaller and the beams are wider near endfire.

For the remaining array shapes only the array response to a broadside arrival is shown. The second and third undamped examples are in Fig.6, while the damped cases are illustrated in Fig.7. For the undamped arrays, $\sigma/\lambda = 0.3$, the same value as the half cycle undamped array of Fig. 5. For the one cycle array, a distortion amplitude, A, of 1.47d gives this σ/λ value, while for the cycle and a half array, A = 0.87d. The general behavior of the responses of the single cycle array, Figs. 6(a) and (b), and the one and one half cycle array, Figs. 6(c) and (d), is similar to that of the broadside responses of the half cycle array. For both the Fig.6 cases, however, the false peak in the shape-known responses and the true and false peaks in the shape-unknown responses are

considerably more broken with local maxima and minima than the half cycle case. This is because the deformed array shapes themselves have more structure. In effect, the deformed array is composed of several nearly-straight subsections, each of which has its own natural direction. Thus the incident plane wave is resolved into multiple directions.

Since the damped arrays of Fig.7 have smaller values of σ/λ than the undamped cases, the responses are closer to the linear array response at broadside than the undamped responses of Figs. 5 and 6. The responses in Figs. 7 (a) and (b) correspond to an array with $\sigma/\lambda = 0.2$ (A = 2.13d, a = 0.0069) and in Figs. 7 (c) and (d) to an array with $\sigma/\lambda = 0.1$ (A=2.13d, a = 0.020).

The irregular nature of the broken peaks in Figs. 5 through 7 leads to instabilities in such performance measures as peak height, bearing, and beamwidth because of the difficulty in defining these quantities. The splitting of the true peak when the beamforming is done assuming a linear array leads to bearing errors resulting from choosing the largest sub-peak. This suggests that for arrays which have a large enough aperture to resolve this splitting, it is probably better to find the centroid of the overall peak, or to fit a smooth analytic shape to it, or to use some other alternative to choosing the value of highest signal gain for the determination of source direction. Fitting a smooth analytic shape to the peaks also suggests itself as an approach to dealing with the instabilities in the peak height and beamwidth measures. Nevertheless, in order to have a straightforward measure of performance, none of these procedures are adopted for this study. They may prove crucial, however, for obtaining the best bearing estimate when doing shape-unknown beamforming.

We note that the shape-unknown responses are all symmetric about 0° in Figs. 5 - 7. To understand this result, consider the phases at the hydrophones for arrival directions of plus and minus θ. For the deformed arrays, arrivals from $+\theta$ will have, at each phone, a shifted phase Δ_+ from the phase value at a straight line array and arrivals from $-\theta$ will have a different shifted phase Δ_-. These phases will be correctly incorporated into the cross - spectral matrix. The steering vectors for shape - known beamforming correspond to the actual element locations. For shape - unknown beamforming, the same cross - spectral matrix is used, since the acoustic fields are taken to be unchanged. The steering vectors, however, are those corresponding to a linear array. The phase changes in going to these steering vectors from the correct ones are opposite to those in the cross spectral matrix mentioned above, and thus the plus and minus arrival directions have the same (incorrect) array response.

Hodgkiss[2] shows that the degradations in the beamforming process, with the incorrect assumption of linearity, increase as the array bow increases for circular arc shapes. The following sections contain a systematic study of this degradation in terms of loss in signal gain and an examination of bearing shifts and beamwidth broadening for sinusoidally deformed arrays. The power losses are graphed versus σ/λ, where σ is the rms deviation of the sinusoidal array

elements from the best fitting straight line. The left-right ambiguity removal is also investigated in terms of the power difference between the true and false peaks and the beamwidth broadening of the false peak, both of which are shown as functions of σ/λ.

LEFT-RIGHT AMBIGUITY RESOLUTION AND LINEAR DEGRADATION

Probably the most obvious change in the array response patterns as they describe a deformed array is the possible power loss in both the real and ambiguous signal peaks. This loss can be studied from two different perspectives.

The first considers the "ability" of a given array shape to resolve left-right ambiguities. Both Hinich and Rule[1] and Hodgkiss[2] discuss this advantage of a deformed array over a linear array. Figure 8 illustrates the power loss in the "secondary," or ambiguous, peak. This loss is plotted vs σ/λ for various array damped and undamped shapes (half cycles, full cycles, one and a half cycles) and for various source azimuths. The azimuths selected are 10°, 30°, 45°, 60°, and 90° for the half cycle cases and 10° and 90° for the others. Figure 8 summarizes the results for all shapes and all azimath angles considered. In Fig. 8 (a) the half cycle damped array performance is given for left-right ambiguity removal in terms of false peak-true peak power difference in dB versus σ/λ. For the damped array σ/λ may be varied by changing the amplitude or the damping factor. We have chosen to vary the damping for this performance evaluation. In general, for this and all cases in Fig. 8, the ability to discriminate an ambiguous peak from a true peak by power difference is greatest for sources at broadside and decreases to be least for sources close to endfire. This trend is expected because the left-right phase difference is smaller at endfire. Deviations from this observation are slight in Fig. 8, and occur because of the instabilities in the broken false peak maxima discussed earlier. In Figs. 8 (b), (c), and (d) the left-right ambiguity removal performance for the undamped half cycle, cycle, and cycle and a half are summarized. At broadside, for a given σ/λ, the undamped half and full cycles are better (i.e., have greater power difference) at resolving left-right ambiguity than a one and a half cycle array. An examination of Figs. 5(a) and 6(a) and (c), however, shows that for $\sigma/\lambda = 0.3$, this advantage in resolution is due mainly to two thin spikes in a highly broken one and a half cycle ambiguous peak. If an average or curve fit peak is used instead of the tallest subpeak to measure ambiguity removal this distinction in the difference performance measure is not expected to be as large.

The second perspective considers the loss in array signal gain which results from assuming that the array shape is linear. Figure 9 shows the power loss in the source peaks, relative to the linear peak power, plotted versus σ/λ, for the same array shapes and azimuthal source directions considered in Fig. 8. For all cases the degradation is greatest for broadside arrivals, decreasing, in general, as the angle decreases to become least at 10°. The exceptions, as before, are due to the

irregular qualities of the degraded peaks. As expected, the degradation becomes worse with increasing array deformations for all shapes. For a given source direction the degradations are similar for almost all combinations considered, except for differences in the 90° and 60° results. Only the half cycle undamped and the full cycle performance for sources at broadside track fairly closely for these arrival angles among the cases examined. The performance at $\sigma/\lambda = 0.3$, however, is identical for all arrival angles for the damped and undamped half cycles because the two arrays are the same. (We note that this is true in Fig. 8 as well.) The damped array has $\sigma/\lambda = 0.3$ when the damping is zero. To study larger values of σ/λ for the damped array we would have had to start with a larger initial amplitude A, or to have chosen to vary A instead of varying the damping factor, a.

One utilization for performance summaries, such as those shown in Fig. 9, is to determine, as a function of σ/λ, if the array element locations need be known or if the beamforming process can assume a linear array. As an example, given a one cycle deformed array and broadside arrivals, if no more than a 5 dB loss in signal gain is acceptable, then array element locations are needed when $\sigma/\lambda > 0.2$. If no more than 3 dB loss is tolerable, then the upper limit for assuming linearity is $\sigma/\lambda \cong 0.13$. Note that these limits are a function of array shape and that for broadside arrivals they are higher for one and one half cycle arrays and lower for damped and undamped half cycle arrays.

In all of the above cases, the sources are in the plane of the array. The variation of the results for sources above or below the plane of the array is also investigated. To reduce the number of cases, a fixed value of $\sigma/\lambda = 0.3$ is chosen. Arrays of one half cycle, a full cycle, and one and a half cycles are considered. Source cases include azimuthal angles of 10° and 90° from endfire, with an elevation angle of 10°. These results are not plotted because, as anticipated, the dB losses are only slightly larger than those for sources in the horizontal plane. In all three situations, any observed change in dB loss is of the order 1×10^{-4}. (The largest observed change is 3×10^{-4} dB, for a full cycle, beamformed as if linear.) These effects should be more pronounced for larger values of σ/λ, i.e., sinusoidal arrays of larger amplitudes, and also for larger elevation angles.

3 dB WIDTHS

Other degradations which can arise in the beamforming process for deformed arrays are an increase in the source peak beamwidth and raised sidelobes. Beamforming with the known phone locations, however, gives source peaks which correspond closely, in terms of 3 dB width, to those source peaks which a linear array would produce for the small deformations considered here. For the ambiguous peaks, on the other hand, the broadening is large and the ratio of the 3 dB width of the false peak to that of the true peak may be taken as another measure of left-right ambiguity

discrimination. In Fig. 10, we give this ratio, as a function of σ/λ, for all three undamped cases with broadside arrivals and for the undamped half cycle with a 10° arrival. For broadside incidence, the ambiguous peak-true peak width ratio increases rapidly with increasing σ/λ to a value of 30 to 35 at $\sigma/\lambda = 0.3$ for all three shapes. It is possible that at small deformations this ratio may offer improved left-right discrimination in contrast to the difference in signal gain for sources at broadside in some applications. For the half cycle and a source at 10°, however, the beamwidth ratio is almost constant at one, versus σ/λ, and so would not serve as a useful discriminant. The dB widths of the broken ambiguous peaks have been determined as accurately as possible without recourse to curve fitting and may be subject to small errors.

One can also consider the source peak width for shape - unknown beamforming as a measure of performance degradation by comparing it to the beamwidth for the source peak in the corresponding linear array response. Although we do not show these results, significant source peak broadening may be observed in the shape - unknown response patterns of Figs. 5 through 7. It should be noted, however, that the shape - unknown source peak widths are smaller for all these examples than the width of the ambiguous peak in the associated shape - known response. Therefore, in this limited range of calculations, the ratios shown in Fig. 10 are larger than would be found on a performance graph for shape - unknown source peak width ratios. This result is not surprising, since the phase errors for the ambiguous peak are in a sense twice those of shape unknown beamforming. Performance curves for source peak broadening as a result of assuming linearity serve as a measure, which, along with the loss in array signal gain, can be used to determine the largest acceptable value of σ/λ for shape - unknown beamforming.

PEAK SHIFTS

For small values of σ/λ, incorrectly assuming a linear array may result in only small dB losses. In these instances, one may choose to accept this degradation. As Hinich and Rule[1] and Hodgkiss[2] point out, however, there can still be a bearing error of 1° to 2°. This bearing error arises from the splitting of the source peak into two or more subpeaks, the largest of which is not centered with respect to the peak spread. For the deformed array responses shown in this paper, only damped half cycle responses are included for deformations with σ/λ less than 0.3. In Fig. 7 (b) $\sigma/\lambda = 0.1$ and the peak is already asymmetrical, although not highly broken. For $\sigma/\lambda = 0.2$ the response shown in Fig. 7 (d) is split into two parts with a minimum between them at the correct source bearing. The broadside $\sigma/\lambda = 0.3$ peaks, shown for various array shapes in Figs. 5 (b) and 6 (b) and (d), exhibit behavior ranging from a simple splitting into two parts to a highly broken and irregular shape. Thus it is understandable that even relatively small array deformations lead to bearing errors as large as approximately half the source peak width in shape - unknown

beamforming. Hinich[10] and Bouvet[3] (and references cited therein) discuss techniques for estimating the correct bearing.

CONCLUSIONS

We have shown that it is not difficult to build an algorithm for an exact (to within quantization and round-off error) model of damped sinusoidally deformed arrays of any whole or fractional number of cycles. Even though the model is not needed for very small array deformations, which may simply be calculated using Eq. (1), it is inexpensive enough to use for all deformatiion.

We have also investigated full 360° array responses for a variety of damped and undamped sinusoidally deformed 128 element arrays, including correct responses and those resulting from an incorrect assumption of array linearity. Undamped and damped 1/2 cycle arrays and undamped 1 cycle and 1 and 1/2 cycle arrays have been included. By examining various properties of these response patterns as a function of σ/λ, for various source directions, we have been able to summarize their performances both in the shape-known and shape-unknown applications.
In shape-known beamforming, the ability to discriminate true peaks from false peaks increases, as expected, as array deformation increases. Differences in array signal gain for these two peaks range up to 9 dB for $\sigma/\lambda = 0.3$ when the source is at broadside. For arrivals near endfire, however, the largest difference is just over 2.5 dB. In shape-unknown beamforming, the degradation in array signal gain ranges up to 7 dB at broadside but remains less than 1 dB near endfire.

We have also examined the 3 dB widths for the ambiguous peaks compared to the true peaks in shape-known beamforming. The ratio of these widths increases rapidly with σ/λ, reaching a value of 35 at $\sigma/\lambda = 0.3$ for the one cycle array at broadside. The shape-unknown peak broadening is also significant, but less than that of the ambiguous peak, as we have explained. Near endfire the broadening is negligible for both types of beamforming for the domain of σ/λ considered.

Straightforward measures of array signal gain changes and peak widths are difficult to apply due to the broken nature of the peaks with the resolution capability of 128 phones. This problem also leads to errors of bearing estimation. We have suggested various techniques for dealing with this problem.

The model admits of ready extension to two and three dimensional array geometries, and it is anticipated that these will be examined in the future.

ACKNOWLEDGEMENTS

The authors wish to acknowledge the support of the Naval Underwater Systems Center and of the Office of Naval Research through the NORDA Defense Sciences Program (61153N). We are extremely grateful to Mr. Art Collier of the Defence Research Establishment Atlantic for supplying BEAMSTATPAK, a powerful and general computer software package for modeling acoustic signal and noise fields and for beamforming. We have had helpful discussions with Don Murphy of NORDA and Jeff Becklehimer of Syntek, Inc. (currently with NORDA).

References

1. M. J. Hinich and W. Rule, "Bearing estimation using a towed array," J. Acoust. Soc. Am. 58, 1023 -1029 (1975).

2. W. S. Hodgkiss, "The effects of array shape perturbation on beamforming and passive ranging," IEEE J. Oceanic Eng. OE - 8, 120 - 130 (1983).

3. M. Bouvet, "Beamforming of a distorted line array in the presence of uncertainties on the sensor positions," J. Acoust. Soc. Am. 81, 1833-1840 (1987).

4. L. Ginzkey, "Influence of sensor position errors on spatial signal processing algorithms, " in Proceedings of NATO ASI on Adaptive Methods in Underwater Acoustics, Luneburg, Germany, 30 July-10 August 1985, edited by H. Urban (Reidel, Dordrecht, 1985), pp. 477-482.

5. D. Butler, "Beamforming with a distorted towed array," in Proceedings of NATO ASI on Adaptive Methods in Underwater Acoustics, Luneburg, Germany, 30 July-10 August 1985, edited by H. Urban (Reidel, Dordrecht, 1985), pp. 469-475.

6. C. Lee, "A modeling study on steady-state and transverse dynamic motion of a towed array system," IEEE J. Oceanic Eng. 3, 14-21 (1978).

7. J. Ketchman, "Vibration induced in towed linear underwater array cables," IEEE J. Oceanic Eng. 6 (3), 77-86 (July 1981).

8. W. Brandenburg, "A point mechanical model for the dynamics of towed arrays," Proceedings of ICASSP 84, San Diego, California, 1984, pp. 40.3.1-40.3.4.

9. A. J. Collier , "BEAMSTATPAK: A Fortran Beamforming and Statistics Modeling Package for Sonar Arrays," Defence Research Establishment Atlantic Technical Communication (in preparation).

10. M. J. Hinich, "Bearing estimation using a perturbed linear array," J. Acoust. Soc. Am. 61, 1540 - 1544 (1977).

Figure Captions

Fig. 1. The coordinates of a deformed array which is a half cycle of a sine curve. The array consists of 128 hydrophones and a VIM. The known arclength between two phones is used to calculate the (x,y) coordinates of each phone. Coordinates are given in units of d, the phone spacing. The amplitude of the deformation for this case is 10d. The position of the 75th phone is indicated. Note that different scales are used for the ordinate and the abscissa.

Fig. 2. The absolute error in the x coordinate of the phones resulting from the assumption of equal spacing d along the x axis. The error is given in terms of the phone spacing, d, as a function of phone number. The array shape is assumed to be an undamped half cycle sine, including a VIM, with the indicated total array deformation amplitude for each error curve. The deformation amplitudes are given as multiples of d and range from 0.5d to 4.0d.

Fig. 3. Representative array geometries. The first and last phones and every eighth phone are shown. Array dimensions are given in units of phone spacings. (a) Linear array; (b) undamped half cycle, amplitude 2.13d; (c) undamped full cycle, amplitude 1.47d; (d) undamped cycle and a half, amplitude 0.87d; (e) damped half cycle, maximum amplitude 1.55 at x = 57.5d; (f) damped half cycle, maximum amplitude 0.95d at x = 42.6d.

Fig. 4. Linear array responses for sources at (a) 90°, (b) 45°, and (c) 10° from endfire.

Fig. 5. Undamped half cycle (Fig. 3b) deformed array response. Amplitude of deformation is 2.13d and σ/λ is 0.3. Responses (a), (c), and (e) are obtained when the correct phone locations are used, and (b), (d), and (f) result when the arrays are incorrectly assumed to be linear. Source is at (a) and (b) 90°, (c) and (d) 45°, and (e) and (f) 10°.

Fig. 6. Undamped one cycle, (a) and (b), and one and one half cycle, (c) and (d), deformed array responses for a source at 90°. Deformation amplitude for one cycle is 1.47d and for one and one half cycles is 0.87d. σ/λ for both cases is 0.3. (a) and (c) are the responses when the correct phone locations are used, and (b) and (d) are those corresponding to a linear array shape assumption. Array shapes are shown in Figs. 3(c) and (d).

Fig. 7. Damped half cycle deformed array response for a source at 90°. (a) and (b) are for a shape determined by A = 2.13d, a = 0.0069, and σ/λ = 0.2 (Fig. 3e), while (c) and (d) are for an array with A = 2.13d, a = 0.020, and σ/λ = 0.1 (Fig. 3f). The array responses for the

known shape appear in (a) and (c) while the shape unknown (linear assumption) responses are in (b) and (d).

Fig. 8. Performance curves for peak height difference in left-right ambiguity removal of deformed arrays with known element locations. Amount by which left (ambiguous) peak is down from right (true) peak is given in dB versus σ/λ for sources at 10° (□), 30° (O), 45° (Δ), 60° (+), and 90° (X). Performance in (a) is for damped half cycle deformed arrays with A = 2.13d and selected values of σ/λ achieved by varying a. In (b), (c), and (d), σ/λ is adjusted by varying A for one half cycle, one cycle, and one and one half cycle deformed arrays, respectively.

Fig. 9. Performance curves of peak height degradation for deformed arrays assumed to be linear. Loss in array signal gain of deformed arrays is given as the power loss in the source peaks, in dB, relative to the corresponding peaks for a linear array, versus σ/λ for sources at 10° (□), 30° (O), 45° (Δ), 60° (+), and 90° (X). Performance in (a) is for damped half cycle deformed arrays with A = 2.13d and selected values of σ/λ achieved by varying a. In (b), (c), and (d), σ/λ is adjusted by varying A for one half cycle, one cycle, and one and one half cycle deformed arrays, respectively.

Fig.10. Left - right ambiguity beamwidth discrimination. The beamwidth ratio, defined as the false peak 3 dB width over the true peak 3 dB width, for deformed arrays beamformed with array element locations known, versus σ/λ. Results for a one - half cycle array (□), a full cycle array (Δ), and a one and a half cycle array (X) for sources at broadside. Results for a half cycle array (O), for a source at 10°.

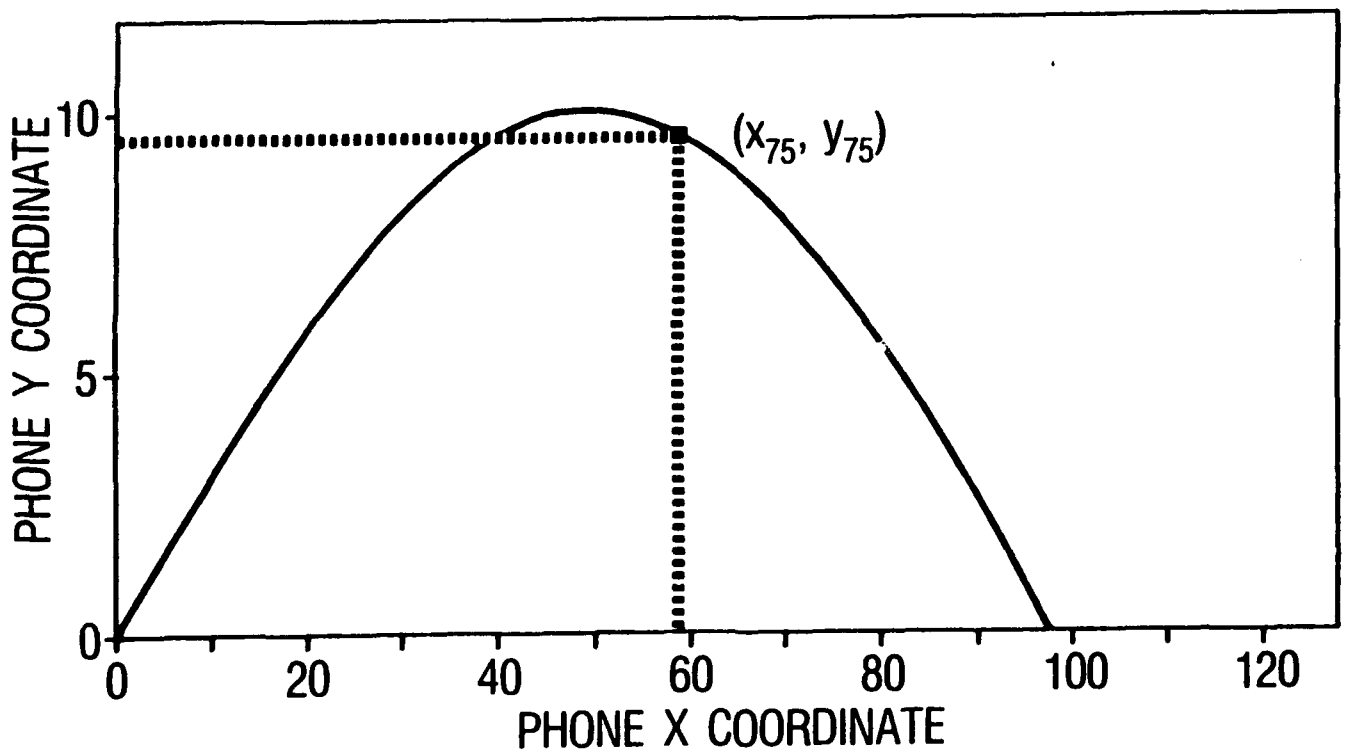
PHONE Y COORDINATE
10
5
0
(x_{75}, y_{75})
0
20
40
60
80
100
120
PHONE X COORDINATE

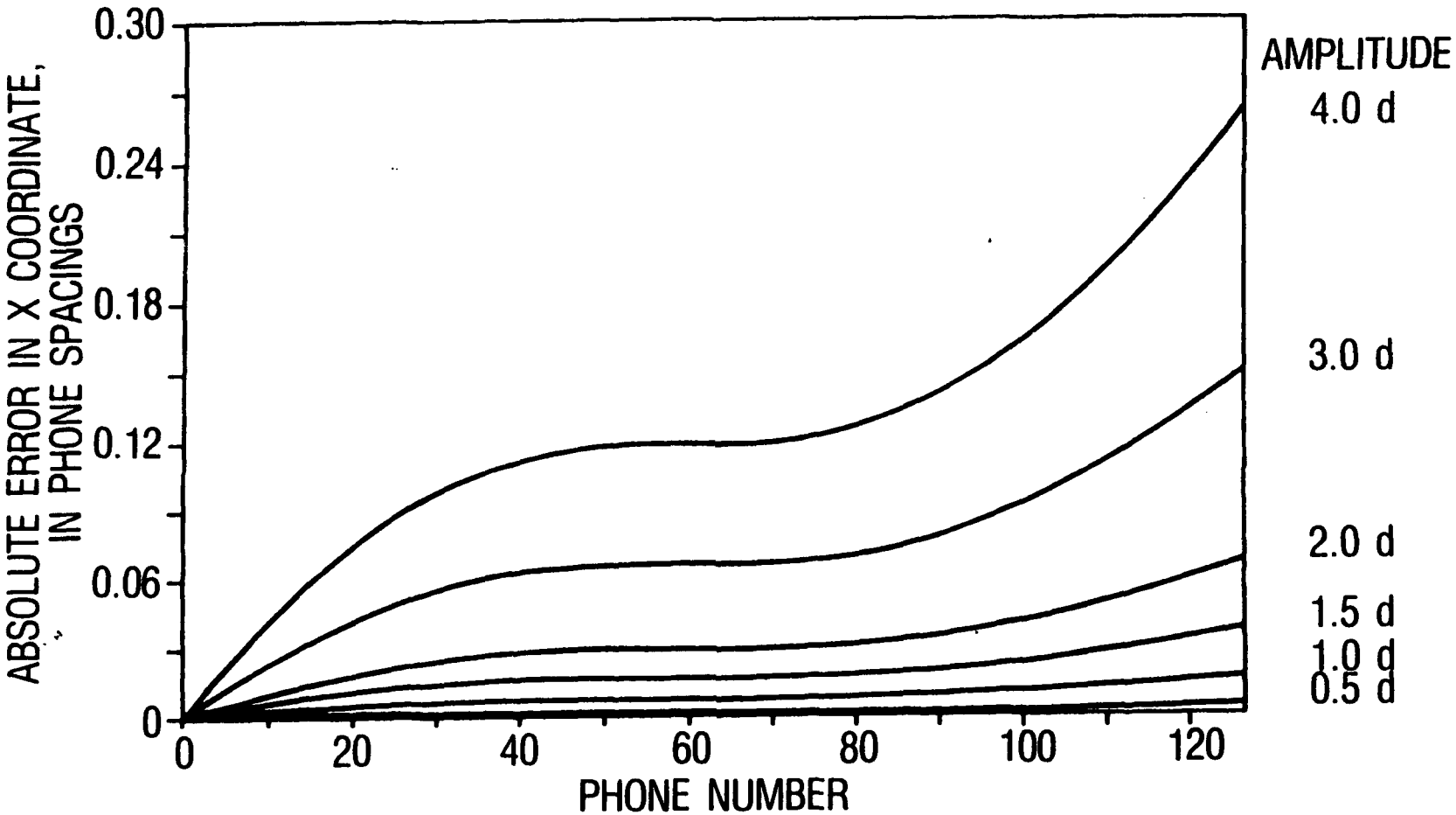
ABSOLUTE ERROR IN X COORDINATE, IN PHONE SPACINGS
0.30
0.24
0.18
0.12
0.06
0
0
20
40
60
80
100
120
PHONE NUMBER
AMPLITUDE
4.0 d
3.0 d
2.0 d
1.5 d
1.0 d
0.5 d

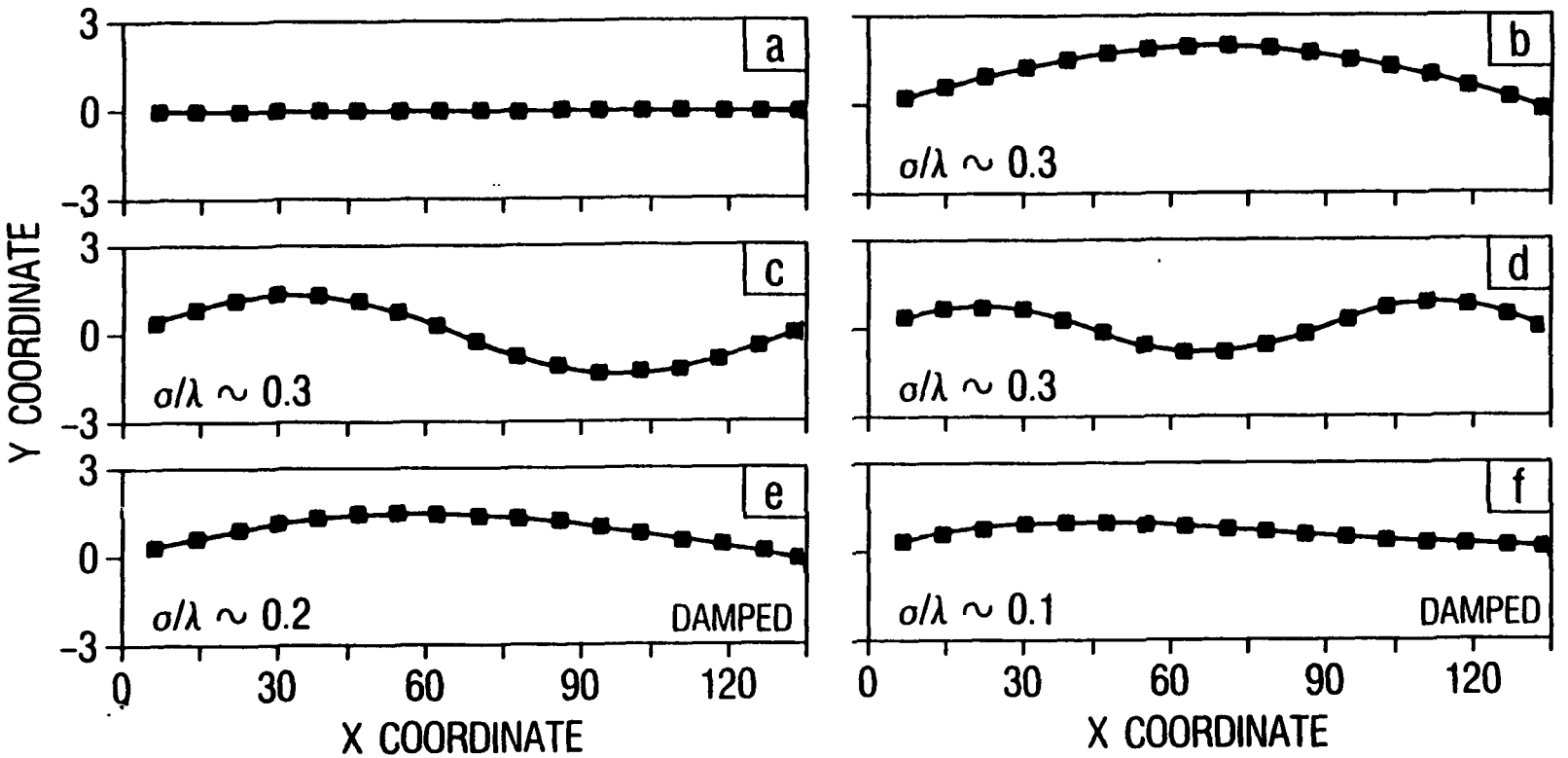
a
b
c
d
e
f
3
0
-3
σ/λ ~ 0.3
σ/λ ~ 0.3
σ/λ ~ 0.2
DAMPED
σ/λ ~ 0.1
DAMPED
Y COORDINATE
0
30
60
90
120
X COORDINATE
X COORDINATE

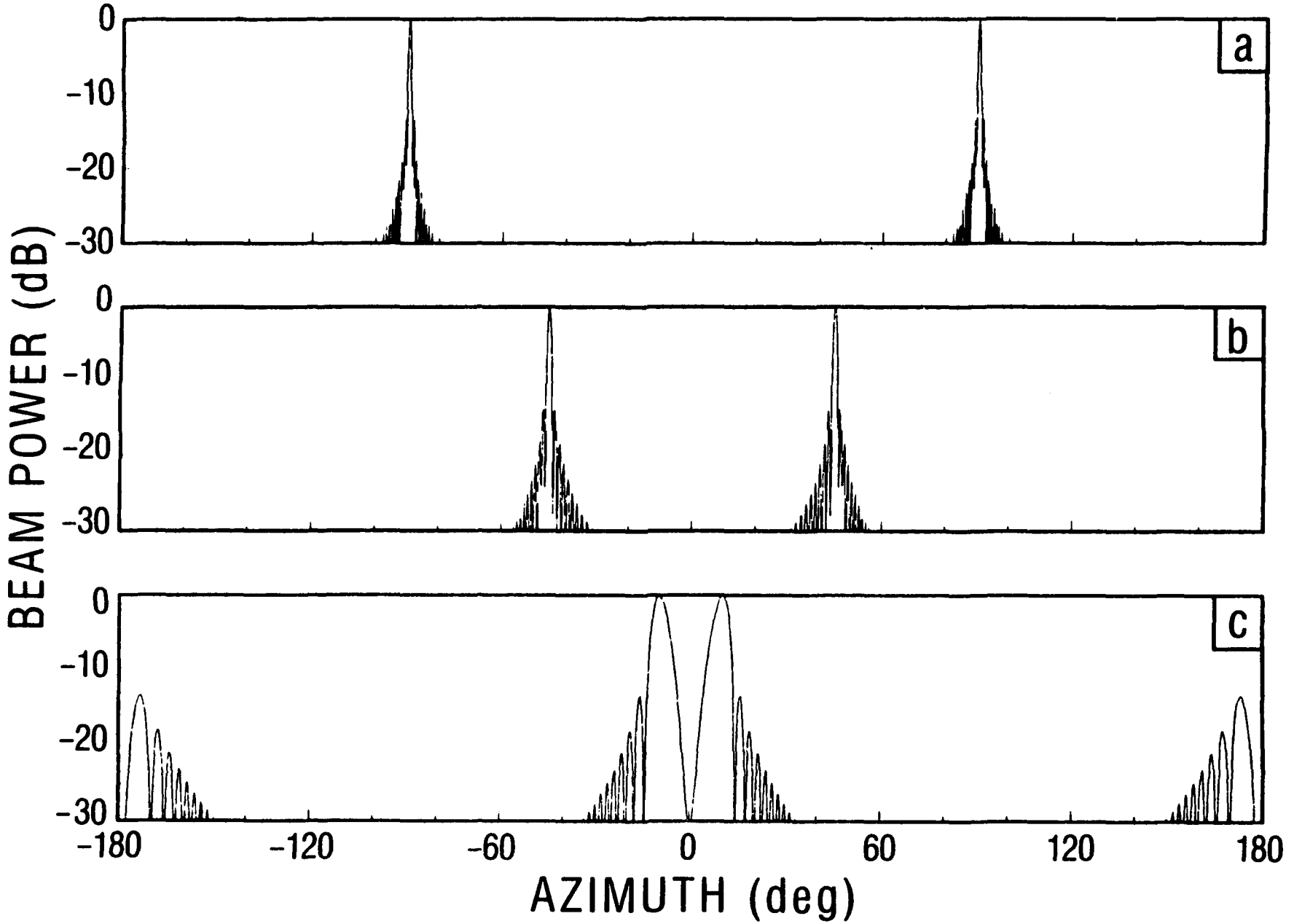
BEAM POWER (dB)
0
-10
-20
-30
a
b
c
-180
-120
-60
0
60
120
180
AZIMUTH (deg)

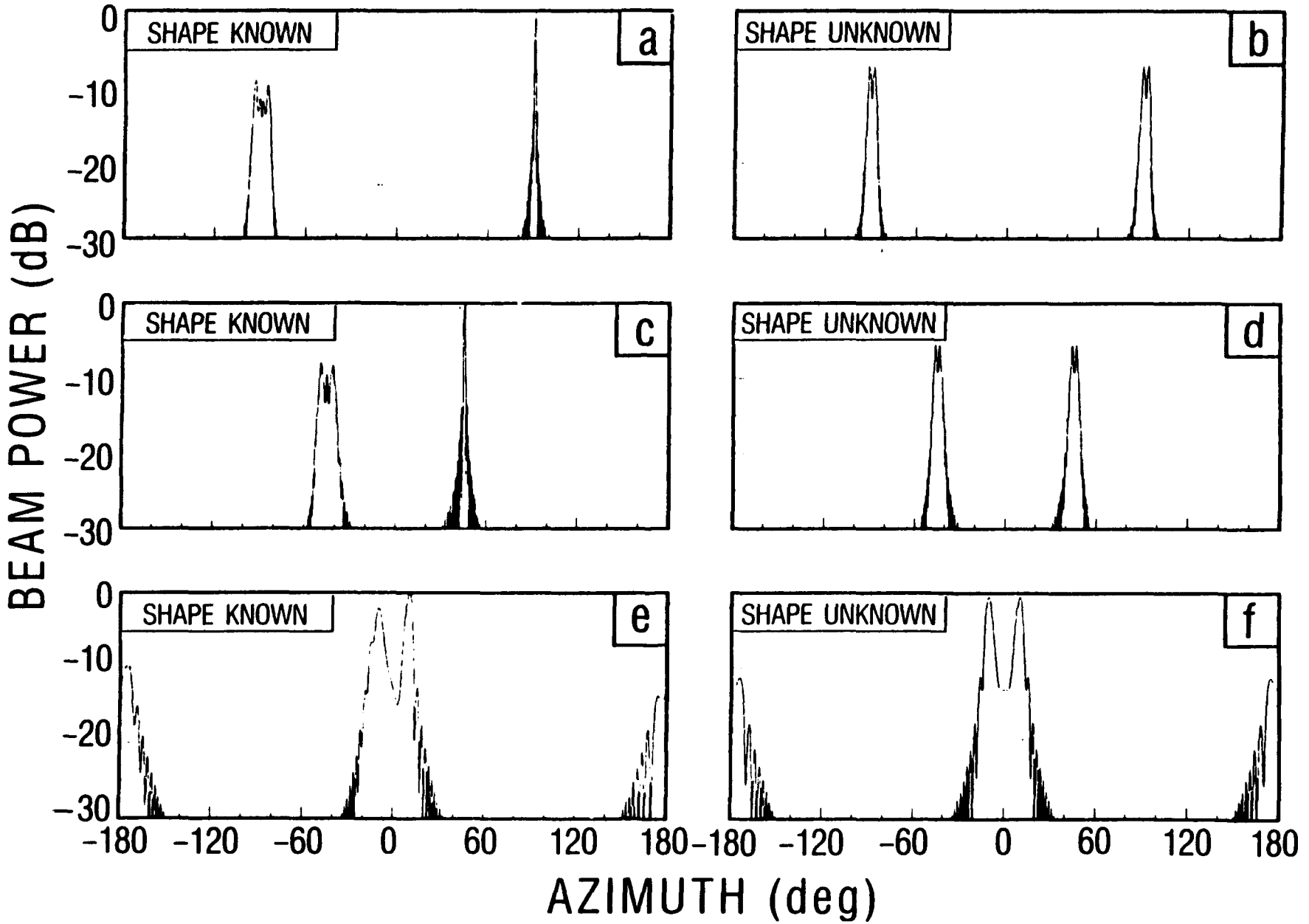
SHAPE KNOWN
a
SHAPE UNKNOWN
b
SHAPE KNOWN
c
SHAPE UNKNOWN
d
SHAPE KNOWN
e
SHAPE UNKNOWN
f
0
-10
-20
-30
BEAM POWER (dB)
-180
-120
-60
0
60
120
180
AZIMUTH (deg)

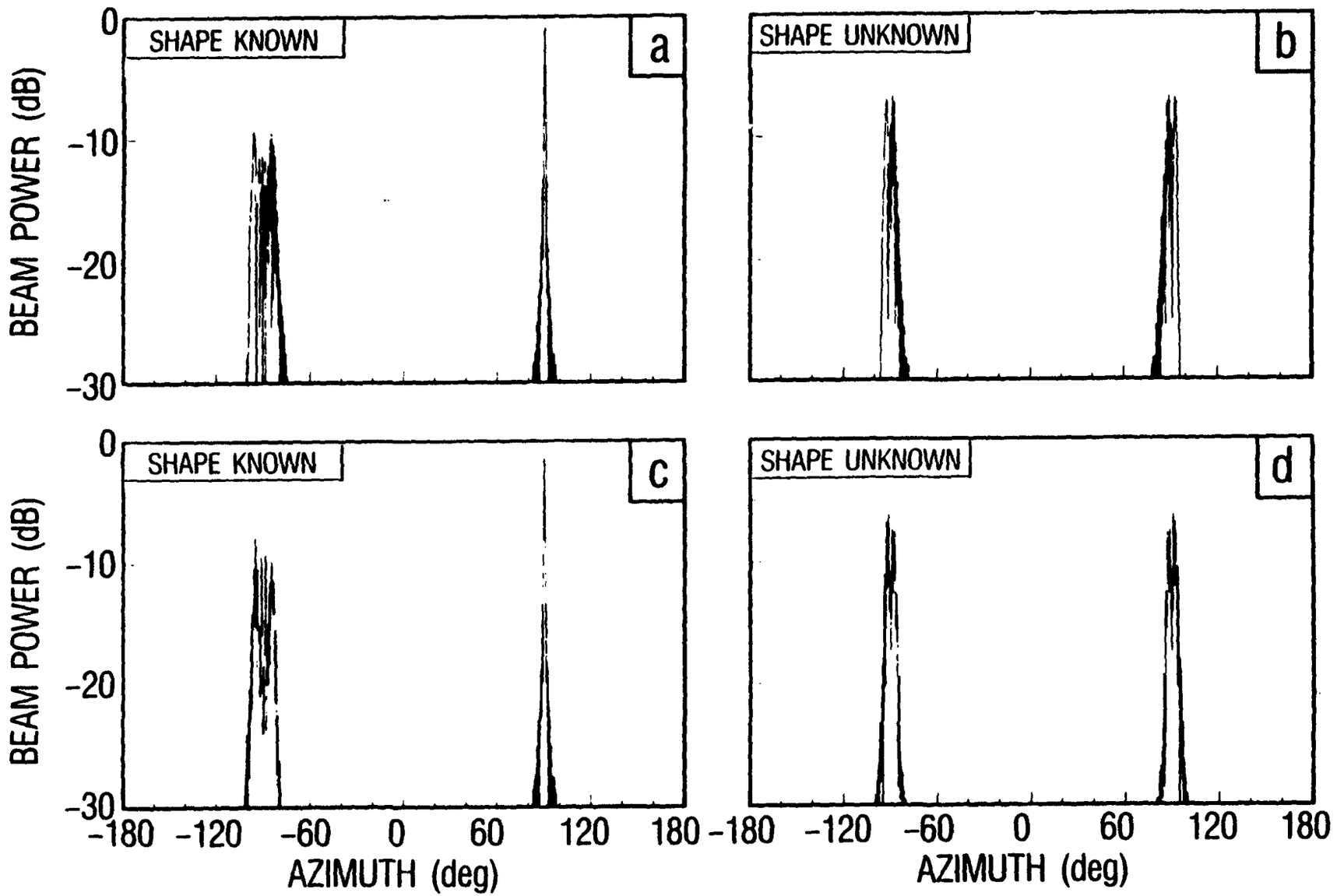
SHAPE KNOWN
a
SHAPE UNKNOWN
b
SHAPE KNOWN
c
SHAPE UNKNOWN
d
BEAM POWER (dB)
0
-10
-20
-30
-180
-120
-60
0
60
120
180
AZIMUTH (deg)

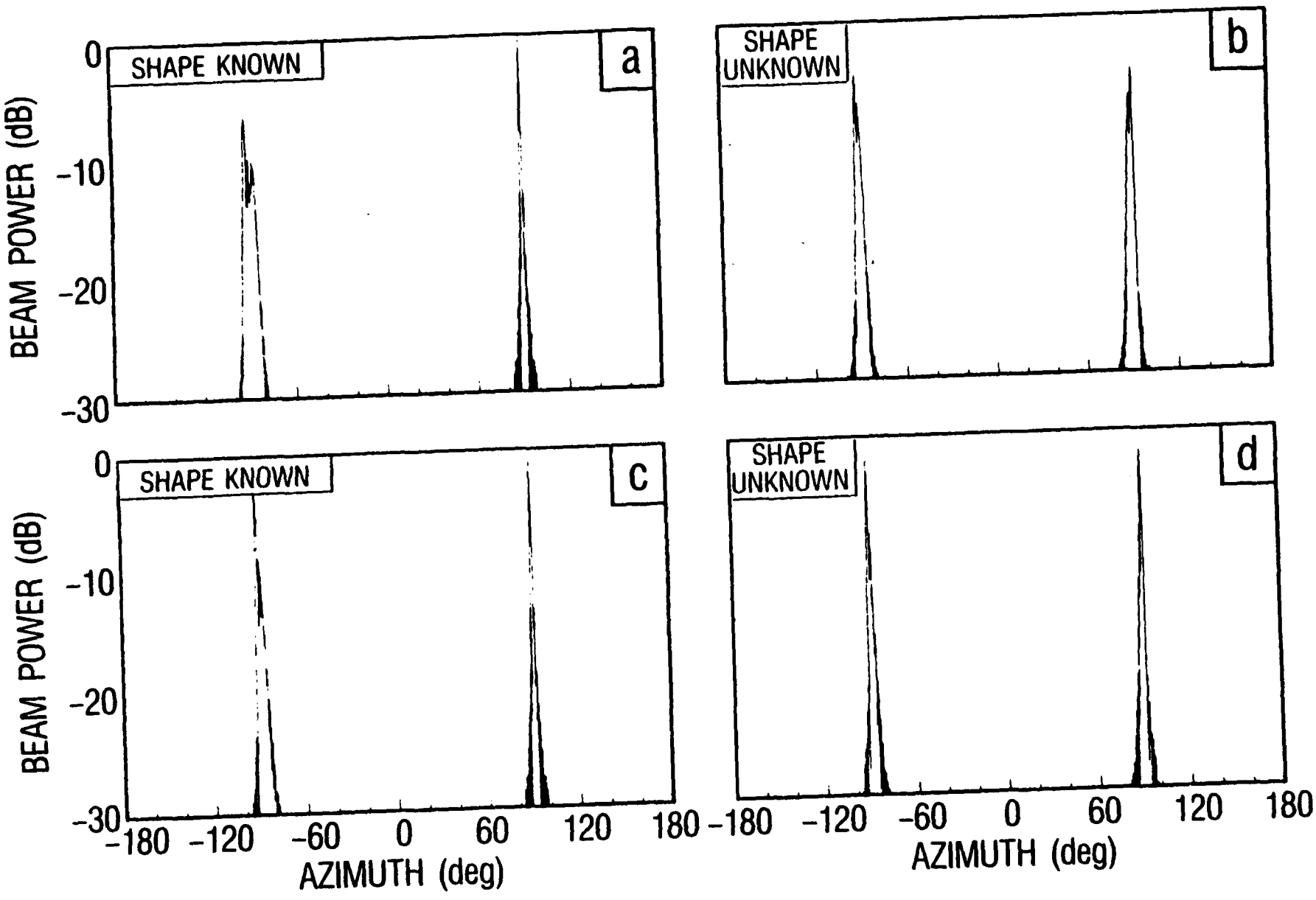
SHAPE KNOWN
a
SHAPE UNKNOWN
b
SHAPE KNOWN
c
SHAPE UNKNOWN
d
BEAM POWER (dB)
0
-10
-20
-30
-180
-120
-60
0
60
120
180
AZIMUTH (deg)

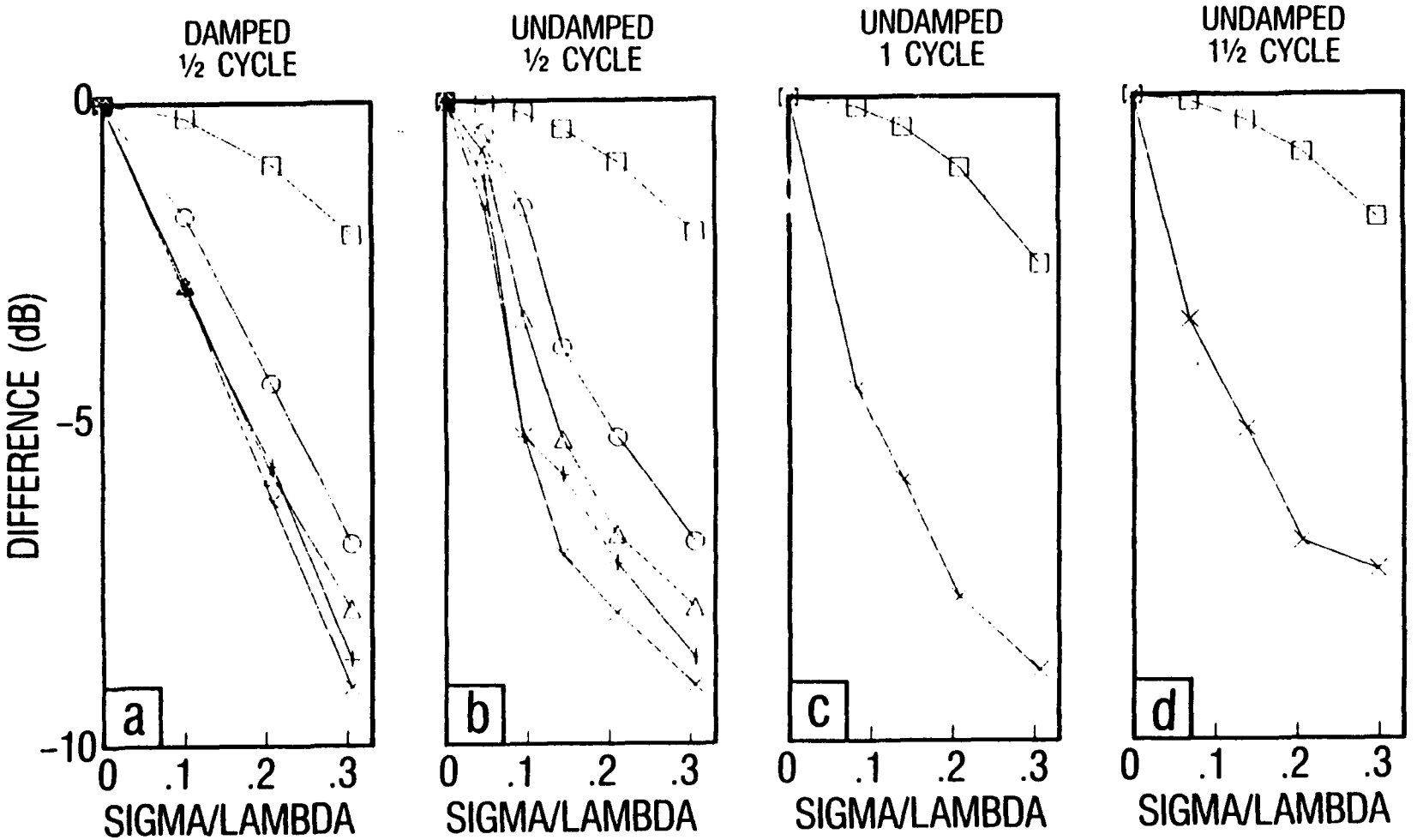
DAMPED
½ CYCLE
UNDAMPED
½ CYCLE
UNDAMPED
1 CYCLE
UNDAMPED
1½ CYCLE
DIFFERENCE (dB)
0
-5
-10
a
b
c
d
0 .1 .2 .3
SIGMA/LAMBDA

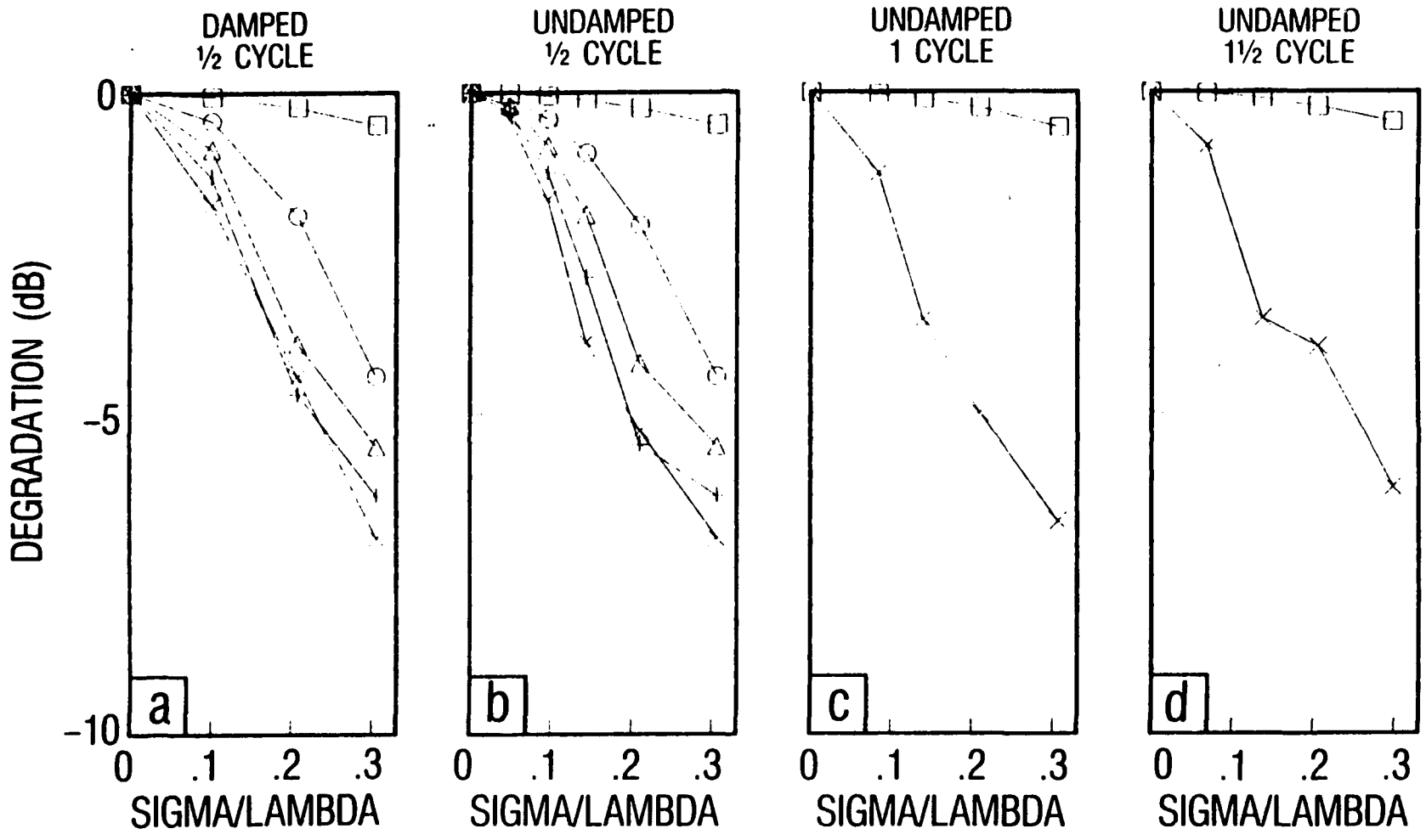
DAMPED
½ CYCLE
UNDAMPED
½ CYCLE
UNDAMPED
1 CYCLE
UNDAMPED
1½ CYCLE
DEGRADATION (dB)
0
-5
-10
a
b
c
d
0
.1
.2
.3
SIGMA/LAMBDA

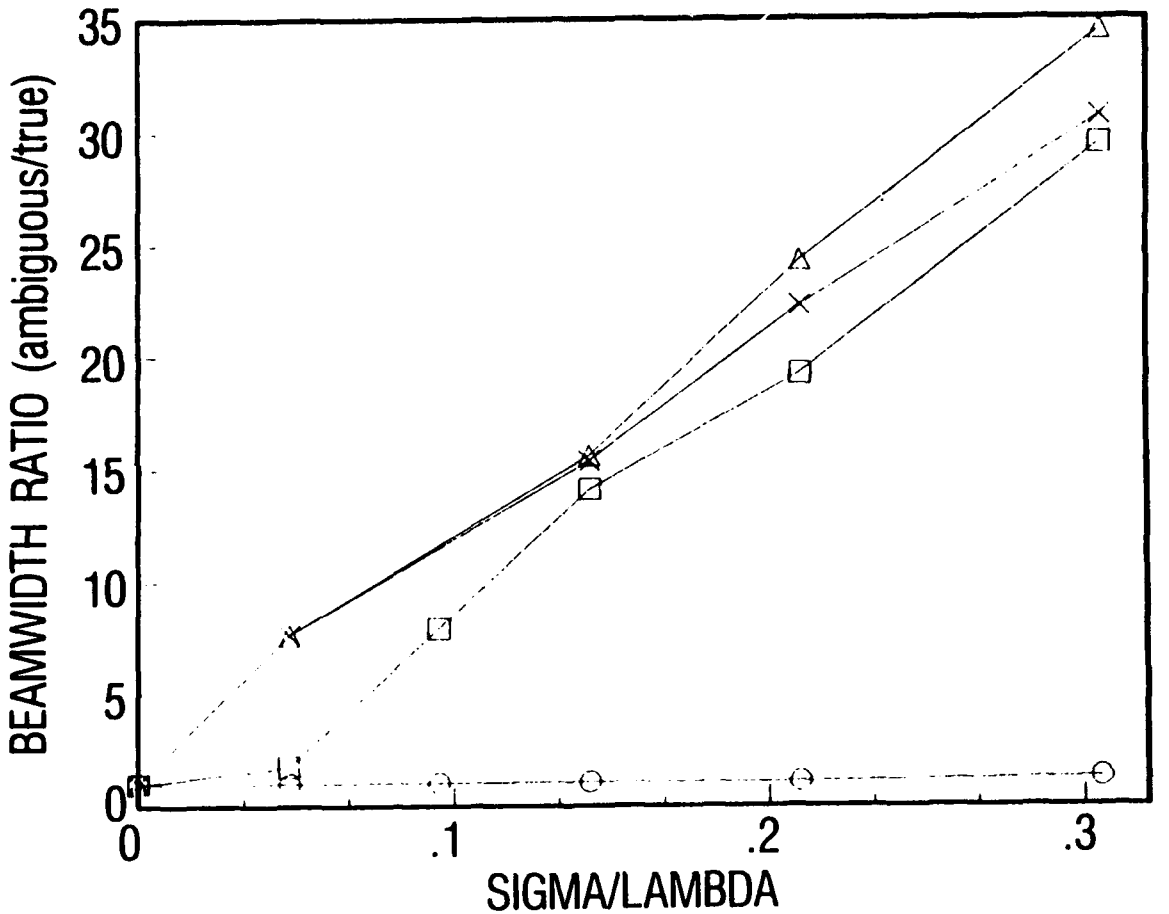
BEAMWIDTH RATIO (ambiguous/true)
35
30
25
20
15
10
5
0
0
.1
.2
.3
SIGMA/LAMBDA

Nonorthogonality of measured normal modes in shallow water

Grayson H. Rayborn
Department of Physics and Astronomy
University of Southern Mississisippi, Hattiesburg, MS 39406-5046

George E. Ioup and Juliette W. Ioup
Department of Physics and Geophysical Research Laboratory
University of New Orleans, New Orleans, LA 70148

ABSTRACT

Several investigators have demonstrated that measured mode nonorthogonality, among other factors, can make processing of shallow water vertical array data by use of modal compositions an improvement over processing in the space of the original pressure measurements. The potential for improvement using this technique is greatest when the nonorthogonality of the measured modes is largest, although the success of the transformation to modal amplitude space is governed by the condition of the transformation matrix. We have cast the Helmholtz equation for the Pekeris model in dimensionless form and studied the amount by which the measured normal modes fail to be orthogonal for a variety of ocean bottoms, array lengths and discretizations, and array positions. Environments are selected to reflect sediment types characteristic of the continental shelf using an inverse linear relationship which we show exists between water-to-bottom density and velocity ratios for the data of Hamilton. The nonorthogonality is found to be substantial and to exceed previous estimates for some cases even when the entire water column is spanned by a dense array. We have found that matched field processing using modal composition is likely to offer the most improvement over conventional matched field processsing for water depths and frequencies at and just above modal onsets, for sound speed ratios close to one, and for arrays which span

only a fraction of the water column. For full water column span discrete arrays with one more phone than mode, there is a zone of orthogonality covering one third to one half the possible depth and frequency combinations for all cases studied.

INTRODUCTION

Propagation of sound in shallow water is commonly analyzed in terms of normal modes, i.e., collective oscillations of the entire body. It is not always remembered that the oscillating body is composed of the water column and the sediment beneath it, not just of the water column alone. The importance of these oscillations in sound propagation in the bottom is more easily understood for those normal modes whose depth eigenvalues form a continuum since these modes correspond to pairs of travelling waves which are largely absorbed and only partially reflected when they strike and penetrate the bottom, and these bottom oscillations correspond to the energy lost to the bottom. The importance of the bottom oscillations for sound propagated by trapped normal modes is less easily perceived since these modes are totally reflected from the bottom and therefore largely constitute the pressure field in the water column at appreciable distances from the source. Nonetheless, the bottom is oscillating and this oscillation is important in the sense that the energy in the bottom prevents even the trapped normal modes from being orthogonal on the water column, a fact that was recognized by Pekeris in his seminal study of the transmission of sound in shallow water.[1] Since this early work numerous investigators have detected, separated, and measured normal modes.[2-7]

Despite the emphasis that Pekeris gave to the fact that the

normal modes were orthogonal only when both the water column and bottom were considered, mode filtering experiments in the past frequently assumed that the nonorthogonality was not important and approximated the depth eigenfunctions as orthogonal on the water column alone. Estimates of the error induced by this assumption have occasionally been made. Ferris[2] has measured the mode nonorthogonality under unspecified conditions and found it to range from -10 dB to -30 dB of the measure mode. Clay et al.[8] have termed this error "mode leakage" and found it to vary from 3 to 10 percent using a nine-element vertical array in a water tank with a sand bottom overlying concrete when three normal modes were present. An important exception to the usual assumption of orthogonality is found in the experiments and analysis of Tindle et al.[6] These investigators propose forming a matrix of the sampled depth eigenfunctions and computing its inverse when the number of phones and modes are equal. When there are more phones than modes, they form a square matrix by multiplying by its transpose to extract an inverse of the resulting depth eigenfunction matrix. The importance of this inverse has been recognized by recent investigators who term it a mode filtering processor and use it to map the pressures measured on the hydrophones into a space which describes modal compostions for the purpose of estimating the range and depth of sources in waveguides by matched field processing.[5,9] In this paper we review the connection between nonorthogonality and modal composition space processing and present a uniform and systematic approach to understanding the degree of nonorthogonality of the measured modes and, therefore, some of the conditions under which it is important to use this type of processing.

I. THEORY

A. Nonorthogonality and its relation to matched field processing

In the following we treat the assumption of orthogonality, not the approximations of the environment and the solution of the Helmholtz equation, each of which is an important topic treated elsewhere. Consider a vertical array of N hydrophones when M trapped modes are present, such that $M \leq N$. Let the depth eigenfunction for the m^{th} mode be $U_m(z)$ so that the complex pressure produced by the m^{th} mode at the n^{th} hydrophone is

$$p_m(z_n) = U_m(z_n)\ b_m(r_o,z_o) \quad , \tag{1}$$

where r_o and z_o are the range and depth of the source, b_m is a complex multiplicative factor for the m^{th} mode at this source range and depth, and z_n is the depth of the n^{th} hydrophone. The form of b_m may be found in standard treatments of solutions of the Helmholtz equation.[10,11] To determine the modal composition of the measured complex pressure field, prior knowledge of the environment is used to calculate a theoretical depth eigenfunction, $U_m(z)$, from the Helmholtz equation by means of any of several commonly used computer algorithms. The measured pressure can then be projected onto the calculation of the measured eigenfunction to give $a_m(r_o,z_o)$, an approximation to $b_m(r_o,z_o)$:

$$a_m(r_o,z_o) = \sum_{n=1}^{N} p(z_n)\ U_m(z_n) \quad . \tag{2}$$

The integrity of this method is based on the assumption that the pressure field can be expressed as a linear

combination of these environmentally determined, numerically approximated eigenfunctions, and that they are orthogonal on the interval sampled by the hydrophones so that the inner product sum is

$$Z_{mm'} = \sum_{n=1}^{N} U_m(z_n)\ U_{m'}(z_n) = \delta_{mm'} \quad . \tag{3}$$

The expansion may then be written as

$$p(z_n) = \sum_{m=1}^{M} U_m(z_n)\ a_m \quad . \tag{4}$$

If the assumption of orthogonality applies for the calculated discrete depth eigenfunctions, then the matrix Z, whose entries are $Z_{mm'}$, is an identity matrix, and

$$a_m = \sum_{n=1}^{N} p(z_n)\ U_m(z_n) = \sum_{m'=1}^{M} Z_{mm'}\ b_{m'} = b_m \quad . \tag{5}$$

The M X M matrix Z is not ordinarily an identity matrix, however, since measured fractional span discrete approximations to the eigenfunctions are normally not orthogonal. Even so the modal amplitudes b_m can be extracted correctly by computing the inverse of Z, since $Z^{-1}Z$ will still be an identity matrix. In this case we have

$$b_m = \sum_{m'=1}^{M} (Z^{-1})_{mm'}\ a_{m'}$$

$$= \sum_{m'=1}^{M} \sum_{n=1}^{N} (Z^{-1})_{mm'}\ p(z_n)\ U_{m'}(z_n) \tag{6}$$

and

$$p(z_n) = \sum_{m=1}^{M} U_m(z_n)\ b_m \quad . \tag{7}$$

Tindle et al.[6] appear to be the first to suggest an approach to processing which does not rest on the assumption of orthogonality. They define a matrix U whose mn^{th} entry is the value of the m^{th} eigenfunction at the location of the n^{th} hydrophone. Thus, the columns of this matrix are vectors, each of which is composed of samples taken from a depth eigenfunction sampled at the hydrophone locations. This matrix defines a transformation from a vector space of modal compositions to a vector space of measured complex pressures, as in Eq. (7) above. Tindle et al.[6] and subsequent investigators[5,9] have shown that, under certain conditions, there exist significant advantages associated with using an inverse mapping to go from the space of measured complex pressures to the space of modal compositions. The problem with defining an inverse mapping is that the U matrix is generally not square. The Moore-Penrose pseudoinverse[12] may be calculated to accomplish the inverse mapping, however, and when $N > M$ it provides the theoretical best least-squares solution for the modal composition. Hence, as in Eq. (6),

$$b = (U^{\dagger}U)^{-1} U^{\dagger} p \quad , \tag{8}$$

in which we have dropped summation notation in favor of the less cumbersome matrix form and show the commonly used $U^{\dagger}U$ for the matrix Z, where $\dagger$ represents the conjugate transpose.

The potential advantage of processing in modal composition space can be seen by considering the conventional matched field processor in the complex pressure space, $\langle |p^{\dagger}(r_o,z_o)p'(r,z)|^2 \rangle$, with $p(r_o,z_o)$ the measured or true field vector and $p'(r,z)$ the calculated field vector for a source at (r,z). If this processor is

represented in terms of modal composition vectors, we have[5,13]

$$\langle |p^{\dagger} p'|^2 \rangle = p^{\dagger} \langle p' p'^{\dagger} \rangle p$$

$$= b^{\dagger} U^{\dagger} R U b \quad , \qquad (9)$$

where R is the cross-spectral matrix of the complex pressures and $b(r_o, z_o)$ is the vector of true modal amplitudes corresponding to the noise-free measured field. As has been shown by Shang[5] and Yang,[9] matched field processing can be considerably improved when it is performed in the space of modal compositions. This processing is specified by $\langle |b^{\dagger}(r_o, z_o) b'(r,z)|^2 \rangle$, with $b'(r,z)$ the vector of modal amplitudes for a source at (r,z). Writing the innermost product explicitly in terms of the transformation from pressure space, this becomes

$$\langle |b^{\dagger} b'|^2 \rangle = \langle b^{\dagger} Z^{-1} U^{\dagger} p' \, p'^{\dagger} U Z^{-1} b \rangle$$

$$= b^{\dagger} Z^{-1} U^{\dagger} R U Z^{-1} b \quad . \qquad (10)$$

The amount by which the processor in Eq. (10) differs from that in Eq. (9) is governed by the deviation of Z^{-1}, and hence Z, from the identity matrix. If, in fact, the measured eigenfunctions are orthogonal so that Z is the identity matrix, the processors are identical. The degree of advantage to be gained by proceeding to this modal composition space processing, then, is determined at least in part by the degree of nonorthogonality of the measured eigenfunctions. It is known that the depth eigenfunctions will be orthogonal if they are densely enough measured on the entire span of water plus bottom. Because hydrophone arrays rarely extend below the water column and are usually sparsely spaced, the amount of nonorthogonality among the

modes can vary greatly with environment and array configuration. It is our purpose to investigate the behavior of the nonorthogonality in shallow water for bottoms consisting of a variety of sediment types and for dense and sparse arrays spanning part or all of the water column. The above discussion does not consider the effects of noise or nonlinear processing nor the condition number of the transformation, which governs the degree to which modal compositions can be recovered.

B. Dimensionless Analysis for Normal Modes

We wish to demonstrate the amount of nonorthogonality in the modes and its effect on the Z matrix by use of a simple model, one that still permits the insertion of realistic bottom velocities and densities, parameters whose contribution to nonorthogonality we wish to investigate. To this end we have adopted the Pekeris model[1] with constant velocities in the water column and in the sediment and no shear in the bottom. The fraction of the eigenfunction in the water column depends on the wavelengths of the depth eigenfunctions (the mode wavelengths) in the water column, which are determined for a given bottom type by the product of the linear frequency of the source and the water depth divided by the speed of sound in the water. This fraction, then, does not depend solely on the depth of the water column nor the frequency of the source. Thus, for our model, a water depth of 50 m and a source frequency of 100 Hz produce the same nonorthogonality between modes for a given bottom type as a water depth of 100 m and a source frequency of 50 Hz if the slight difference in relative densities due to the depth difference is ignored. Consequently, to present our results in a form that has the

greatest possible usefulness, we have defined dimensionless variables by dividing the lengths in the problem by $(\lambda/2\pi)$, where λ is the wavelength of the sound in water and $c_1/\omega = \lambda/2\pi$. The angular frequency of the source is ω, and c_1 is the speed of sound in the water column. Thus, we make the following definitions:

$\zeta = \omega z/c_1$ is the dimensionless distance below the surface, and

$\alpha = \omega H/c_1$ is the dimensionless depth of the water column.

Using the standard separation for the homogeneous Helmholtz equation with the assumption of cylindrical symmetry,[14] the equation for the depth eigenfunctions is

$$d^2U/dz^2 + (\omega^2/c^2 - k_r^2)U = d^2Z/dz^2 + k_z^2Z = 0 \quad , \qquad (11)$$

where k_r, the separation constant, is the horizontal component of the wave vector, k_z is the vertical component, and c is the speed of sound in the medium. We use the subscript 1 to denote parameters in the water column and 2 for those in the bottom. In terms of the newly-defined dimensionless variables, the differential equation becomes, after factoring out ω^2/c_1^2,

$$d^2U/d\zeta^2 + (c^2/c_1^2 - K^2)U = 0 \quad , \qquad (12)$$

with $K = k_r(c/\omega)$. For the two media this becomes

$$\begin{aligned} d^2U/d\zeta^2 + (1 - K^2)U &= 0 \quad \zeta < \alpha \\ d^2U/d\zeta^2 + (c_r^2 - K^2)U &= 0 \quad \zeta > \alpha \end{aligned} \qquad (13)$$

with $c_r = c_1/c_2$, the relative velocity of sound in the two media. Since we are interested in trapped modes, we desire solutions for which $c_r^2 < K^2 < 1$. Application of the usual boundary conditions leads to

discrete values of K and of $k = (1 - K^2)^{1/2} = (c/\omega)k_z$, which satisfy the transcendental equation

$$\tan k_m\alpha = - (D_r k_m)/[(1 - c_r^2) - k_m^2]^{1/2} \quad , \tag{14}$$

where $D_r = D_2/D_1$, the relative density of the two media (in the opposite sense to c_r). The depth eigenfunctions before normalization and matching boundary conditions are given by

$$\begin{aligned} U_m(\zeta) &= \sin k_m\zeta \qquad 0 < \zeta < \alpha \\ U_m(\zeta) &= \exp(-[(1 - c_r^2) - k_m^2]^{1/2}\zeta) \quad \zeta > \alpha \quad . \end{aligned} \tag{15}$$

C. Measured normal mode nonorthogonality

As discussed previously, it was recognized by Pekeris that the orthogonality of normal modes exists on the entire span of water column plus bottom.[1] This orthogonality applies for continuous eigenfunctions defined on this span. It is therefore expected that when only the water column, or part of the water column, is sampled discretely by an array of hydrophones, the measured normal modes will not be orthogonal. Since our intention is to study this phenomenon, we next develop equations to calculate nonorthogonality in the Pekeris model for given bottom types, array lengths and placements, and distribution of hydrophones in the array.

Since the nonorthogonality may be due to any of the above causes we suggest the following terminology to describe its sources. For a dense array which spans the entire water column, the nonorthogonality is due to neglecting the portion of the eigenfunction in the sediment, and we use the name "water column span nonorthogonality." If only a part of the water column is spanned with

a dense array, we refer to the effect as "fractional span nonorthogonality." The overlap of differing eigenfunctions due to approximating a dense array with a sampled array we refer to as "discretization nonorthogonality," i.e., the replacement of the integral with a Riemann sum. The usual measurement will contain nonorthogonality due to more than one of these sources, and this work contains studies when various combinations are present.

Since the measurements due to a dense array are adequately approximated with a continuous model for the eigenfunctions, we begin by calculating the nonorthogonality in the integral formulation. The overlap of any two eigenfunctions on the water column is given by

$$I_{mn} = \int_0^{\alpha} \sin k_m \zeta \sin k_n \zeta \, d\zeta \quad . \tag{16}$$

It is important to normalize this overlap in calculating the nonorthogonality. There is some arbitrariness in the choice of the normalization. Since we are only interested in working in the water column, we choose to normalize by the geometric mean of the areas under the continuous eigenfunctions involved in the overlap integral. This gives entries of one on the main diagonal of the Z matrix. It ignores the fraction of energy which is in the bottom. Bottom abosrption also affects the amount of each mode present, but transmission loss is not included here. Our calculated nonorthogonalities indicate the size of the off-diagonal elements relative to diagonal elements of equal size because of the normalization used. Since in practice the diagonal elements are not generally all equal, our results would have to be scaled with the inverse of the geometric mean of the diagonal elements

calculated with normalized eigenfunctions to correspond to the energy partitioning of the propagating modes. Our normalization corresponds to that used by Clay et al.[8] We then define the nonorthogonality between the modes m and n as

$$A_{mn} = I_{mn}/[I_{mm}I_{nn}]^{1/2} \quad . \tag{17}$$

The integral I_{mn} has particularly simple form:

$$I_{mn} = \frac{\sin(k_m - k_n)\alpha}{2(k_m - k_n)} - \frac{\sin(k_m + k_n)\alpha}{2(k_m + k_n)} \qquad m \neq n \tag{18}$$

and

$$I_{nn} = \alpha/2 - \sin(2k_n\alpha)/4k_n \quad . \tag{19}$$

For partial span nonorthogonality, we evaluate the integral of Eq. (16) from α_1 to α_2 to obtain

$$I_{mn} = \frac{\sin(k_m - k_n)\alpha_2}{2(k_m - k_n)} - \frac{\sin(k_m + k_n)\alpha_2}{2(k_m + k_n)} - \frac{\sin(k_m - k_n)\alpha_1}{2(k_m - k_n)} + \frac{\sin(k_m + k_n)\alpha_1}{2(k_m + k_n)} \qquad m \neq n \tag{20}$$

and

$$I_{nn} = \alpha_2/2 - \sin(2k_n\alpha_2)/4k_n - \alpha_1/2 + \sin(2k_n\alpha_1)/4k_n \quad . \tag{21}$$

When the number of hydrophones is not dense and the continuous model no longer suffices, we evaluate instead a sum over hydrophones to determine the overlap:

$$I_{mn} = \sum_{i=1}^{N} \sin(k_m\zeta_i)\,\sin(k_n\zeta_i)\,\Delta\zeta_i \quad , \tag{22}$$

where N is the number of phones.

With these expressions it is possible to investigate in a systematic fashion the amount contributed to nonorthogonality by all of the above factors. Since all of the assumptions depend on the sound speeds and densities in the bottom, of which there are many possible combinations, it is necessary to limit these variables to a reasonable number while treating to the extent feasible commonly found combinations in shallow water. We have found a method using the data of Hamilton[15] to accomplish this, and discuss it in the next section. For the sound speed and density combinations selected, we then show the water column span nonorthogonality as a function of α for all modal combinations through six modes. We then examine for two bottom types fractional span nonorthogonality as a function of α for dense arrays which span the top, middle, and bottom half of the water column, as well as a few other fractional spans. We show one case in which the array size is held constant as α is varied. Next the discretization nonorthogonality for full and partial water column span for a dense array of 25 phones is presented. The sparse array cases range from the number of hydrophones equal to the number of modes to twice the number of modes for the largest α's included.

II. SOUND SPEEDS AND DENSITIES

Hamilton[15] has studied density and compressional sound velocity in common marine sediments. We wish to investigate possible relations between the sound speeds and densities reported by Hamilton for the purpose of selecting representative cases. To this end we have plotted the relative density, D_r, defined by the ratio of the density in the bottom to the density in the water versus the ratio of the sound speed in water to that in the bottom, c_r, in Fig. 1. Although this method of

defining sound speed and density ratios is chosen to reflect the way the quantities appear in the Helmholtz equation, Eq. (13), these definitions prove fruitful because the data of Hamilton then fall very close to two straight lines, as shown in Fig. 1. Separate straight lines have been fitted to (A) the data for the sands and silts without clays, and (B) the data for the clays with sands and silts, using weighted linear regression with the weights determined by the errors given by Hamilton.[15] The data for the clays were fit by the equation

$$D_r = -4.08\, c_r + 5.50 \quad , \tag{23}$$

and the data for the sands and silts by

$$D_r = -2.69\, c_r + 4.24 \quad . \tag{24}$$

The absolute densities measured by Hamilton were divided by 1.02293, the specific gravity of seawater at a depth of 50 m at standard salinity, to produce the relative densities used in the plots. It was necessary to fix a water density in order to proceed with the calculations, and the density at 50 m was chosen as a reasonable compromise over the continental shelf. Although in general the relation of density to sound speed is expected to be complex,[16] the fact that the measurements of Hamilton are characterized by such a simple relation implies that a significant part of the sediments may be treated assuming a linear relation between the relative densities and sound speeds. Several benefits accrue from this assumption. One advantage is that a few density and sound speed combinations may be chosen to span the sediments of interest. One might expect results between these points to vary smoothly from one case to another because of the linear relationship. The equations which describe the propagation of normal modes can be reduced by one parameter by

employing the relation between the density and the sound speed to eliminate one of the variables. Finally, the measurements of Tindle et al.[6,7] have shown that it can be difficult to make shipboard determinations of densities, although sound speeds may be fairly accurately determined. If it is known that the sediment is among the types characterized by Hamilton, these relations can possibly be used to determine densities from measured sound speeds in the bottom more accurately than they can be measured at sea. The laboratory experiments of Tindle et al.[17,7] are done with a sand whose density and sound speed fall close to the fitted straight line of the sands. This data point is shown as a triangle in Fig. 1.

The data points of Hamilton[15] are shown as rectangles in Fig. 1. The values selected to represent the sand and silt sediments for the results shown in the following figures are indicated with open circles. Three values, (0.847,1.96), (0.909,1.79), and (0.926,1.75), were chosen from the sand and silt straight line using the linear regression Eq. (24). For the clays the representative value of (0.990,1.46) was chosen from Eq. (23). More sand and silt sediments than clayey sediments are chosen because of the predominance of sand sediments on the continental shelves.

III. Measured mode nonorthogonality

A. Full water column span

Water column span nonorthogonality refers to the nonorthogonality resulting when a dense array spans the entire water column. This nonorthogonality results because the part of the eignfunction which extends into the bottom is ignored. In general it is not possible to

overcome this nonorthogonality without sampling the pressure field in the bottom, although certain depth, frequency, and environmental combinations may have modal orthogonality for a specific sampling. The nonorthogonality for the canonical cases mentioned previously has been calculated using Eq. (17) for all mode combinations through the sixth mode, as a function of the scaled depth alpha. The results are given in Figs. 2-5, which show with a continuous line the percentage nonorthogonality for each case versus alpha. (The symbols represent the results for a discrete 25-phone array, which will be discussed later.) The general features of all four figures are similar. The domain of the scaled depth alpha from the onset of the second mode to the onset of the seventh mode differs, however, from one case to the next. These are the alpha values required to produce all the combinations for nonorthogonality when six or fewer modes are present. Below the onset of the second mode there is only one mode present, so no nonorthogonality exists. Fig. 2 shows the nonorthogonality for the sand with the highest sound speed and largest density (c_r = 0.847, D_r = 1.96). Depending on the choice of water depth and source frequency, the nonorthogonality can be seen to range from approximately 17 percent at the onset of the second mode to less than a percent for the mode combinations with the least overlap prior to the onset of the seventh mode. Nonorthogonality is greatest at the onset of a new mode for the combinations involving the highest modes. At onset the nonorthogonalities between the established modes and the new mode increase with the mode number of the previously present mode. Nonorthogonalities involving established modes at the onset of a new mode increase with the product of the mode numbers. The curves of nonorthogonality occasionally but rarely cross. When they do, they

always involve a new mode and an established mode and are accomplished before the onset of the next mode for all cases studied here. Thus, just before the onset of a new mode the magnitude of the nonorthogonalities is ordered by the product of the mode numbers.

Further inspection of Fig. 2 reveals that the maximum error at onset decreases uniformly as the number of the new mode increases. For example, the maximum nonorthogonality at the onset of the sixth mode is just over ten percent, compared to the almost 17 percent nonorthogonality at the onset of the second mode. Both positive and negative percentages have been given, according to the sign of the overlap between the two modes. The overlap is seen to be positive for the n(n - 1) mode combination, and negative for the n(n - 2) mode combination, and continues to alternate. The relative minimum in the amount of nonorthogonality occurs just before the onset of a new mode. The largest value of nonorthogonality before onset ranges from approximately 3.5 percent below the third mode onset to just over 4 percent below the seventh mode onset.

The next higher velocity sand results are plotted in Fig. 3. This sand has $c_r = 0.909$ and $D_r = 1.79$. Essentially all the observations for the previous figure hold for this one, with some slight changes in the percentages. For example, the maximum error is almost 18 percent for this case.

Figure 4 shows the results for the lowest velocity sand considered, $c_r = 0.926$ and $D_r = 1.75$. Again changes from the highest velocity sand discussion are small. For this sand the maximum nonorthogonality is just over 18 percent.

Although the general features of Fig. 5, the clay-silt-sand

with $c_r = 0.99$ and $D_r = 1.4608$, are similar to the other three figures, there are several important differences worth noting. The scaled depth alpha domain needed to cover the region from the onset of the second mode to that of the seventh mode is considerably greater than that of the sands. The maximum nonorthogonality is greater by a larger margin than the small differences among the other cases. The nonorthogonality between the first and second mode at the onset of the second mode is over 20 percent. This is the largest nonorthogonality we have observed for a full water column span with a dense array in the cases considered. The smallest maximum nonorthogonality at onset, which occurs at the onset of the sixth mode, is over 13 percent.

The magnitude of nonorthogonality for different mode combinations depends on the density of the sediment, but when allowance is made for modal onset the shape and position of the nonorthogonality curves are very similar. This is illustrated by defining a parameter

$$\gamma = \alpha [1 - c_r^2]^{1/2} \quad . \tag{25}$$

Modal onsets occur at the same value of this parameter since, as Eq. (14) demonstrates, the onset of a new mode, corresponding to another root of the equation, is determined by the asymptote of the right side of the equation, which occurs at $k_n = [1 - c_r^2]^{1/2}$. Thus the onset of modes occur for the same value of γ, namely $\gamma = (n - 1/2)\,\pi$, regardless of the bottom type. Figure 6, which shows the percentage modal nonorthogonality as a function of γ, demonstrates that in terms of γ the nonorthogonalities are nearly the same for all bottom types studied.

B. Fractional water column span

When only part of the water column is spanned by a dense array

the nonorthogonality might be expected to be larger than that which occurs for full water column span. Indeed it is found that nonorthogonalities can approach 100 percent in magnitude when the array lengths are small. There are, however, isolated occurrences of zeros in the overlap integral, so some modal combinations can have less nonorthogonality when measured by a fractional span array than those resulting from an array that fully spans the water column. In order to investigate this phenomenon while keeping the number of cases considered to a reasonable number, we limit our study to the two examples with extreme velocity/density ratios, the sand with $c_r = 0.847$ and $D_r = 1.96$, and the clay with $c_r = 0.990$ and $D_r = 1.461$.

We consider the fractional water column span nonorthogonality from three perspectives:

(1) For selected values of the scaled depth α, we show nonorthogonality as the fraction of the water column spanned increases with (a) the array centered in the middle of the water column, (b) the array growing from the top of the water column, and (c) the array growing from the bottom of the water column.

(2) As a function of the scaled depth α, we show the nonorthogonality when the top, middle, and bottom half of the water column are spanned by an array.

(3) For an array chosen arbitrarily to be half the water column depth at the initial scaled depth α, the nonorthogonality is examined as α increases and the array length is held constant for arrays centered in the water column, beginning at the top of the water column, and beginning at the bottom of the water column. This simulates using a fixed vertical array in water of increasing depth at constant

frequency or increasing the frequency for a fixed length array at a constant depth.

Figures 7 through 12 show sample results corresponding to perspective (1). The nonorthogonality percentages for arrays growing outward from the middle of the water column, for scaled depth α values selected to have six modes present, are shown in Figs. 7 and 8 for the sand and clay examples, respectively. At the right edge where the arrays span the full water column, the nonorthogonalities agree with those shown for these alpha values in Figs. 2 and 5. At the left edge of the curves, where only 0.05 of the water column is spanned, the nonorthogonalities are between 90 and 100 percent in magnitude for all mode combinations. The overlaps between any two modes are not in general expected to vary monotonically with increasing fraction of α spanned by the array due to the oscillatory character of the modal functions. It is not surprising, therefore, that many of the curves of Figs. 7 and 8 have local maxima, some more than one. The maximum nonorthogonality present, however, does decrease monotonically as the fraction of α spanned increases.

The same discussion can be applied to the nonorthogonality for arrays growing down from the top of the water column, as shown in Figs. 9 and 10. The major difference is that the nonorthogonality magnitude starts at 100 percent for arrays which span 0.05 of the water column, and it does not decrease below 90 percent for any combination until 0.2 of the column is spanned. This result obtains because all modes have a node at the surface of the water column, and there is no cancellation of negative and positive area in the overlap until a node of one of the pair of modes is reached. Since there is not a node of the depth eigenfunctions at the bottom of the water column, this

feature does not appear in Figs. 11 and 12, which show the nonorthogonality for arrays which grow from the bottom of the water column. For arrays which grow from the bottom up, the maximum nonorthogonality decreases more rapidly than it does for the other two array starting points, although the maximum nonorthogonality does not decrease monotonically, possessing three local minima. The last local minimum, which occurs when the array length spans approximately 94 percent of the water column from the bottom up, has a smaller value for the extreme nonorthogonality than the full water column span. This result is one facet of a feature of these figures which is not present for the other two cases. Because the modal eigenfunctions are truncated at the bottom before reaching a node, whereas they end at the top of the water column at a node, an array growing from the bottom reaches a depth symmetric with the bottom cutoff before reaching the top of the water column. One would therefore expect that for many mode combinations the nonorthogonality would increase as the array grows from this point to the top of the water column. The point at which many mode nonorthogonalities start to increase for the case in Fig. 11 is at 90% span and for Fig. 12 at about 88% span.

The nonorthogonalities in perspective (2) are shown in Figures 13 through 18. Figures 13 and 14 show the nonorthogonality for arrays spanning the middle half of the water column as the scaled depth α increases from the onset of the second mode to the onset of the seventh mode for the sand and clay examples, respectively. When only half the water column is spanned, the nonorthogonalities can be much larger than those of the full water column span, with percentages as high as 85% observed. The percentages for different modal overlaps vary greatly

from one to another, and some decrease with increasing α, while others increase with increasing α. These behaviors can be understood from an examination of the overlap of the modal eigenfunctions for the two modes in question as α increases. The results suggest one reason that arrays spanning a large fraction of the water column are needed to produce high-quality ambiguity surfaces, as reported by Heitmeyer and Hamson.[18] There is no α value on these graphs for which large nonorthogonalities are not present. The sand and clay results are qualitatively similar, although detailed curve shapes and percentages differ for some overlaps.

Figures 15 and 16 show the results corresponding to 13 and 14, but with the array spanning the top half of the water column rather than the middle. The maximum nonorthogonality is even larger for these arrays, approaching 100% in the case of the first and second mode overlap. Whereas the largest nonorthogonalities above the third mode onset corresponded to negative overlaps for arrays in the middle of the water column, in Figs. 15 and 16 these occur for positive overlaps. Again, some nonorthogonalities increase with increasing α and some decrease.

The last set of graphs for perspective (2) are Figs. 17 and 18, which show the nonorthogonalities for arrays in the bottom half of the water column. Maximum nonorthogonalities for arrays in the bottom half are less than 80% in magnitude. Like the arrays in the middle of the water column, the largest nonorthogonalities occur for overlaps which are negative. The curves for the overlaps of the newly onset modes with the two mode numbers just below them appear to be mirror images of each other about a line of symmetry which varies from about -37% to about -30%.

Finally, perspective (3) nonorthogonalities are presented in Figs. 19 thru 24. For this perspective an array length is chosen which spans half the water column at the onset of the second mode. This array length is held fixed while the scaled depth α is increased. As new modal onsets are reached, additional nonorthogonalities are shown on the graph. The increasing of the scaled depth may be viewed as an increase in frequency or an increase in water depth, as discussed above. The change in nonorthogonality with frequency and depth could be an important factor in the design of experiments with fixed array length. Figures 19 and 20 give the resulting nonorthogonalities when the constant array has its center at the center of the water column for all scaled depths, for the sand and clay cases, respectively. Again, some nonorthogonalities increase with α while others decrease, at least initially after onset. The nonorthogonalities observed are generally large, some even approaching 100 percent. The nonorthogonalities of the first and second modes between themselves, however, are not larger than 80 percent, in contrast to Figs. 21 and 22, which have the constant array descending from the top of the water column. For this case, as might be expected from an examination of the modal eigenfunctions, the nonorthogonalities between modes one and two are close to 100 percent over the entire domain of α included. Many other large nonorthogonalities are also observed for the array at the top of the water column. Nonothogonalities never become smaller than 20 percent except for a single case at the onset of the sixth mode in the clay results of Fig. 22. In contrast to the nonothogonality behavior of the arrays which start at the top of the water column, those which start at the bottom, whose results are given in Figs. 23 and 24, have

nonorthogonalities which change signs as α increases. This means that there are regions of α for which some nonorthogonalities are small. The difference between the top and bottom behavior is explained by the different boundary conditions at the top and bottom, and the fact that a node is found in the eigenfunctions at the top of the water column whereas none of the eigenfunctions terminates in a node at the bottom of the water column.

C. Discretization

All calculations to this point have been done using a continuous model, i.e., an integral formulation to evaluate the nonorthogonality. This model is an excellent approximation if the hydrophones are densely enough spaced in the array. In all plots presented in this paper, the number of phones is held constant as α is increased. It is found over this range of α that the results for 50 phones are graphically indistinguishable from those of the continuous model. If instead 25 phones are used, the discrete results differ slightly for the highest modes from those of the continuous model. The 25-phone results are shown in Figs. 2 through 5 as the plotted points, and they may be seen to lie on the continuous lines which are the integral results except for the highest modes, for which they differ slightly. When the number of hydrophones is reduced to 12, the discrepancy between the dense array shown by the continuous lines in Fig. 25 and the discrete array indicated by the symbols, becomes more noticeable. Interestingly, for this case, the nonorthogonality is less for the discrete than for the dense array.

When the number of phones is equal to or only slightly exceeds the number of modes, the discrepancy between the continuous

array and a full-span six-phone array, shown in Fig. 26, is even more pronounced. Again, the dense array results are indicated by the continuous lines and the discrete array by the symbols. When the number of phones is one more than the number of modes, as is true for α values from 26.6 to 32.5 in Fig. 26, the nonorthogonality shows an interesting development. With a discrete array there exists a small range of α values for which the nonorthogonalities are almost zero for all mode combinations. In this figure, the α range corresponding to nonorthogonalities less than 1% is 29.6 to 32.5 at the onset of the next mode. An implication of this result for matched field processing will be discussed in later work. After the nonorthogonality reaches a minimum, which appears to occur just before the onset of the mode whose number is equal to the number of phones in the array, the nonorthogonalities of all mode combinations begins to increase rapidly with increasing α. Similar behavior has been observed for the other canonical cases. The existence of the large zone of nonorthogonality suggests that for between one-third and one-half of all water depth and frequency combinations for the range of α's studied, a discrete array can be designed for a given α for which all the measured modes are orthogonal to within 1%.

For discrete partial span arrays, the difference between continuous arrays and discrete arrays is generally smaller for a given number of phones than for full span arrays because the phone spacing is smaller. Six phone arrays which span half the water column show differences between discrete and continuous arrays comparable to the differences for 12 phone arrays which span the full water column.

SUMMARY

Full Water Column Span

Continuous

As long as there are more phones than modes, nonorthogonality is greatest near modal onset and decreases smoothly with increasing scaled depth. At a fixed scaled depth with few exceptions, and these occurring near modal onset, the greatest nonorthogonality occurs between modes whose modal numbers form the highest product. Indeed at a fixed scaled depth, modal nonorthogonalities are nearly ordered by this mode number product. Finally, although the maximum nonorthogonality is always greatest between the two highest modes, the amount of this maximum nonorthogonality decreases with increasing scaled depth from a maximum of 16% to 20%, depending on bottom type, for the nonorthogonality between modes two and one, to about 11% to 14% between modes six and five at onset.

Discrete

The nonorthogonality for the discrete case is visually indistinguishable from the continuous case as long as approximately twenty-five or more hydrophones are used for the six modes studied. In general, approximately four times as many phones as modes appear to be required for this conclusion. For fewer than 25 hydrophones the discrete results diverge from those for the continuous array, more so as the number of phones decreases. Surprisingly, the deviation is in the direction of decreased nonorthogonality for the discrete geometries tested. The most interesting manifestation of this increase in orthogonality with sparse spatial sampling is the existence of a domain

of values for the scaled depth α for which the nonorthogonality between modes almost vanishes for all modal pairs. For all bottom types studied, these zones of orthogonality occur just before the onset of the mode whose mode number is equal to the number of hydrophones in the array. The existence of the zones suggests that, for a given value of α, arrays can be designed to have measured mode orthogonality to within one percent for all modal combinations, over much of the α domain.

Partial Water Column Span

For arrays that span no more than one-half the water column, the nonorthogonality of all modal combinations is quite substantial, except for occasional near zero values for certain modal combinations for some particular fractional water column spans. Arrays that span 20% of the water column or less typically exhibit strikingly large modal nonorthogonalities, frequently 60 to 80 percent. Even for arrays that span as much as 90% of the water column, the nonorthogonality is increased substantially over the full span case, typically exhibiting nonorthogonalities of about 20%. These results, which were of course expected, seem to hold for arrays near the top, middle, or bottom of the water column. No zones of orthogonality were observed.

When arrays half the length of the water column were examined as α was increased, large nonorthogonalities were found for all but a few modal combinations regardless of the scaled depth α used or the placement of the array in the top, middle, or bottom of the water column. A curiously symmetrical distribution of nonorthogonalities for some modal combinations was observed.

These same substantial nonorthogonalities were observed when the perspective was changed and the nonorthogonalities calculated as the

actual array length, initially half the water column, was held constant and the scaled depth α increased. Almost all of the modal nonorthogonalities, which were 20% or more initially, increased as the scaled depth increased and the array length became a smaller fraction of the scaled depth.

Although the discrete cases we tested were limited, the use of a sparse array, one with only six phones for example, resulted generally in changes in nonorthogonality of the same order of magnitude as had been observed previously for 12 phones for full span arrays, as long as the number of phones exceeded the number of modes.

In conclusion, the largest nonorthogonalities were observed for partial span arrays, and these arrays are the ones most likely to benefit from proceeding to modal amplitude space for matched field processing. For full span arrays, the largest nonorthogonalities were found at and just above modal onset. These locally maximum nonorthogonalities decrease as the number of modes present increases, and they tend to be significantly smaller than the nonorthogonalities found with partial span arrays. A slight increase in nonorthogonalities was noted as the sound speed ratio approached one from below.

ACKNOWLEDGMENTS

The authors wish to acknowledge the advice and support of Donald R. Del Balzo of NORDA, helpful discussions with Charles Byrne of Lowell University, Christopher Feuillade and George Frichter of Syntek, George Smith of Xavier University, James Matthews of NORDA, and the expert computer assistance of Janet C. Carr of the University of Southern Misssissippi and N. B. Day of the University of New Orleans.

Research supported in part by the Naval Ocean Research and Development Activity through the U. S. Navy ASEE Summer Faculty Research Program and through NORDA Contract Number N00014-87-K-6002.

REFERENCES

[1]C. L. Pekeris, "Theory of Propagation of Explosive Sound in Shallow Water," Geol. Soc. Amer. Mem. 27, 1-117 (1948).

[2]R. H. Ferris, "Comparison of Measured and Calculated Normal-mode Amplitude Functions for Acoustic Waves in Shallow Water," J. Acoust. Soc. Am. 52, 981-988 (1972).

[3]F. Ingenito, "Measurements of Mode Attentuation Coefficients in Shallow Water," J. Acoust. Soc. Am. 53, 858-863 (1973).

[4]E.-C. Lo, J.-X. Zhou, and E.-C. Shang, "Normal Mode Filtering in Shallow Water," J. Acoust. Soc. Am. 74, 1833-1836 (1983); E. C. Shang, H. P. Wang, and Z. H. Huang, "Waveguide Characterization and Source Localization in Shallow Water Waveguides Using the Prony Method," J. Acoust. Soc. Am. 83, 103-108 (1988).

[5]E.-C. Shang, "Source Depth Estimation in Waveguides," J. Acoust. Soc. Am. 77, 1413-1418 (1985).

[6]C. T. Tindle, K. M. Guthrie, G. E. J. Bold, M. D. Johns, D. Jones, K. O. Dixon, and T. G. Birdsall, "Measurements of the Frequency Dependence of Normal Modes," J. Acoust. Soc. Am. 64, 1178-1185 (1978).

[7]C. T. Tindle, H. Hobaek, and T. G. Muir, "Normal Mode Filtering for Downslope Propagation in a Shallow Water Wedge," J. Acoust. Soc. Am. 81, 287-294 (1987b).

[8]C. S. Clay, Y.-Y. Wang, and E.-C. Shang, "Sound Field Fluctuations in a Shallow Water Waveguide," J. Acoust. Soc. Am. 77, 424-428 (1985).

[9]T. C. Yang, "A Method of Range and Depth Estimation by Modal Decomposition," J. Acoust. Soc. Am. 82, 1736-1745 (1987).

[10]L. E. Kinsler, A. R. Frey, A. B. Coppens, and J. V. Sanders, "Fundamentals of Acoustics," Wiley, third edition (1982), p. 434-440.

[11]L. M. Brekhovskikh, "Waves in Layered Media," Academic Press, second edition (1980), p. 409-414.

[12]A. S. Householder, "The Theory of Matrices in Numerical Analysis," Dover (1964), p. 9.

[13]C. L. Byrne, private communication (1987).

[14]Ref. 10, p. 430-433.

[15]E. L. Hamilton, "Geoacoustic Modeling of the Sea Floor," J. Acoust. Soc. Am. 68, 1313-1340 (1980).

[16]A. S. Ahuja, "A Review of Derivations of the Formulas for the Acoustical Properties of Liquid-Solid Mixtures," in "Physics of Sound in Marine Sediments," L. Hampton, ed., Plenum (1974), p. 1-17; P. J. Schultheiss, "The Influence of Packing Structure and Effective Stress on V_S, V_P, and the Calculated Dynamic and Static Moduli in Sediments," in "Acoustics and the Seabed," N. G. Pace, ed., Bath University Press (1983), p. 19-27; K. Attenborough, "Pore Shape and the Biot-Stoll Model for Saturated Sediments," in "Ocean Seismo-Acoustics: Low Frequency Underwater Acoustics," T. Akal and J. M. Berkson, eds., Plenum (1986), p. 435-444; R. D. Stoll, "Acoustic Waves in Saturated Sediments," in "Physics of Sound in Marine Sediments," L. Hampton, ed., Plenum (1974), p. 19-39.

[17]C. T. Tindle, H. Hobaek, and T. G. Muir, "Downslope propagation of normal modes in a shallow water wedge," J. Acoust. Soc. Am. 81, 275-286 (1987a).

[18]R. Heitmeyer and R. Hamson, "Range-depth Ambiguity Surfaces for Vertical Arrays in Shallow-water Environments," J. Acoust. Soc. Am. 81, S64 (1987).

FIGURE CAPTIONS

Fig. 1. Relative density, D_r = density of bottom/density of water, versus relative velocity, c_r = velocity in water/velocity in bottom. Upper straight line fit to data sands and silts without clays, lower straight line fit to data for clays with sands and silts. Squares: data from Hamilton;[15] triangle: data from Tindle et al.;[17,7] circles: cases studied below.

Fig. 2. Percentage nonorthogonality versus scaled depth α for a sand bottom with c_r = 0.847, D_r = 1.96. Vertical dotted lines mark the onset of each new mode. Solid line for a dense array and symbols for a discrete 25-phone array. ⊕ percent nonorthogonality between modes 2 and 1, ⊕ between 3 and 1, □ between 3 and 2, ■ between 4 and 1, □ between 4 and 2, ○ between 4 and 3, △ between 5 and 1, + between 5 and 2, × between 5 and 3, ◇ between 5 and 4, ▽ between 6 and 1, ⊠ between 6 and 2, ✳ between 6 and 3, ○ between 6 and 4, and ● between 6 and 5.

Fig. 3. Same as Fig. 2 for a sand and silt with c_r = 0.909 and D_r = 1.79.

Fig. 4. Same as Fig. 2 for a sand and silt with c_r = 0.926 and D_r = 1.75.

Fig. 5. Same as Fig. 2 for a clay-silt-sand with c_r = 0.990 and D_r = 1.4608.

Fig. 6. Percentage nonorthogonality versus alternate scaled depth γ. Circle for sandy bottom with c_r = 0.847, triangle for c_r = 0.909, plus

for c_r = 0.926, and square for c_r = 0.990. Vertical dotted lines mark the onset of each new mode. Mode numbers may be identified by comparison to Figs. 2 thru 5.

Fig. 7. Percentage nonorthogonality versus fraction of scaled depth α for sandy bottom with c_r = 0.847, α = 26.6 (5 modes present), and the array growing outward from the middle of the water column.

Fig. 8. Same as Fig. 7 for c_r = 0.990 and α = 110 (5 modes present).

Fig. 9. Same as Fig. 7 for the array growing from the top down.

Fig. 10. Same as Fig. 8 for the array growing from the top down.

Fig. 11. Same as Fig. 7 for the array growing from the bottom up.

Fig. 12. Same as Fig. 8 for the array growing from the bottom up.

Fig. 13. Percentage nonorthogonality versus scaled depth α for a sandy bottom with c_r = 0.847 with an array which spans the middle half of the water column.

Fig. 14. Same as Fig. 13 for c_r = 0.990.

Fig. 15. Same as Fig. 13 for the array spanning the top half of the water column.

Fig. 16. Same as Fig. 14 for the array spanning the top half of the water column.

Fig. 17. Same as Fig. 13 for the array spanning the bottom half of the water column.

Fig. 18. Same as Fig. 14 for the array spanning the bottom half of the water column.

Fig. 19. Percentage nonorthogonality versus scaled depth α for a sandy bottom with $c_r = 0.847$ for a fixed length array centered on the middle of the water column. The dimensionless array length is chosen to span half the water column at the onset of the second mode.

Fig. 20. Same as Fig. 19 for $c_r = 0.990$.

Fig. 21. Same as Fig. 19 with the fixed length array having its upper end at the top of the water column.

Fig. 22. Same as Fig. 20 with the fixed length array having its upper end at the top of the water column.

Fig. 23. Same as Fig. 19 with the fixed length array having its lower end at the bottom of the water column.

Fig. 24. Same as Fig. 20 with the fixed length array havings its lower end at the bottom of the water column.

Fig. 25. Same as Fig. 2 except that the symbols are for a 12-phone array.

Fig. 26. Same as Fig. 2 except that the symbols are for a 6-phone array.

Fig. 1

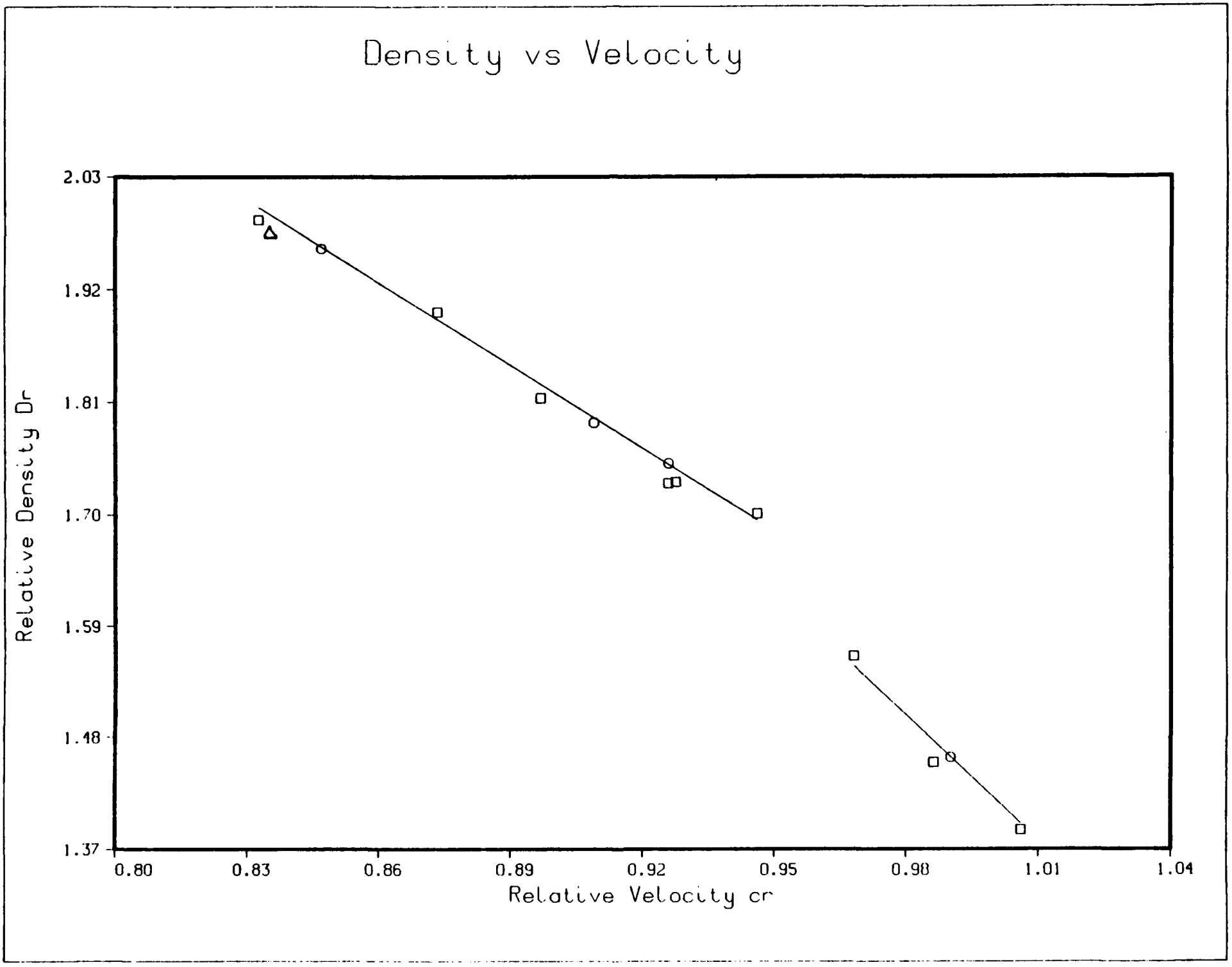
Density vs Velocity
Relative Density Dr
2.03
1.92
1.81
1.70
1.59
1.48
1.37
0.80
0.83
0.86
0.89
0.92
0.95
0.98
1.01
1.04
Relative Velocity cr

Fig. 2

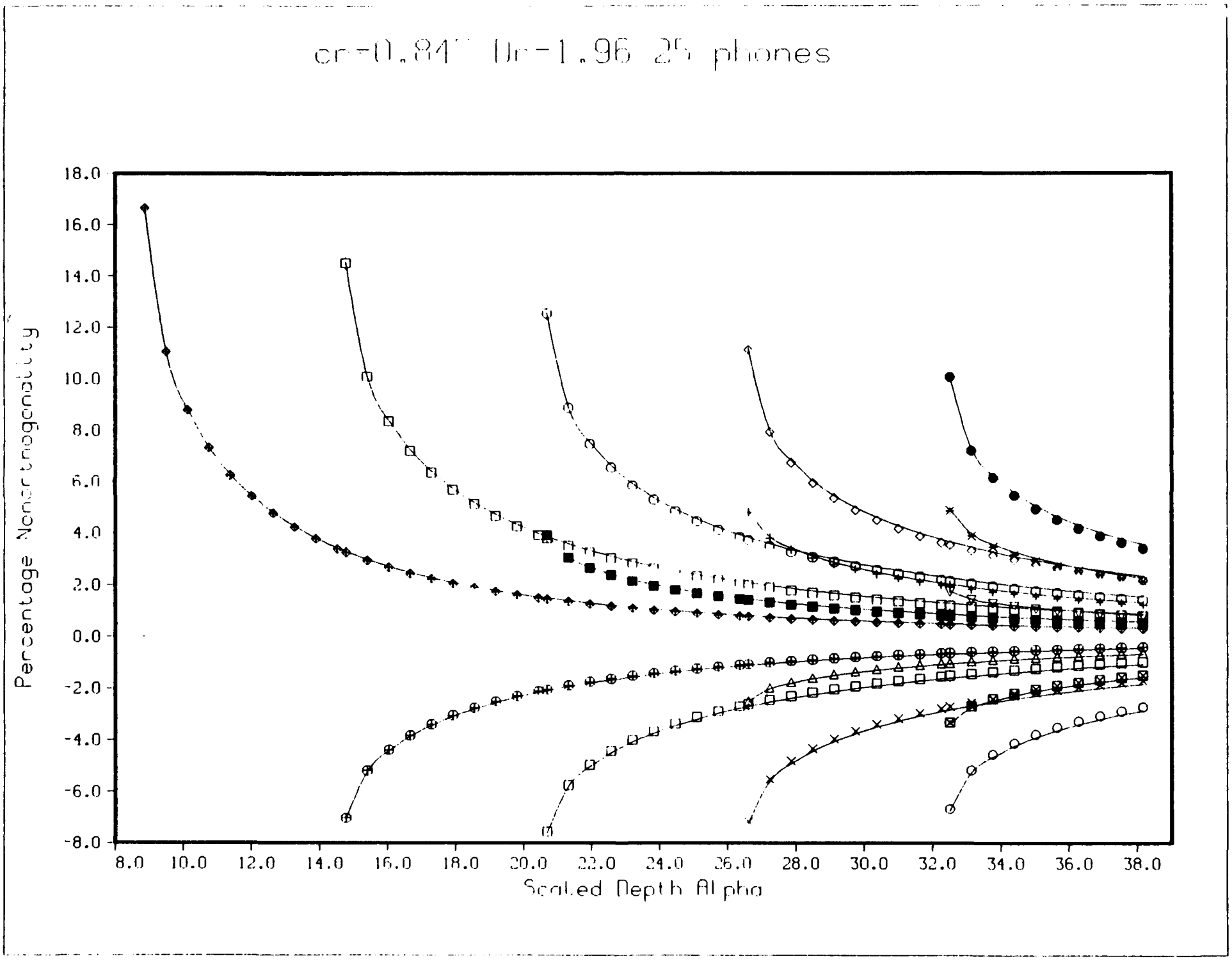
cr=0.84 Ur=1.96 25 phones
Percentage Nonentnogenability
18.0
16.0
14.0
12.0
10.0
8.0
6.0
4.0
2.0
0.0
-2.0
-4.0
-6.0
-8.0
8.0
10.0
12.0
14.0
16.0
18.0
20.0
22.0
24.0
26.0
28.0
30.0
32.0
34.0
36.0
38.0
Scaled Depth Alpha

Fig. 3

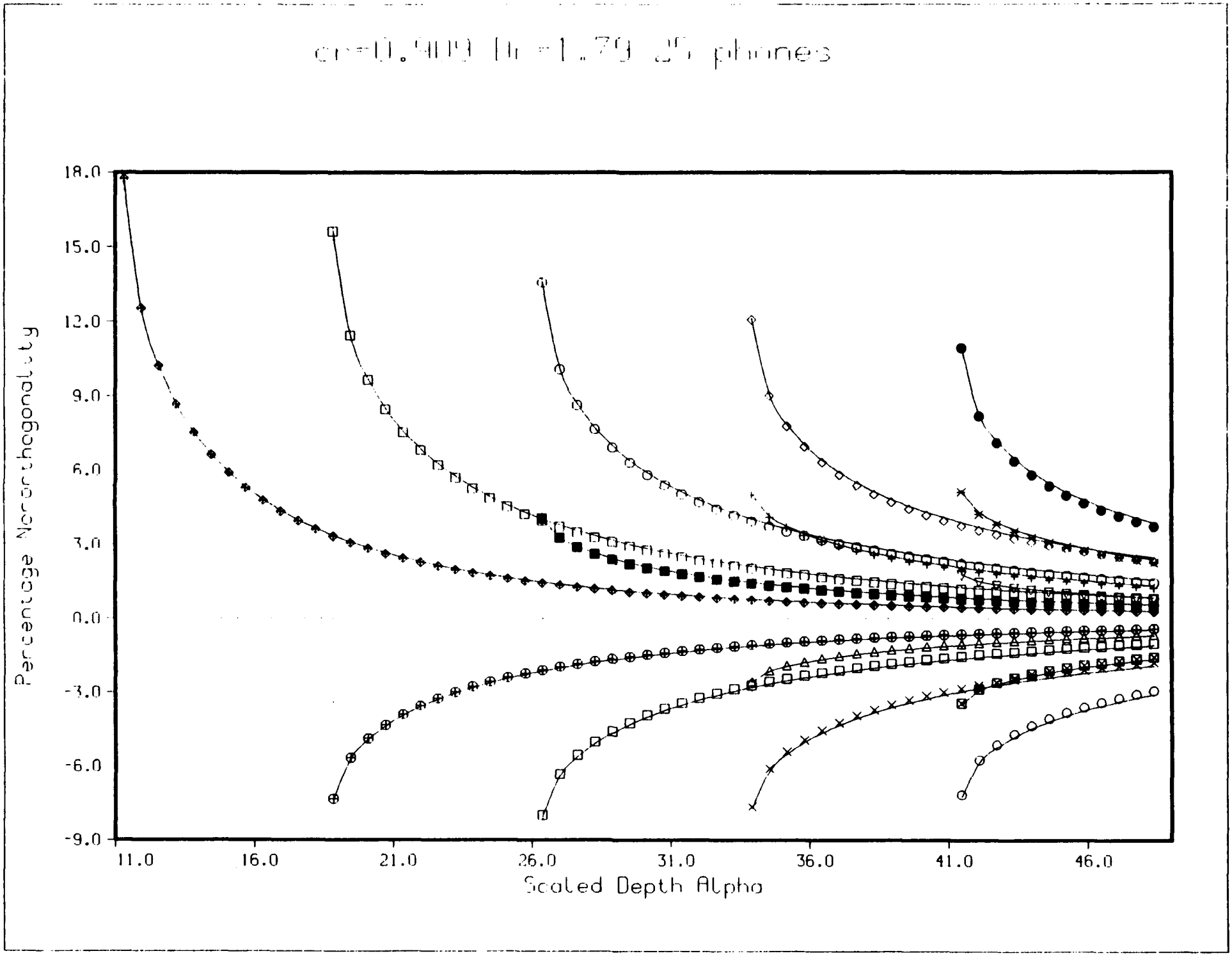
cr=0.489 h=1.79 25 planes
18.0
15.0
12.0
9.0
6.0
3.0
0.0
-3.0
-6.0
-9.0
Percentage Nonorthogonality
11.0
16.0
21.0
26.0
31.0
36.0
41.0
46.0
Scaled Depth Alpha

Fig. 4

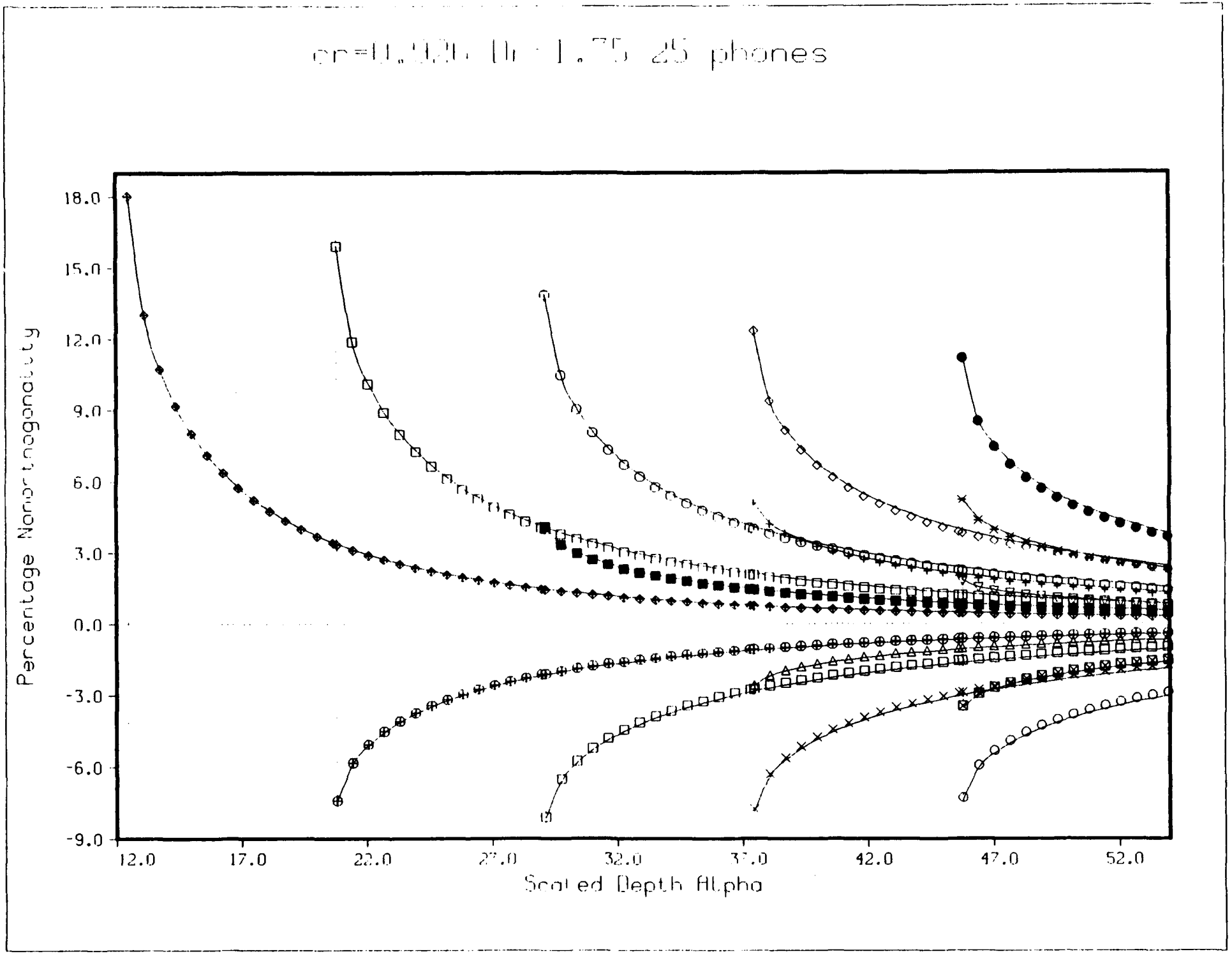
cr=0.020 th=1.75 25 phones
18.0
15.0
12.0
9.0
6.0
3.0
0.0
-3.0
-6.0
-9.0
Percentage Nonorthogonality
12.0
17.0
22.0
27.0
32.0
37.0
42.0
47.0
52.0
Scaled Depth Alpha

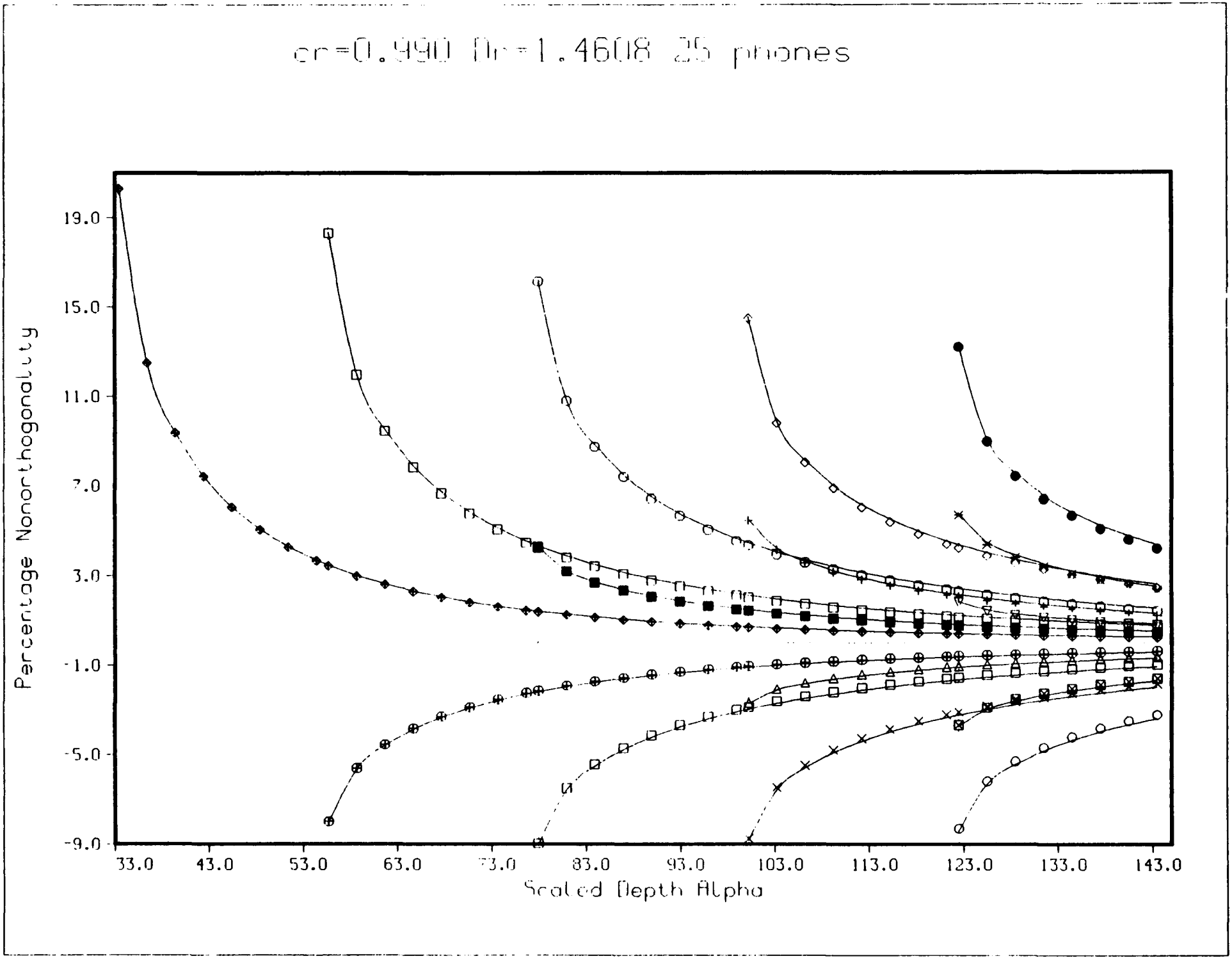
cr=0.990 Rr=1.4608 25 phones
19.0
15.0
11.0
7.0
3.0
-1.0
-5.0
-9.0
Percentage Nonorthogonality
33.0
43.0
53.0
63.0
73.0
83.0
93.0
103.0
113.0
123.0
133.0
143.0
Scaled Depth Alpha

Fig. 6

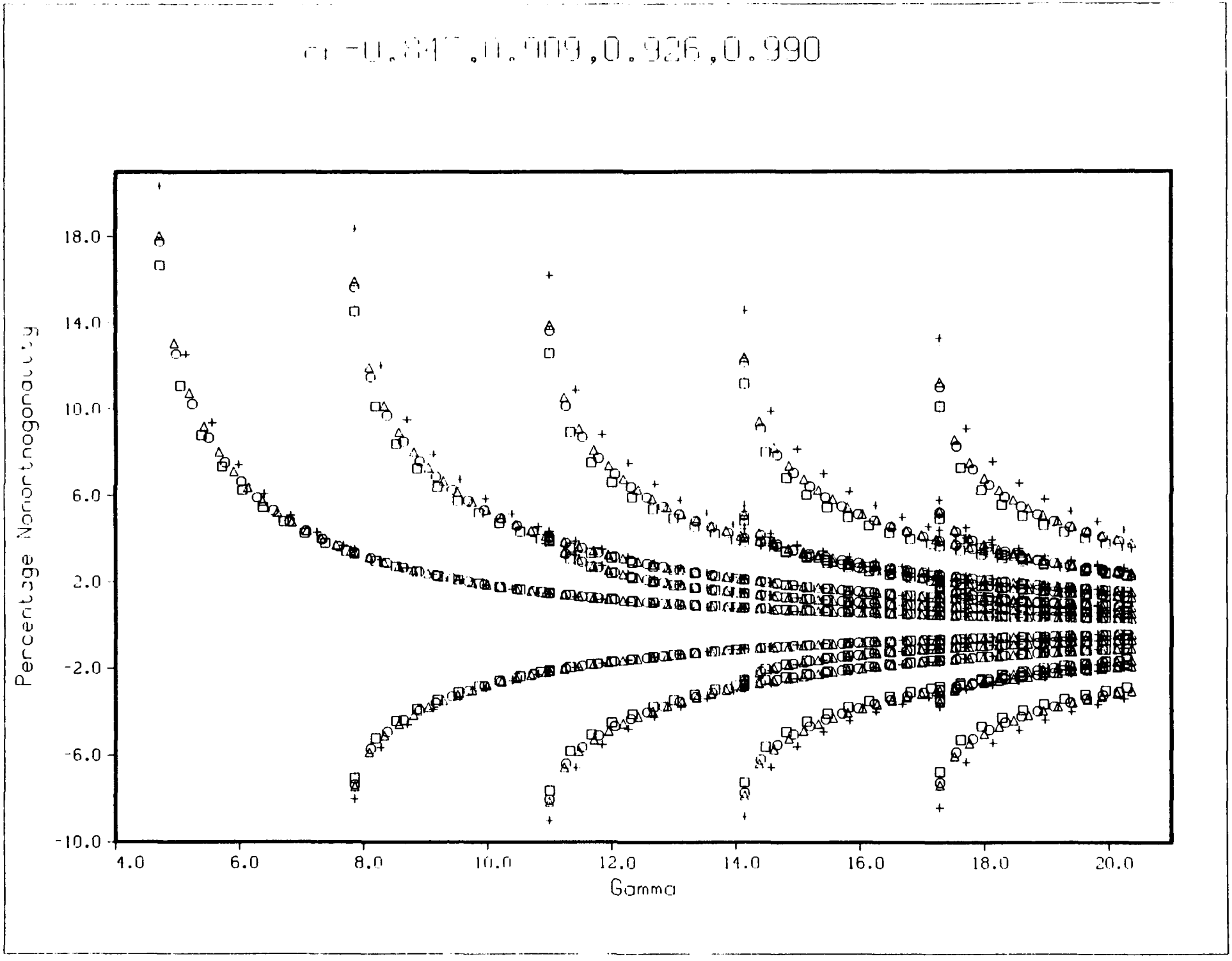
Percentage Nonorthogonality
18.0
14.0
10.0
6.0
2.0
-2.0
-6.0
-10.0
4.0
6.0
8.0
10.0
12.0
14.0
16.0
18.0
20.0
Gamma

Fig. 7

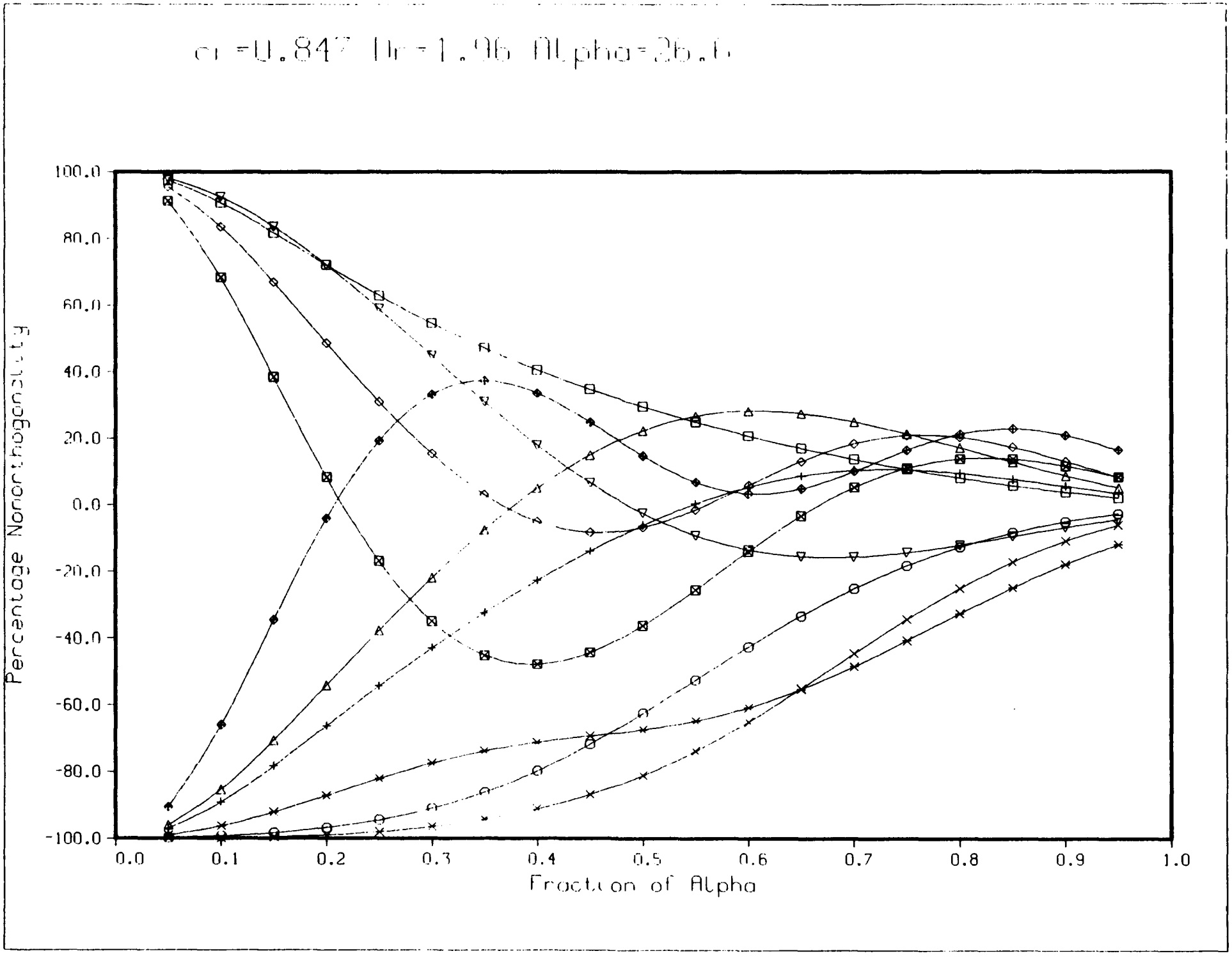
Cr=0.847 Hr=1.96 Alpha=26.6
100.0
80.0
60.0
40.0
20.0
0.0
-20.0
-40.0
-60.0
-80.0
-100.0
Percentage Nonorthogonality
0.0
0.1
0.2
0.3
0.4
0.5
0.6
0.7
0.8
0.9
1.0
Fraction of Alpha

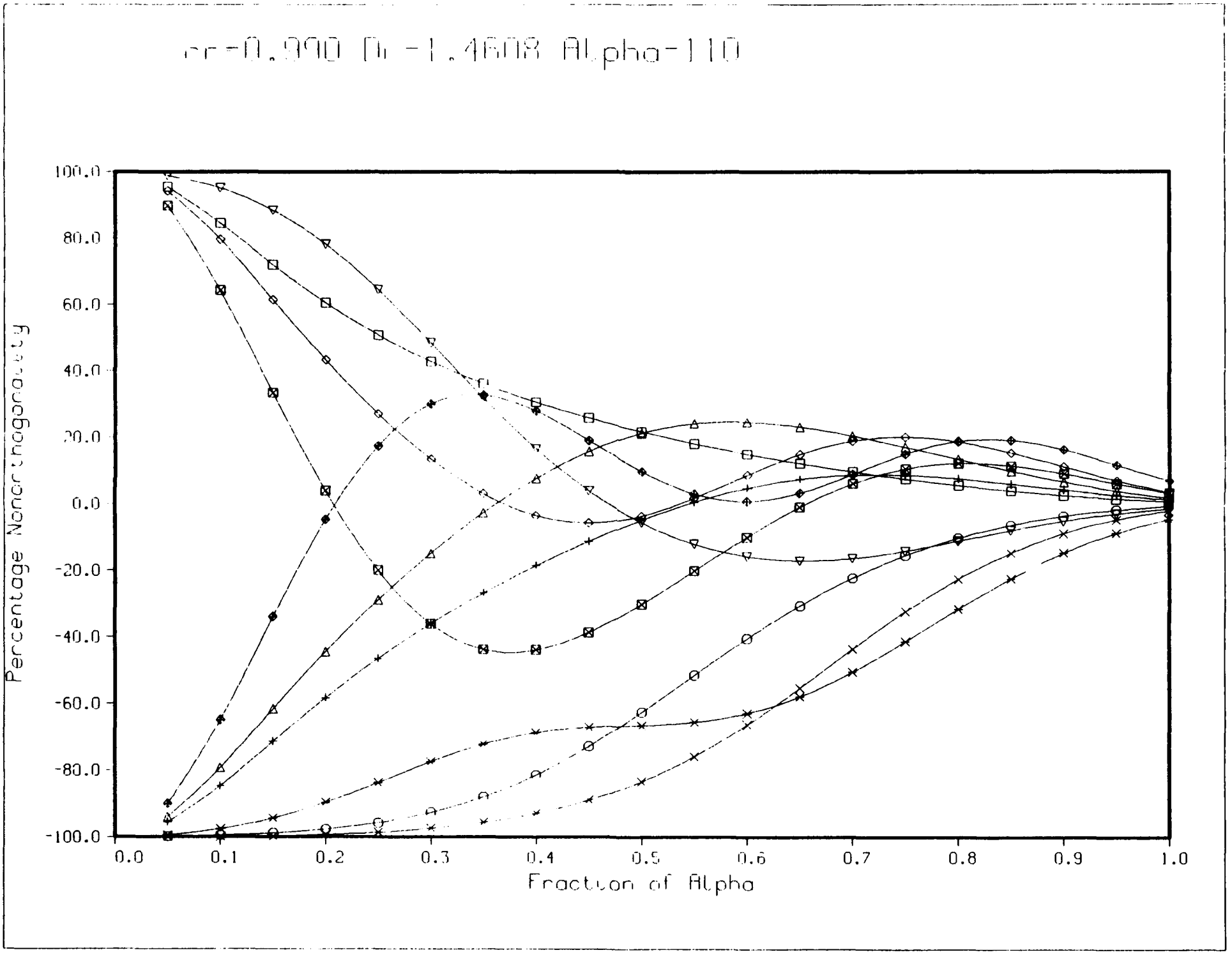
rr=0.990 n=1.4608 Alpha=110
Percentage Noncentrality
100.0
80.0
60.0
40.0
20.0
0.0
-20.0
-40.0
-60.0
-80.0
-100.0
0.0
0.1
0.2
0.3
0.4
0.5
0.6
0.7
0.8
0.9
1.0
Fraction of Alpha

Fig. 9

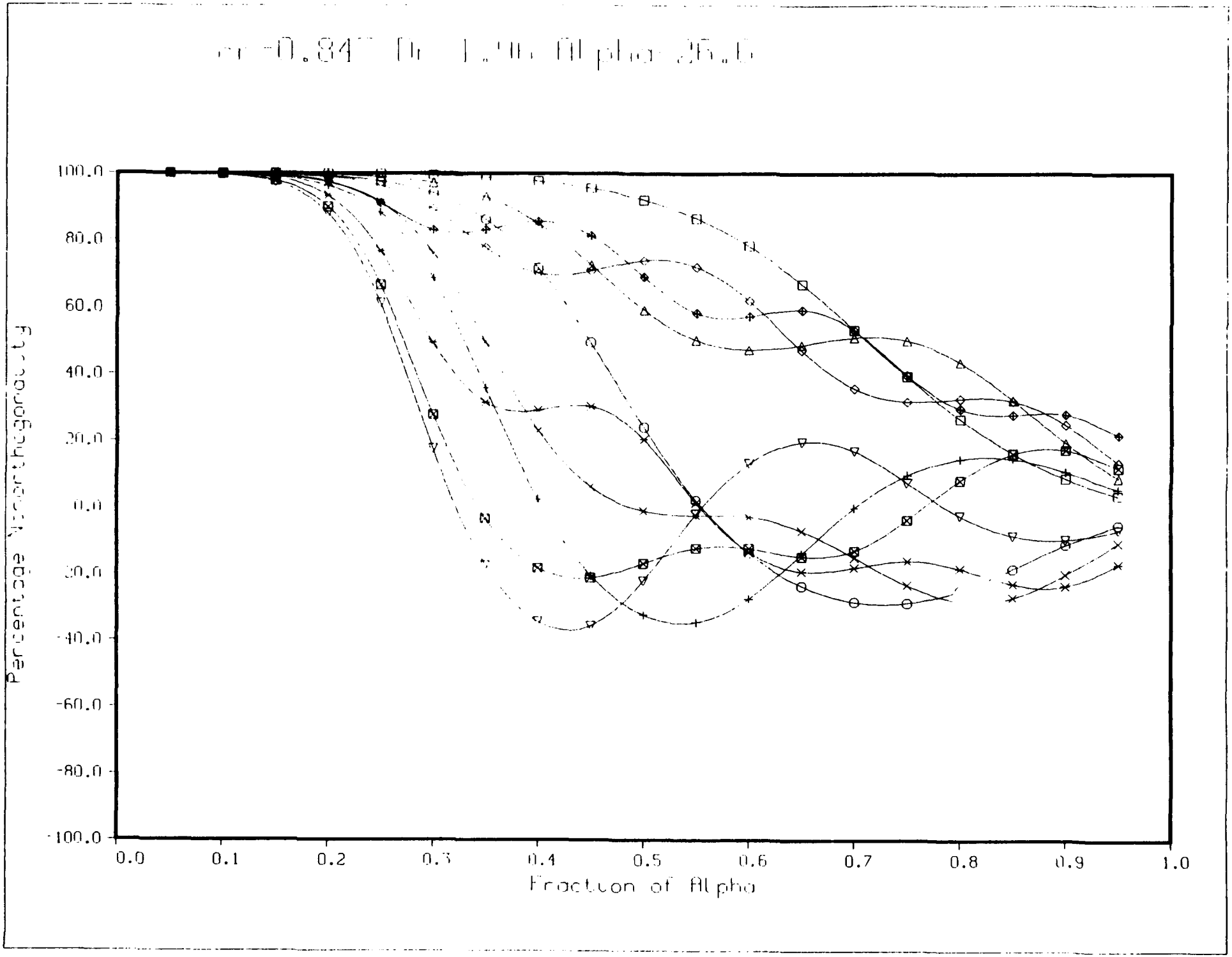
100.0
80.0
60.0
40.0
20.0
0.0
-20.0
-40.0
-60.0
-80.0
-100.0
0.0
0.1
0.2
0.3
0.4
0.5
0.6
0.7
0.8
0.9
1.0
Fraction of Alpha

Fig. 10

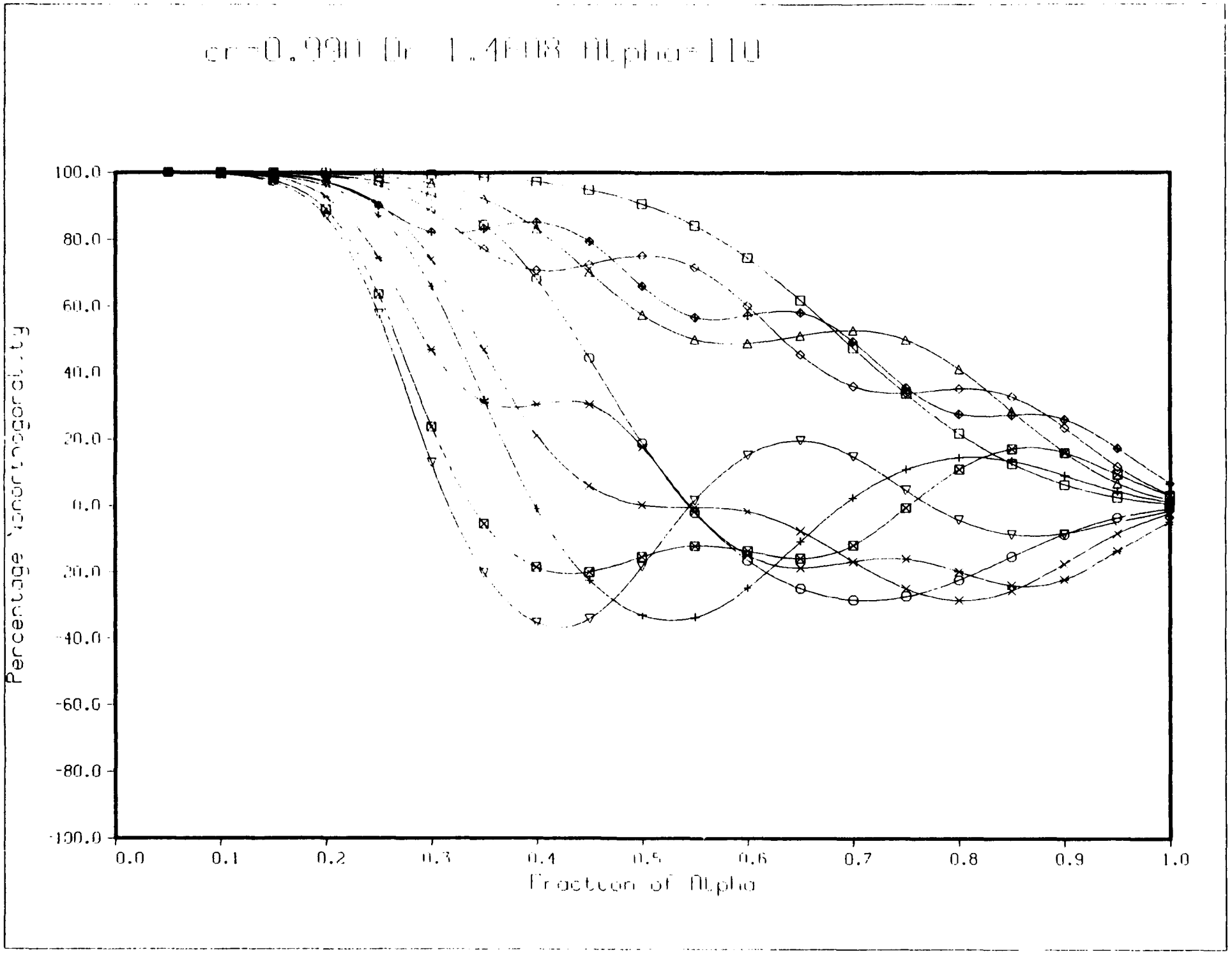
100.0
80.0
60.0
40.0
20.0
0.0
-20.0
-40.0
-60.0
-80.0
-100.0
0.0
0.1
0.2
0.3
0.4
0.5
0.6
0.7
0.8
0.9
1.0
Fraction of Alpha

Fig. 11

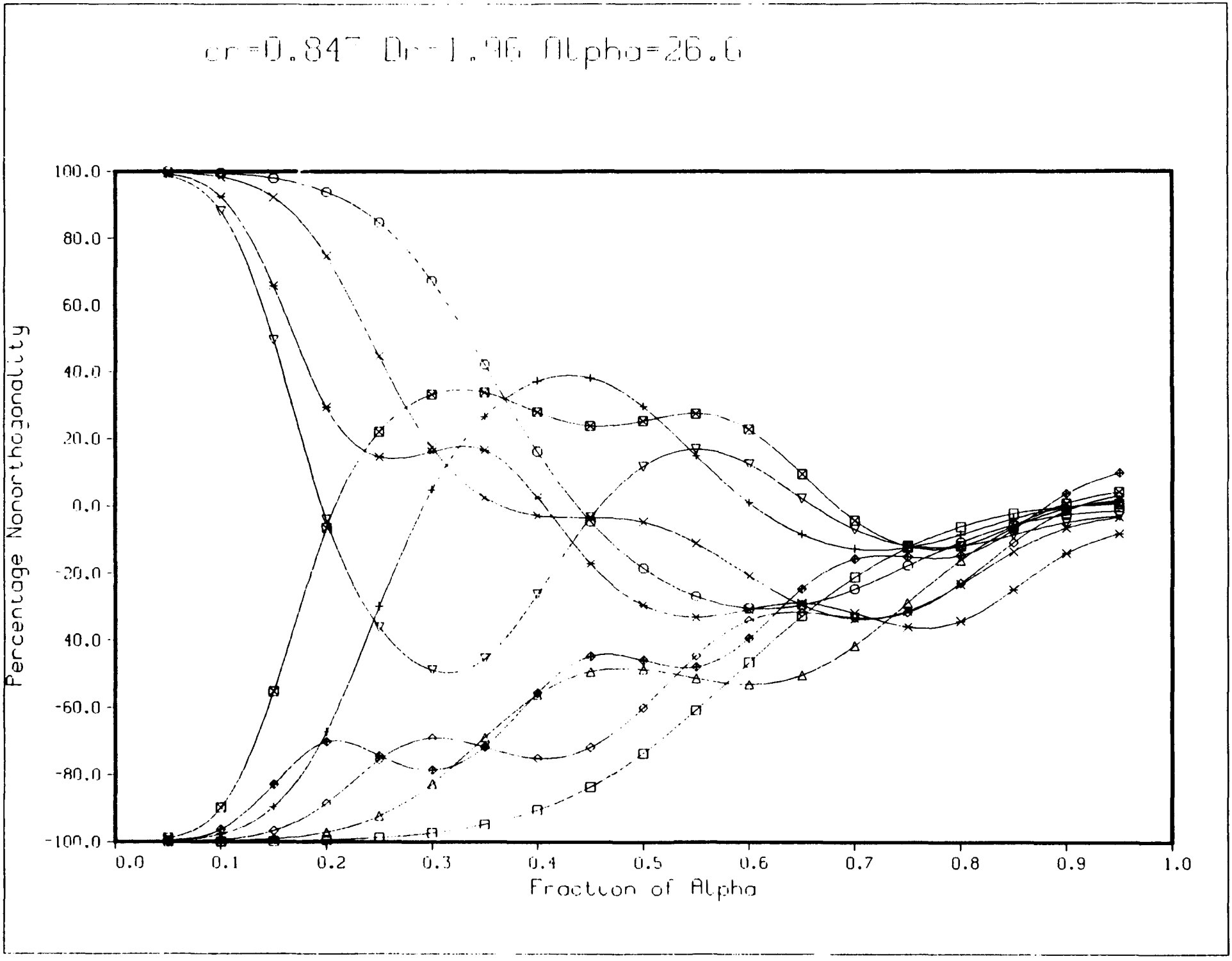
cr=0.847 Dr=1.96 Alpha=26.6
100.0
80.0
60.0
40.0
20.0
0.0
-20.0
-40.0
-60.0
-80.0
-100.0
Percentage Nonorthogonality
0.0
0.1
0.2
0.3
0.4
0.5
0.6
0.7
0.8
0.9
1.0
Fraction of Alpha

Fig. 12

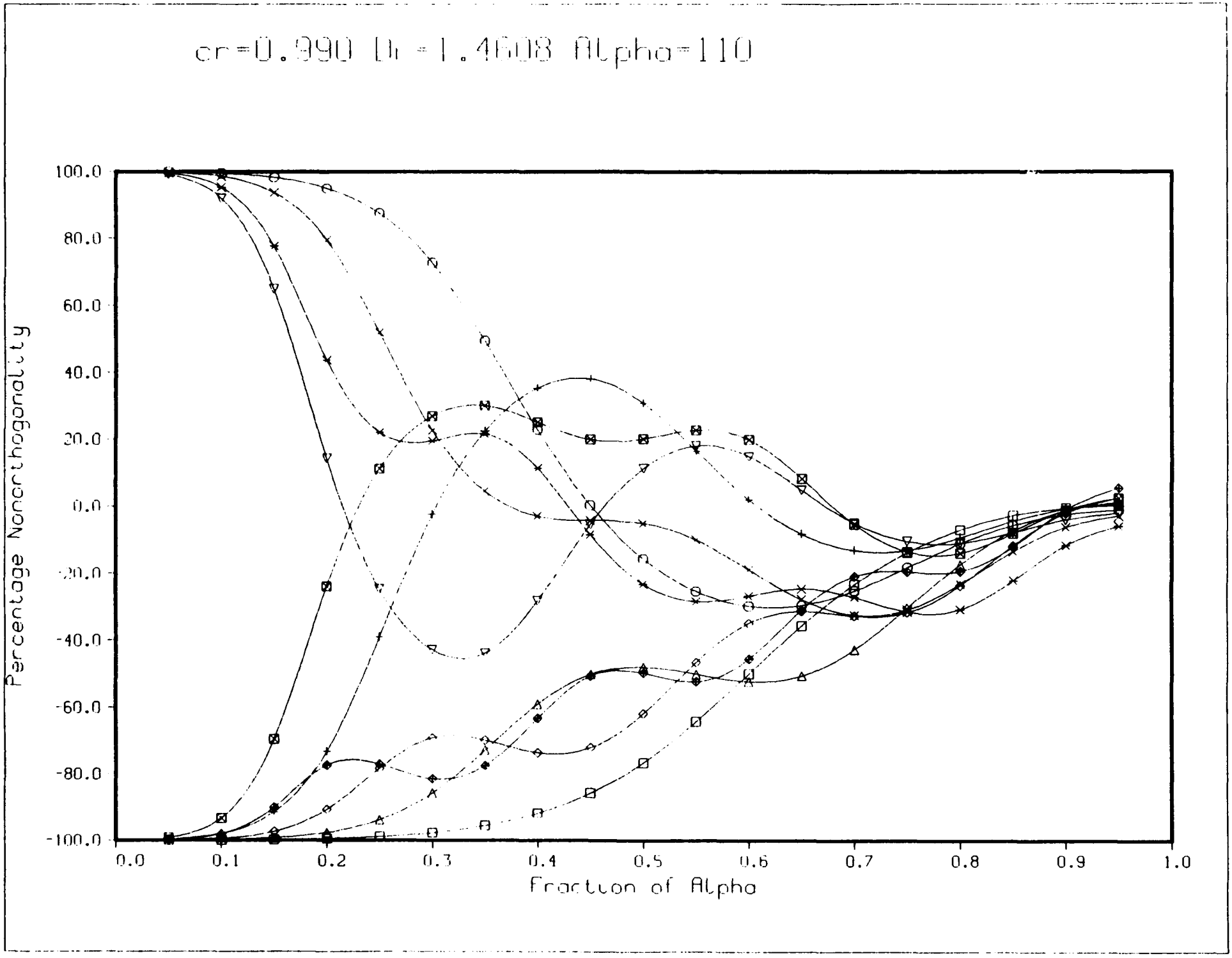
cr=0.990 h=1.4608 Alpha=110
Percentage Nonorthogonality
100.0
80.0
60.0
40.0
20.0
0.0
-20.0
-40.0
-60.0
-80.0
-100.0
0.0
0.1
0.2
0.3
0.4
0.5
0.6
0.7
0.8
0.9
1.0
Fraction of Alpha

Fig. 13

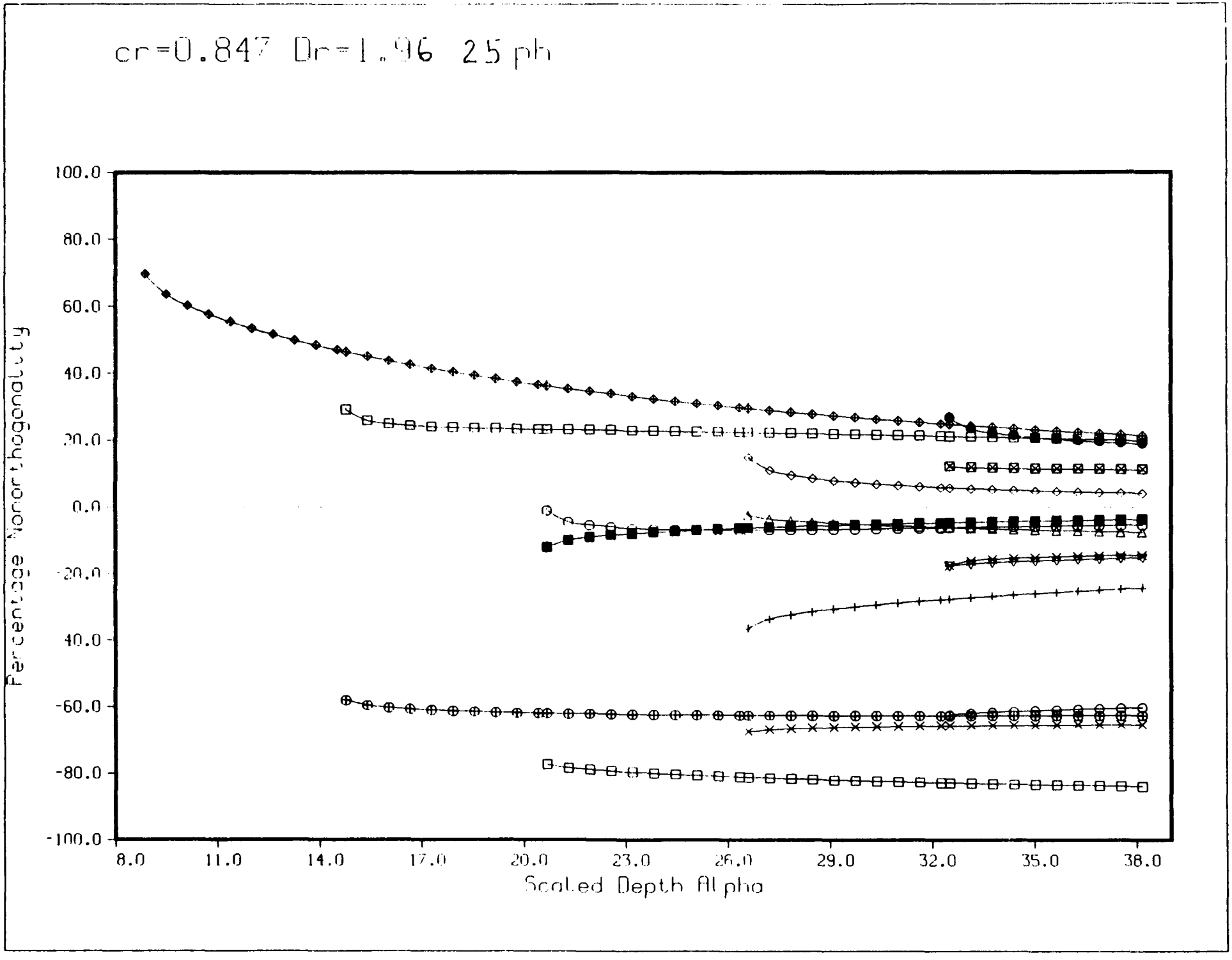
cr=0.847 Dr=1.96 25 ph
100.0
80.0
60.0
40.0
20.0
0.0
-20.0
-40.0
-60.0
-80.0
-100.0
Percentage Nonorthogonality
8.0
11.0
14.0
17.0
20.0
23.0
26.0
29.0
32.0
35.0
38.0
Scaled Depth Alpha

Fig. 14

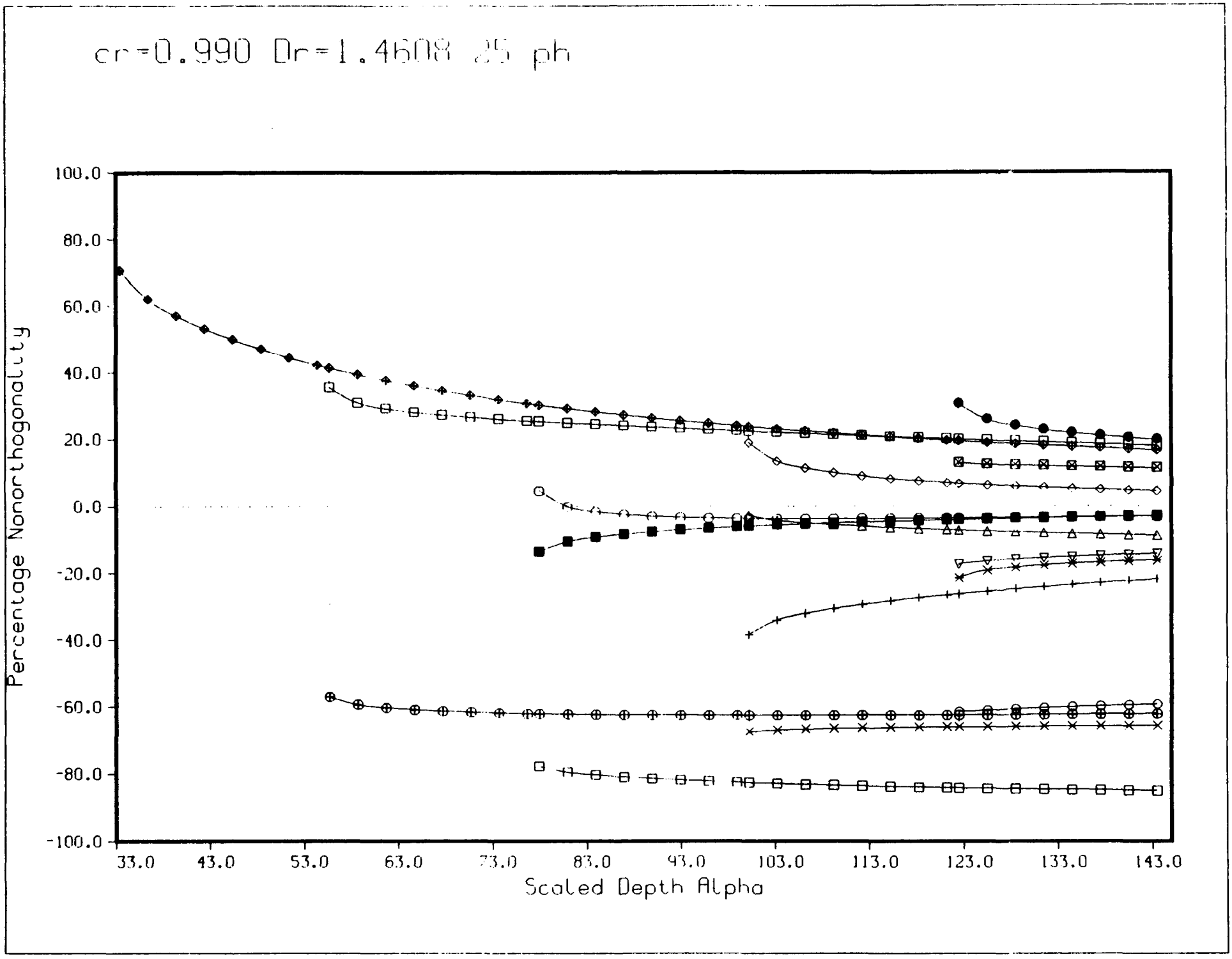
cr=0.990 Dr=1.4608 25 ph
100.0
80.0
60.0
40.0
20.0
0.0
-20.0
-40.0
-60.0
-80.0
-100.0
Percentage Nonorthogonality
33.0
43.0
53.0
63.0
73.0
83.0
93.0
103.0
113.0
123.0
133.0
143.0
Scaled Depth Alpha

Fig. 15

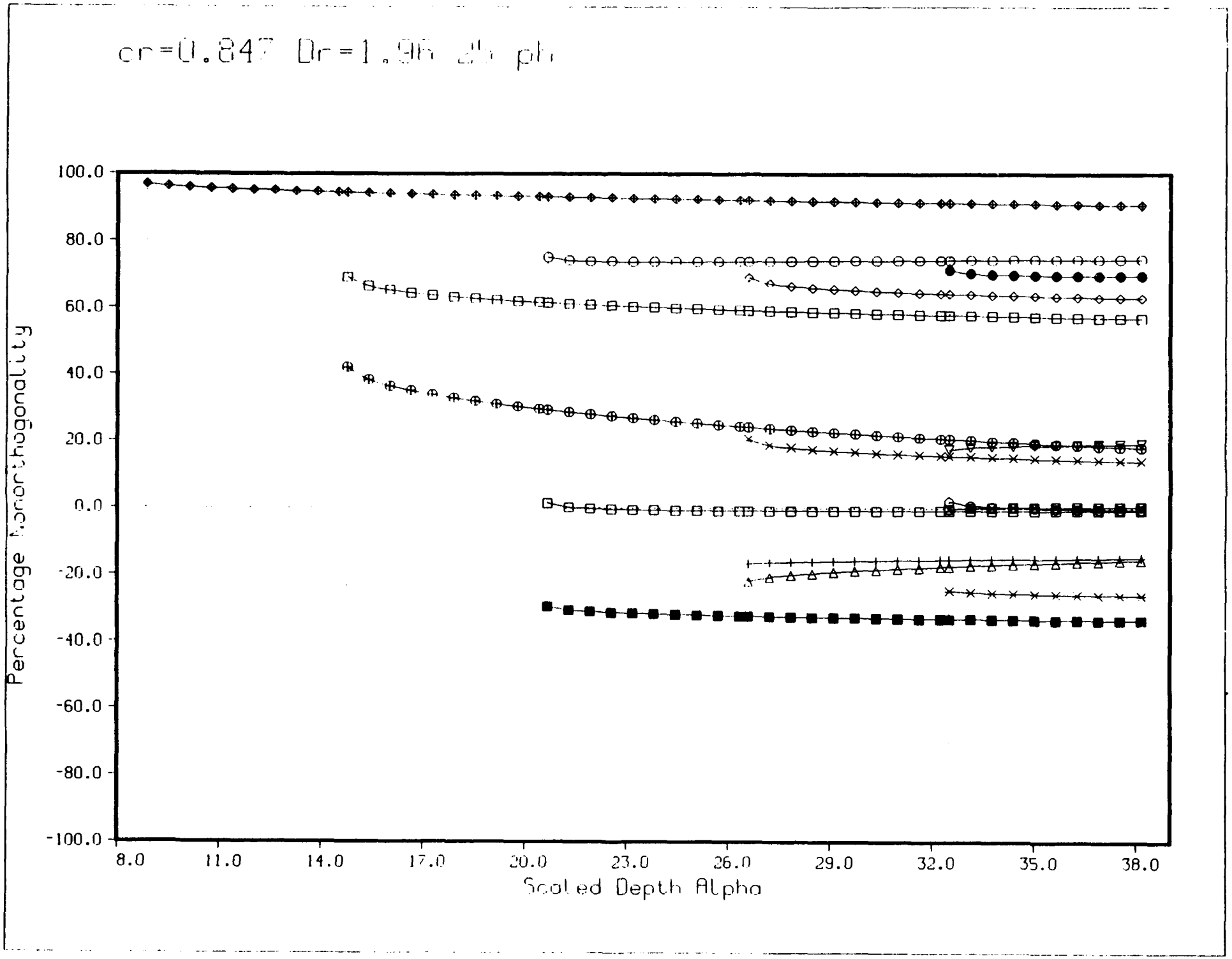
100.0
80.0
60.0
40.0
20.0
0.0
-20.0
-40.0
-60.0
-80.0
-100.0
Percentage Nonorthogonality
8.0
11.0
14.0
17.0
20.0
23.0
26.0
29.0
32.0
35.0
38.0
Scaled Depth Alpha

Fig. 16

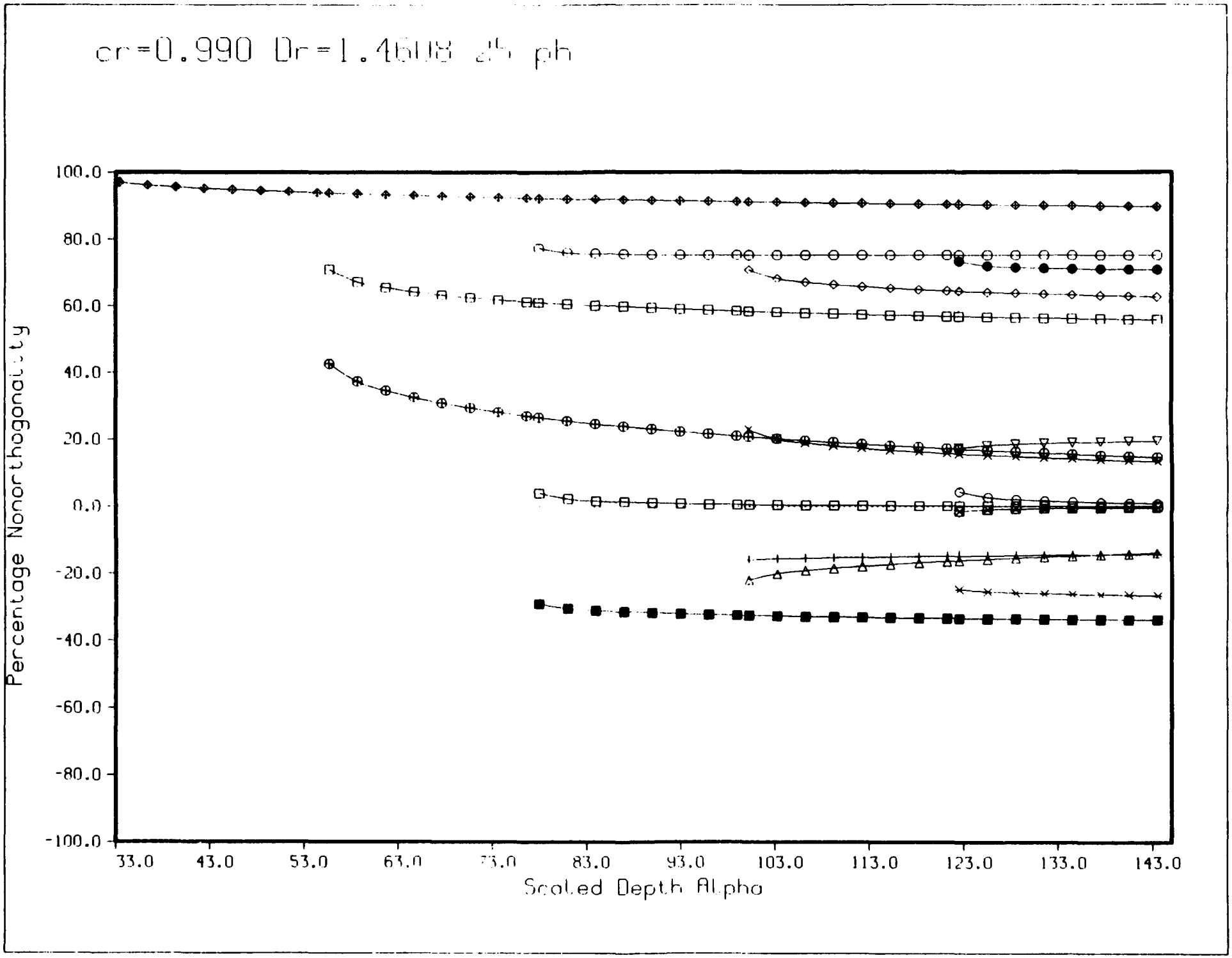
cr=0.990 Dr=1.4608 25 ph
100.0
80.0
60.0
40.0
20.0
0.0
-20.0
-40.0
-60.0
-80.0
-100.0
Percentage Nonorthogonality
33.0
43.0
53.0
63.0
73.0
83.0
93.0
103.0
113.0
123.0
133.0
143.0
Scaled Depth Alpha

Fig. 17

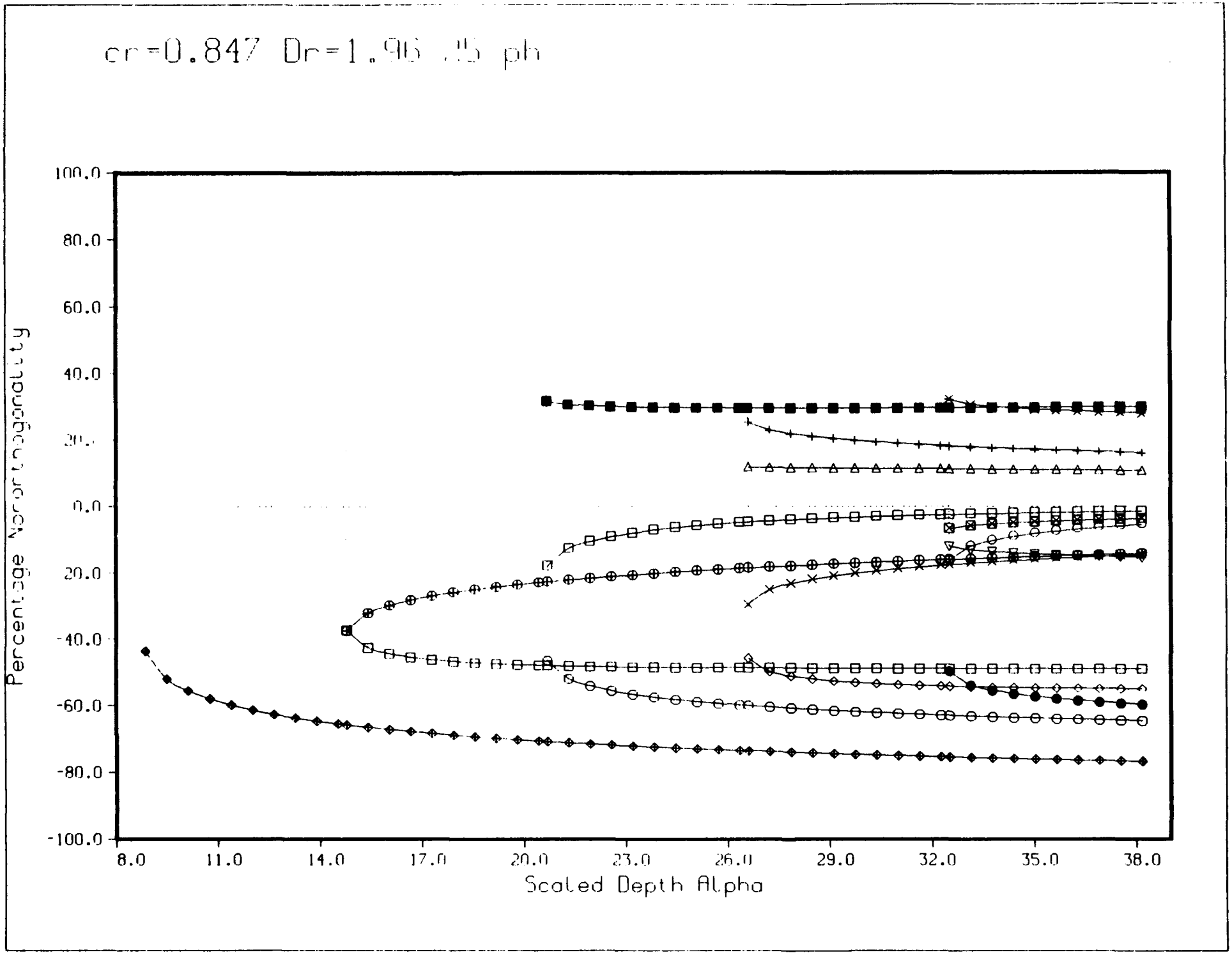
cr=0.847 Dr=1.96 .5 ph
100.0
80.0
60.0
40.0
20.0
0.0
-20.0
-40.0
-60.0
-80.0
-100.0
Percentage Nonentanglability
8.0
11.0
14.0
17.0
20.0
23.0
26.0
29.0
32.0
35.0
38.0
Scaled Depth Alpha

Fig. 18

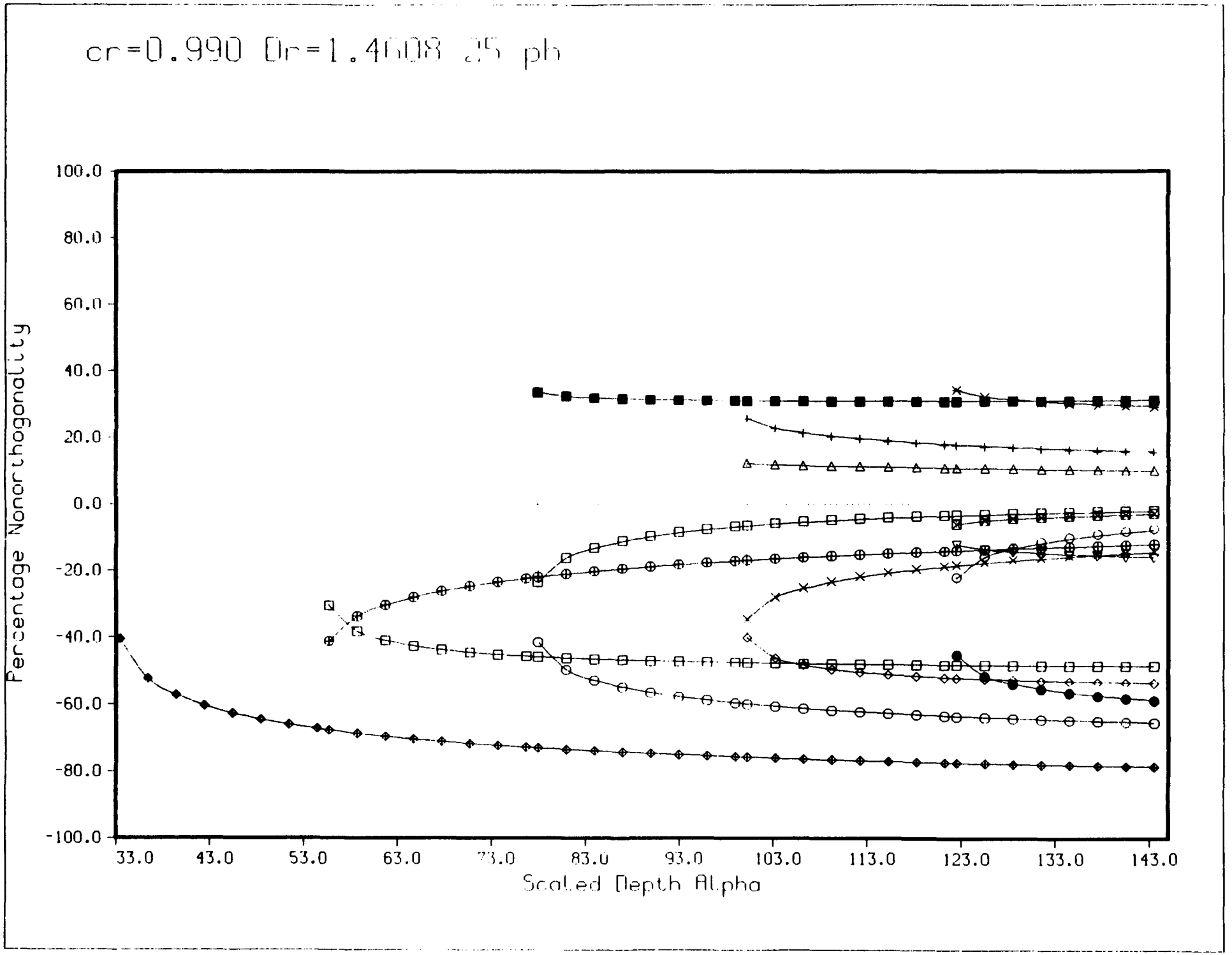
cr=0.990 Dr=1.4608 25 ph
100.0
80.0
60.0
40.0
20.0
0.0
-20.0
-40.0
-60.0
-80.0
-100.0
Percentage Nonorthogonality
33.0
43.0
53.0
63.0
73.0
83.0
93.0
103.0
113.0
123.0
133.0
143.0
Scaled Depth Alpha

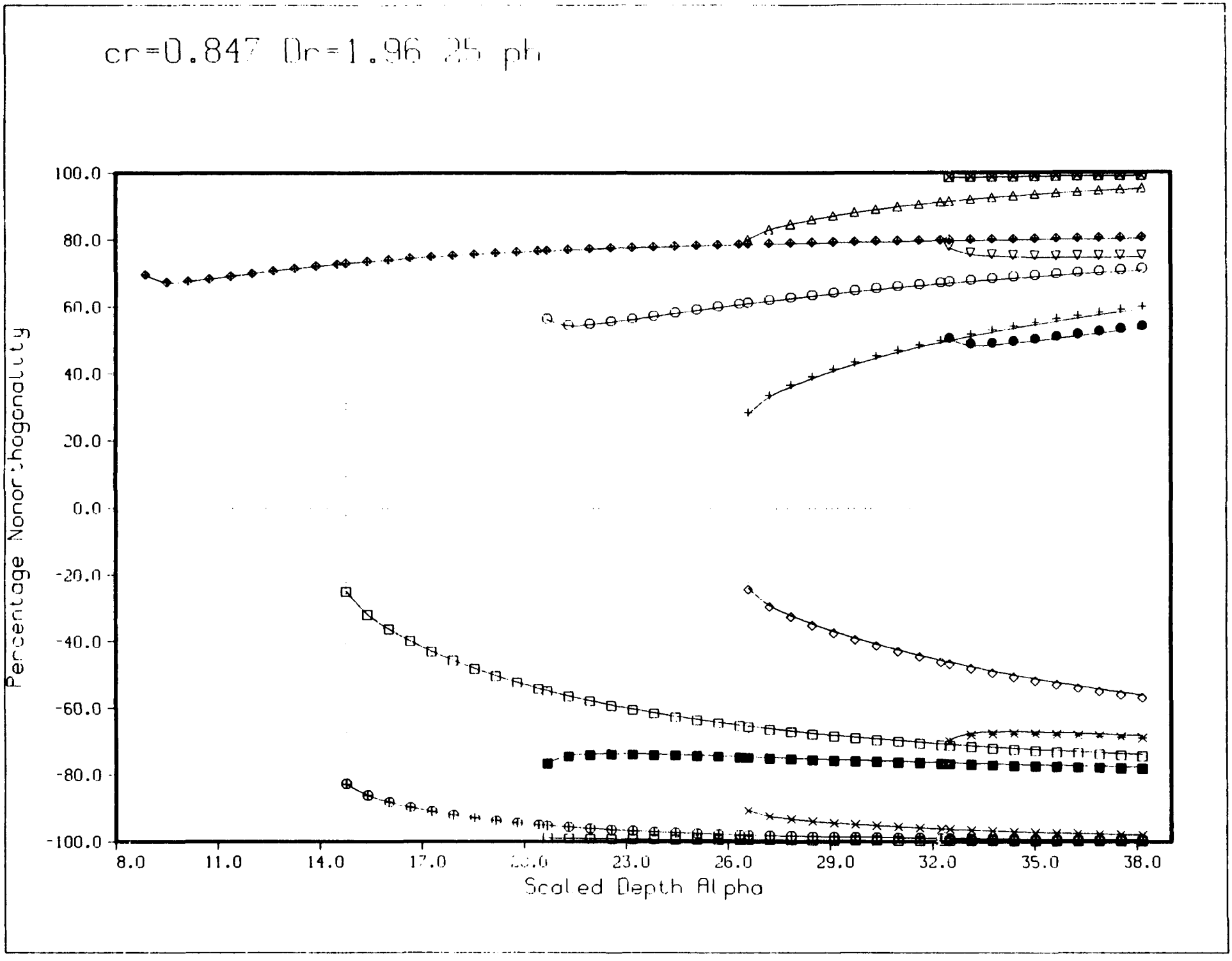
cr=0.847 Dr=1.96 25 ph
Percentage Nonorthogonality
100.0
80.0
60.0
40.0
20.0
0.0
-20.0
-40.0
-60.0
-80.0
-100.0
8.0
11.0
14.0
17.0
23.0
26.0
29.0
32.0
35.0
38.0
Scaled Depth Alpha

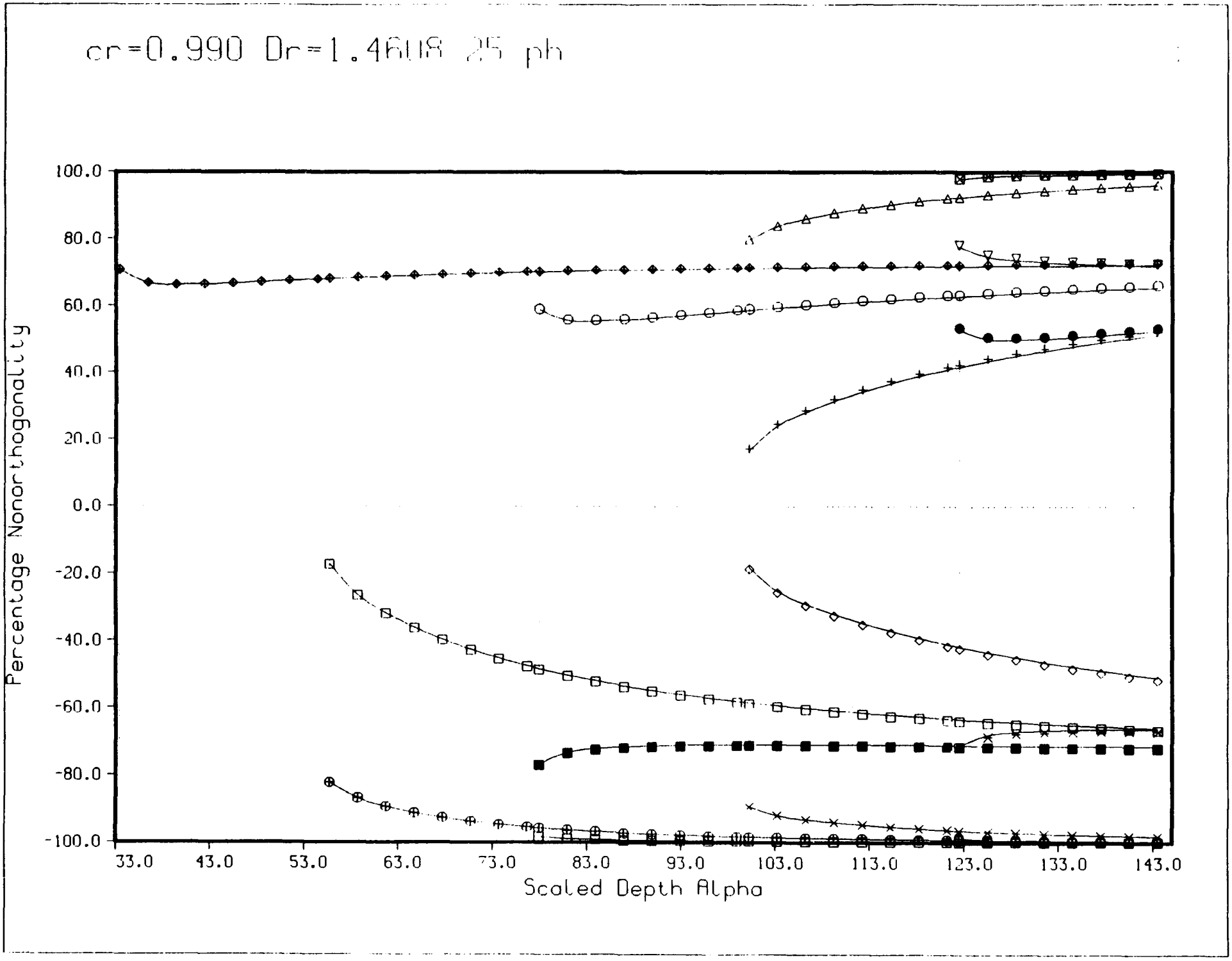
cr=0.990 Dr=1.4618 25 ph
Percentage Nonorthogonality
100.0
80.0
60.0
40.0
20.0
0.0
-20.0
-40.0
-60.0
-80.0
-100.0
33.0
43.0
53.0
63.0
73.0
83.0
93.0
103.0
113.0
123.0
133.0
143.0
Scaled Depth Alpha

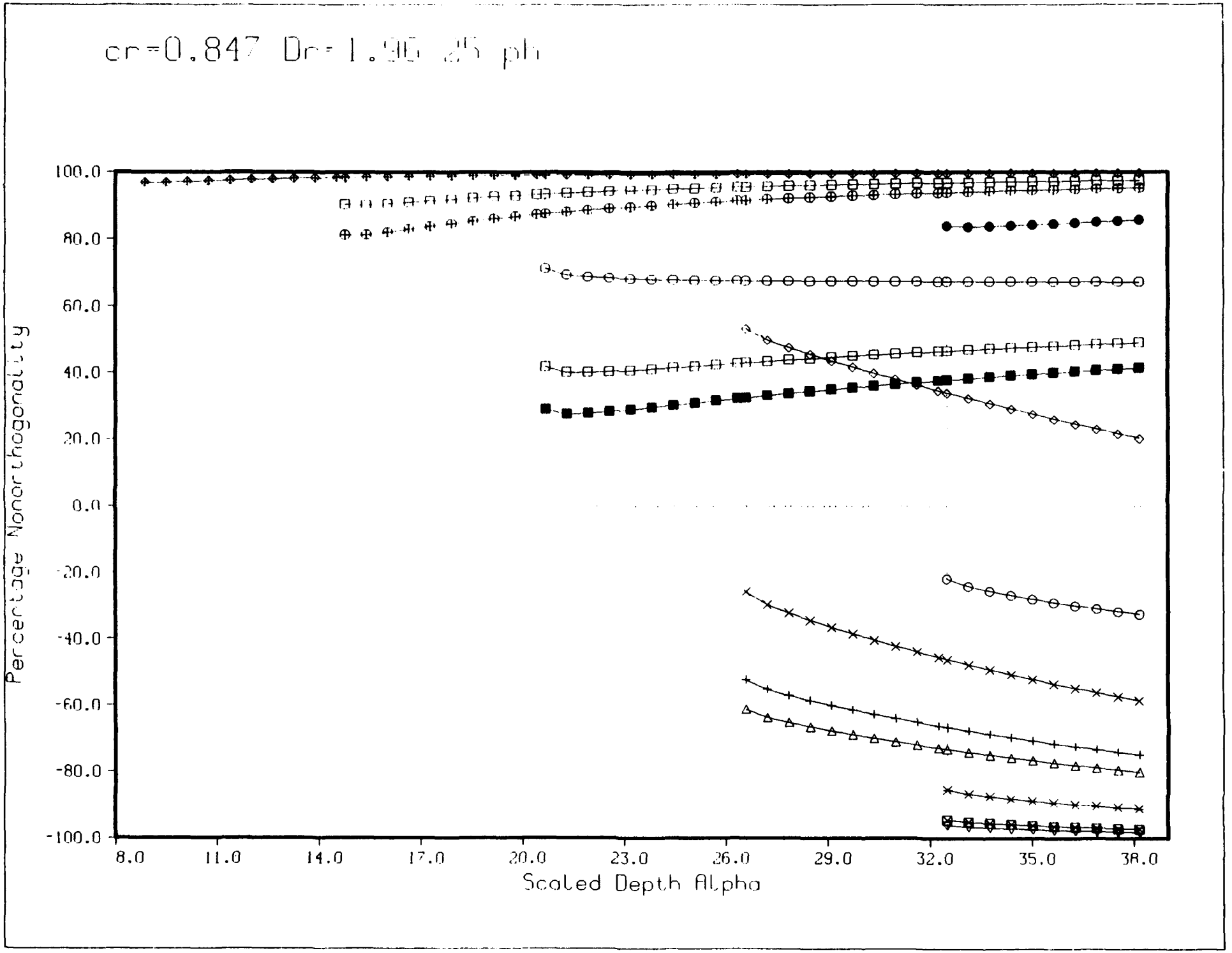
cr=0.847 Dr=1.96 25 ph
100.0
80.0
60.0
40.0
20.0
0.0
-20.0
-40.0
-60.0
-80.0
-100.0
Percentage Nonorthogonality
8.0
11.0
14.0
17.0
20.0
23.0
26.0
29.0
32.0
35.0
38.0
Scaled Depth Alpha

Fig. 22

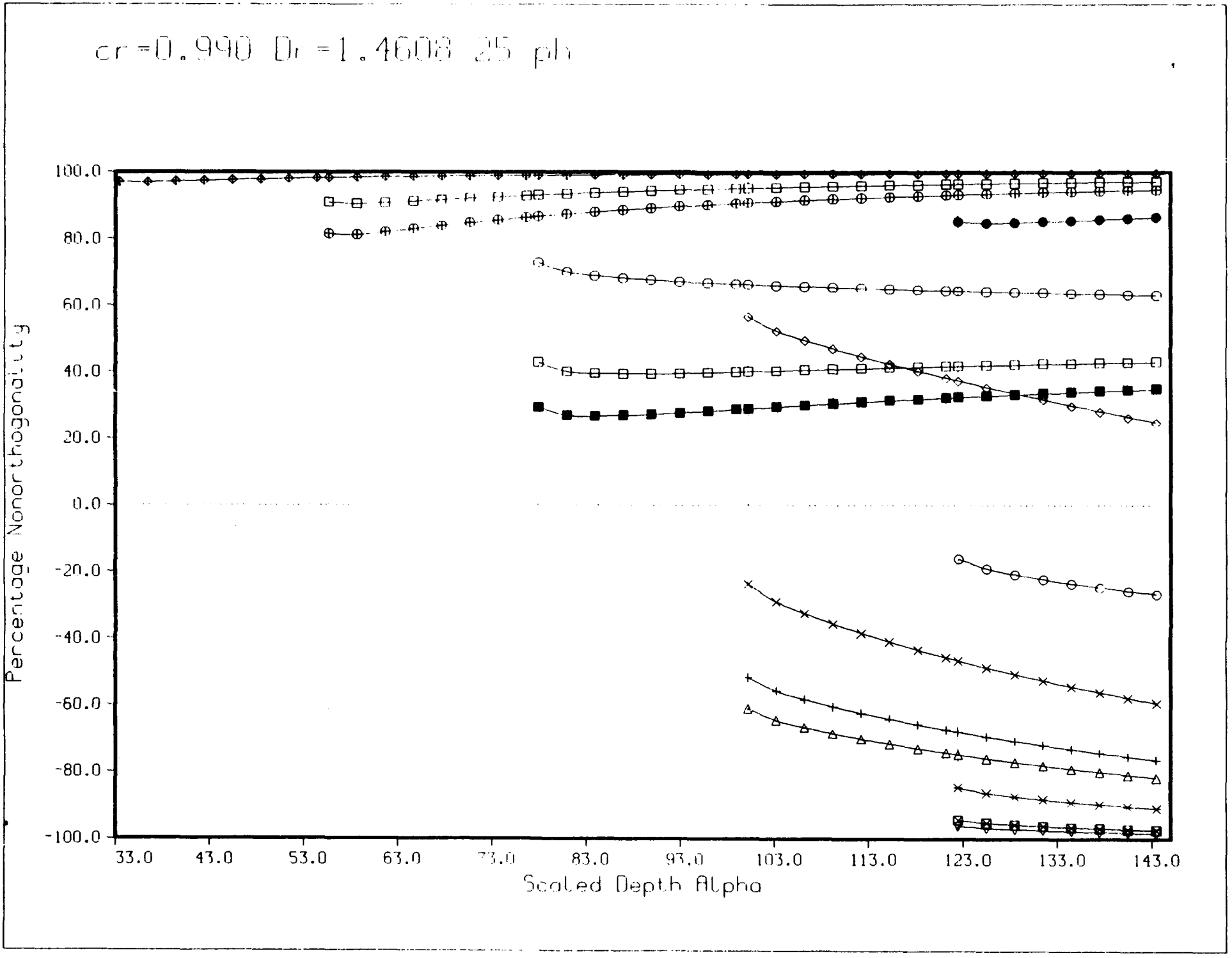
cr=0.990 Dr=1.4608 25 ph
100.0
80.0
60.0
40.0
20.0
0.0
-20.0
-40.0
-60.0
-80.0
-100.0
Percentage Nonorthogonality
33.0
43.0
53.0
63.0
73.0
83.0
93.0
103.0
113.0
123.0
133.0
143.0
Scaled Depth Alpha

Fig. 23

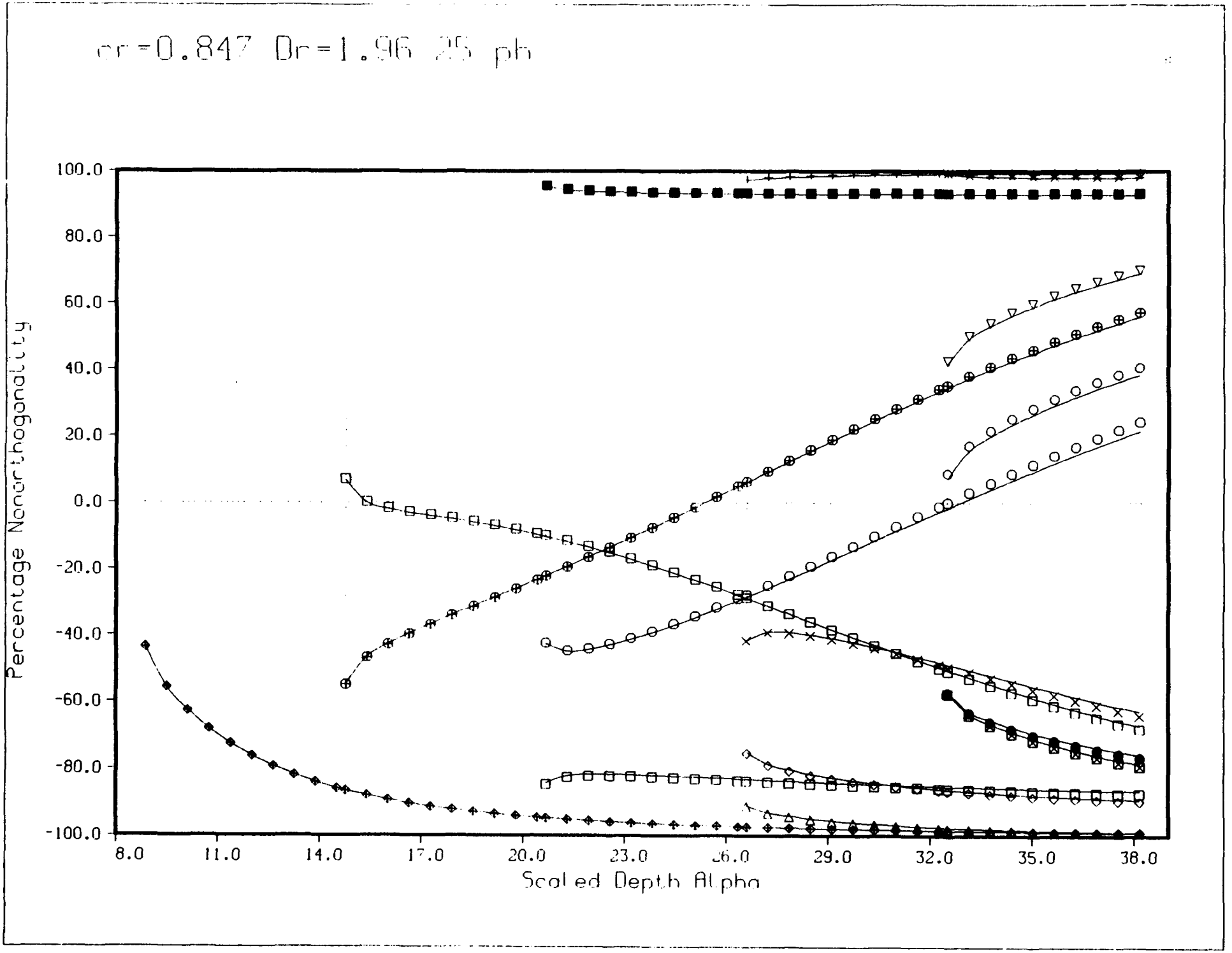
σr=0.847 Dr=1.96 25 ph
100.0
80.0
60.0
40.0
20.0
0.0
-20.0
-40.0
-60.0
-80.0
-100.0
Percentage Nonorthogonality
8.0
11.0
14.0
17.0
20.0
23.0
26.0
29.0
32.0
35.0
38.0
Scaled Depth Alpha

Fig. 24

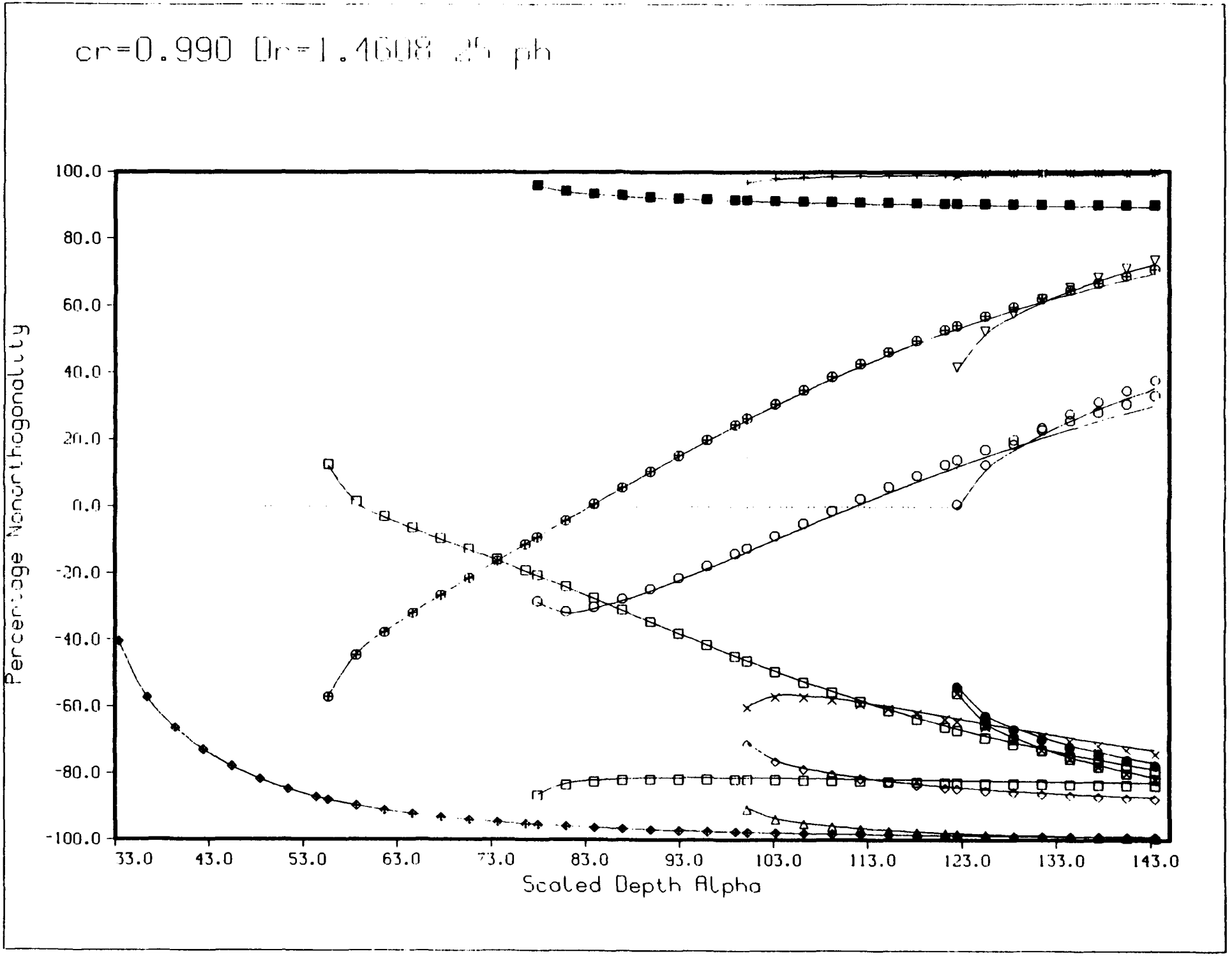
cr=0.990 Dr=1.4608
100.0
80.0
60.0
40.0
20.0
0.0
-20.0
-40.0
-60.0
-80.0
-100.0
Percentage Nonorthogonality
33.0
43.0
53.0
63.0
73.0
83.0
93.0
103.0
113.0
123.0
133.0
143.0
Scaled Depth Alpha

Fig. 25

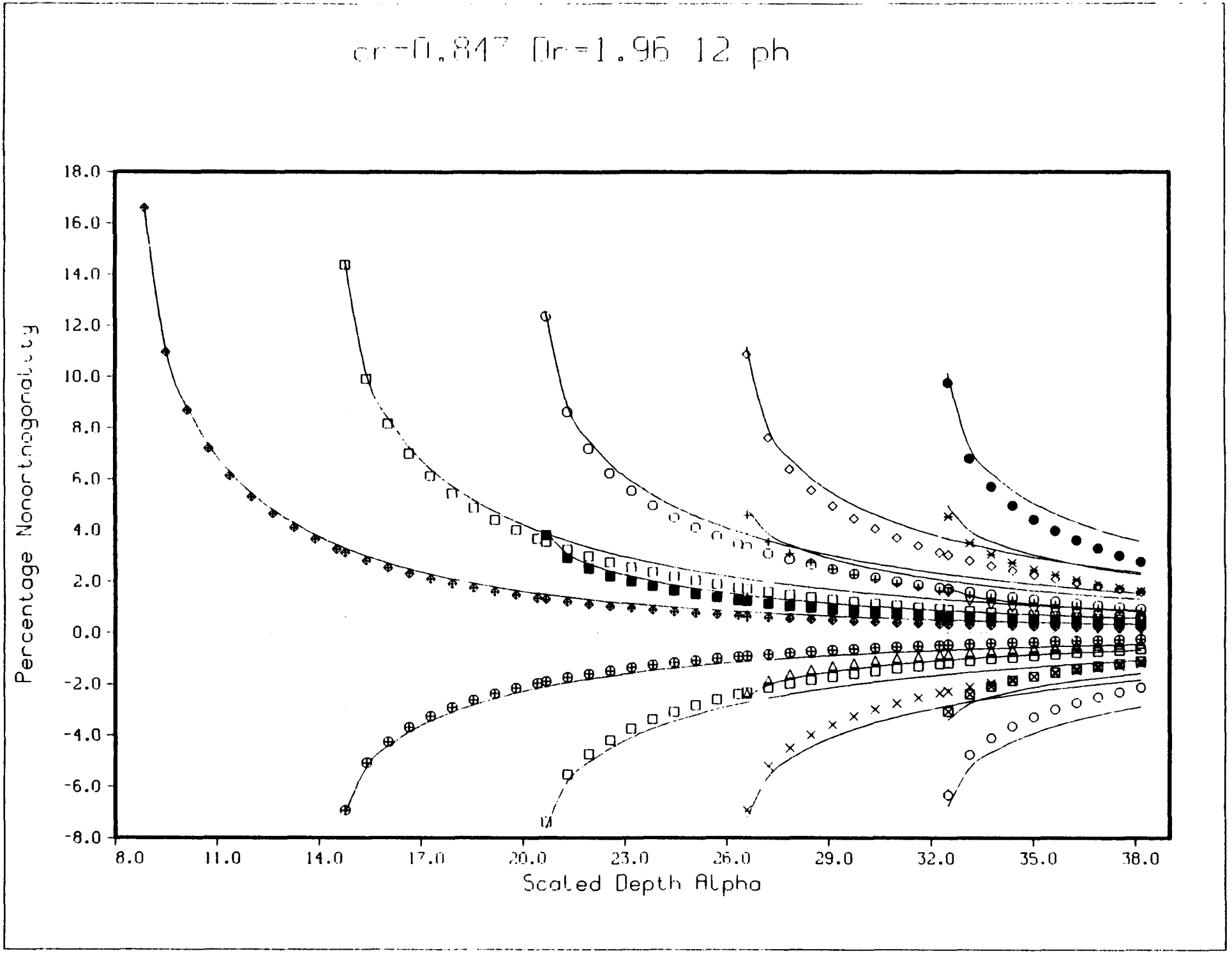
cr=0.847 Dr=1.96 12 ph
Percentage Nonorthogonality
18.0
16.0
14.0
12.0
10.0
8.0
6.0
4.0
2.0
0.0
-2.0
-4.0
-6.0
-8.0
8.0
11.0
14.0
17.0
20.0
23.0
26.0
29.0
32.0
35.0
38.0
Scaled Depth Alpha

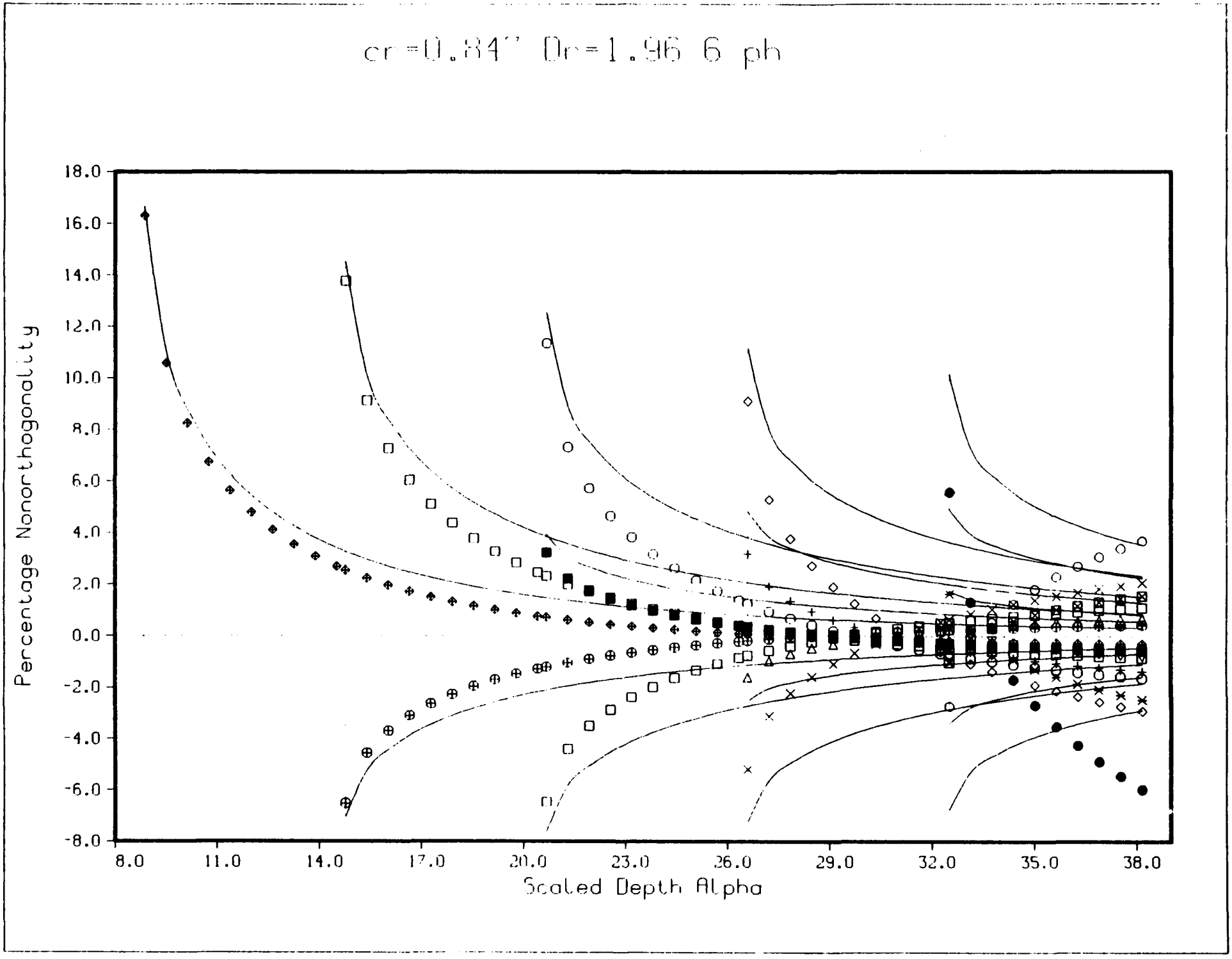
cr=0.84" Dr=1.96 6 ph
Percentage Nonorthogonality
18.0
16.0
14.0
12.0
10.0
8.0
6.0
4.0
2.0
0.0
-2.0
-4.0
-6.0
-8.0
8.0
11.0
14.0
17.0
20.0
23.0
26.0
29.0
32.0
35.0
38.0
Scaled Depth Alpha

THE UNIVERSITY OF SOUTHERN MISSISSIPPI

PHYSICS & ASTRONOMY

December 19, 1988

-COPY-

Dr. Anas M. Abo-Zena
Code 244
Building 1005
NORDA
Stennis Space Center, MS 39529

Dear Dr. Abo-Zena:

Transmitted herewith is the final report on the supplement to the University of Southern Mississippi subcontract to the NORDA contract with the University of New Orleans number N00014-87-K6002. This report is an analysis of the literature on scattering and reverberation from wedges in ocean acoustics. As the report explains, a thorough literature search was done and the five most important papers were analyzed and reported. I have not analyzed your own two papers which make significant contributions to the field because I do not wish to put myself in the uncomfortable position of presuming to explain an author's own paper to the man himself! Although I believe the report to be full and complete, I will, of course, be happy to try to answer any questions you may have. The official report will be submitted through the University of New Orleans as part of their final report on the entire contract. I have informed their Principal Investigator that I was sending a copy of my supplemental report directly to you as well as to him.

Thank you again for the opportunity of working with you and I look forward to future collaborations.

Yours sincerely,

Grayson H. Rayborn
Professor of Physics & Astronomy

Southern Station • Box 5046 • Hattiesburg, Mississippi • 39406 5046 • (601)266 4934

INTRODUCTION

As a supplement to the University of Southern Mississippi subcontract from the Univeristy of New Orleans (Board of Supervisors of Louisiana State University and Agricultural and Mechanical College) of their NORDA Contract N00014-87-K6002, a study of the literature of reverberation and scattering from wedges on the ocean bottom was performed. The Principal Investigator for the University of Southern Mississippi was Grayson H. Rayborn, Professor of Physics and Astronomy. The work was performed during the summer of 1988.

IDENTIFICATION OF RELEVANT LITERATURE

The literature relevant to scattering and reverberation from wedges on the ocean bottom was identified by performing a keyword search at the Maury Library at Stennis Space Center. The search was conducted on the words: "wedge", "ocean", and "underwater acoustics". The resulting citations were studied and additional literature of the author's own personal knowledge was also studied. Of course, relevant citations in these papers were also checked until no new references were found. Thus, the study should be

reasonably complete, although only the five most important papers are analyzed in this report. The form of this report will be first to review the important papers in detail, and then to assess the present understanding of scattering and reverberations from wedges on the ocean bottom as expressed in the literature, and finally to suggest possible areas and ideas for fruitful continued study.

REVIEW AND ANALYSIS OF RELEVANT LITERATURE

1) F. B. Jensen and W. A. Kuperman, "Sound propagation in a wedge-shaped ocean with a penetrable bottom", Journal of the Acoustical Society of America 67(5), 1564-1566 (May 1980).

This paper utilizes a parabolic equation (PE) method to investigate the propagation of sound from a point source, modeled as a gaussian beam in the PE code, across a constant depth ocean into an ocean sloping upward at 1.55°. A single frequency source was used to create three propagating normal modes which disappeared at depths predicted by normal mode theory, propagating into the bottom as beams. These results agree with tank experiments (Coppens and

Sanders 1978) when the geometry is scaled by the acoustical wavelength (Coppens and Sanders used f = 150 kHz), except that experiment showed that the measured beam angle as the modes disappeared into the bottom was 20 to 30% lower than the asymptotic theory, stationary phase angle predicted. Also, the measured beam angle was approximately 20% higher than that predicted by the PE model, probably due to the fact that the critical angle in the experiment was approximately 28°, while their PE model is designed to handle forward angles only as great as 20°.

The important points disclosed by this article are:

a) A PE model can predict the main features of up-slope propagation including cut-off depths and radiation into the bottom;
b) Radiation into the bottom is the principal energy loss mechanism; there is little energy converted into the next lower mode;
c) Thus, mode coupling theories must include coupling to the continuum if they are to be at all realistic.

2) M. J. Buckingham, "Acoustic Propagation in a Wedge-Shaped Ocean with Perfectly Reflecting Boundaries", NRL Report 8793, March 19, 1984; 23 pages.

As the title indicates, this paper presents a solution for the acoustic field produced by a point source in a wedge-shaped ocean with perfectly reflecting, i. e., pressure-release, boundaries. The solution is presented in the form of a sum of normal modes and it correctly reduces in the vicinity of the point source to the free-field solution for a point source. Interestingly, the radiation field associated with each normal mode forms a well-defined beam which diverges as the energy propagates out towards deep water. This paper also demonstrates the formation of shadow zones outside the beam where there is essentially no energy in the mode. The modes are well-ordered with the inner beam having the highest mode number and the outer beam the lowest mode number so that the spatial extent of the sound field in a direction parallel to the shore line is determined by the

lowest order mode which is propagating. The author demonstrates that, to a good approximation, the number of propagating modes is the integer number of half-wavelengths of the sound contained in the depth of water at the source or receiver, whichever is shallower. In addition to a normal mode integral, this paper approximates the normal mode integral accurately as the weighted sum of Hankel functions of the first and second kind (whose order is the mode number), a form which is applicable to most situations encountered in ocean acoustics. Further, the paper demonstrates that another popular approximation to the integral (D. L. Bradley and A. A. Hudimac "The Propagation of Sound in a Wedge Shaped Shallow Duct", Naval Ordinance Laboratory Report NOLTR 70-235, Nov. 1970) is inapplicable precisely in the region of most interest to underwater ocean acoustics, when the receiver is less than ten times the distance of the sound source from the shoreline. The paper concludes by interpreting the modal beams as rays, with a criterion for determining when a ray may correspond to a mode: "the grazing angle of the ray at the vertex of its hyperbolic path must be the same as

that of the ray corresponding to the m^{th} mode in shallow water whose depth is equal to the depth at vertex". Finally, a simple, physical argument for the existence of shadow zones is given.

The principal question raised by this paper is how the solution can be extended to a more realistic case for ocean acoustics in which the bottom surface is treated as penetrable rather than perfectly reflecting (pressure release boundary). The solution presented in this paper is valid because the Helmholtz equation for a wedge is separable when both wedge surfaces are pressure release. The Helmholtz equation is not separable when one of the boundaries is penetrable. The challenge left by this paper is, then, to extend the work to an interesting, realistic model for ocean acoustics. It should also be noted that the solutions given are applicable only to certain angles; namely, those which are integral sub-multiples of pi radians.

3) Stewart A. L. Glegg and Jong R. Yoon, "Experimental measurements of 3-dimensional propagation in a

wedge-shaped ocean with pressure release boundary conditions", (submitted to the Journal of the Acoustical Society of America.)

These experiments were done to check the theoretical analysis of Buckingham presented in NRL Report 8793 and discussed in the previous paragraph of this report. The experiments were performed by immersing a plexiglas tank prismatic in shape and filled with air in a larger tank which is itself filled with water. The wedge angle, then, becomes the angle between the top of the plexiglas tank and the horizontal surface of the water. Adjustment of the cables which restrained the buoyant plexiglas tank then permitted variation in the water wedge angle. The wedge model in this experiment has a pressure release bottom and slope and a wedge angle of about 20 degrees. For simplicity of analysis only the lowest mode is excited by locating the source near the cut off range. The acoustic field from a point source in the wedge domain was measured at several different frequencies and for different wedge angles and good agreement with the theoretical model was found. The wedge angles were between one-tenth pi,

or 18°, and one-eighth pi, or 22,5°. Although large variations in sound level, on the order of 10 dB, were found for small changes in wedge angle, subsequent analysis showed that the measurement were consistent with a linear variation between the sound levels predicted by Buckingham at angles which were sub-multiples of pi radians. It was found that for downslope propagation, the spatial characteristics of the field in a direction parallel to the shore line are in good agreement with the theoretical solution of Buckingham's and that the azimuthal extent of the beam does depend on the wedge angle as predicted. Shadow zones were also found as predicted. Errors were in the range of 1.5 dB except in the shadow zones were low signal-to-noise ratios caused the errors to jump to about 3 dB. In addition to verifying Buckingham's theory, the paper also gives measurements of pulse propagation and distortion in the wedge.

The significance of this paper is that it experimentally confirms the predictions of the Buckingham theory including shadow zones and the spatial extent of the modal beams and demonstrates

that the theory can indeed be extended to angles which are not sub-multiples of pi by simple, linear interpolation.

4) M. J. Buckingham, "Theory of Three-Dimensional Acoustic Propagation in a Wedgelike Ocean with a Penetrable Bottom", Journal of the Acoustical Society of America 82(1), (1987).

This paper extends Buckingham's previous results for a pressure release bottom in a wedge-shaped ocean to a penetrable bottom in the same geometry in an approximate fashion. The approximation depends on the fact that the oscillating modal functions which do not, of course, reach a node at a penetrable bottom the way they do at a perfectly reflecting bottom, do approximately reach nodes some distance below the penetrable bottom, and the distance is the same for all modes. The distance below the bottom at which the nodes form depends in a systematic way on the character of the bottom. Buckingham's application of this "common node theory" to the wedge problem permits him to approximate the wedge

by another one of the same wedge angle but displaced so that its apex is farther from the sound source.

The importance of this paper is that it suggests a means of extending the theory of propagation in an infinite wedge, albeit in only an approximate fashion, to the realistic case of a penetrable bottom.

5) Herman Medwin, Emily Childs, Edgar A. Jordon, and Robert A. Spaulding, Jr., "Sound scatter and shadowing at a seamount: Hybrid physical solutions in two and three dimensions", Journal of the Acoustical Society of America 75(5), 1478-1490(1984).

Previous measurements, theories, and discussions of sound propagating in ocean wedges have assumed that the wedge was infinite in horizontal extent and that the bottom eventually met the ocean surface. Although these are reasonable assumptions to make when studying the transmission of sound near a constantly sloping shoreline, this model is of questionable validity when applied to seamounts

which are finite in horizontal extent and which may never reach the surface of the sea. This paper attempts the more difficult problem of predicting scattering and diffraction from a seamount. The particular object of study is the Dickins Seamount in the Northeast Pacific Ocean (54°32'N, 136°55'W). This paper provides scale model experiments and computer experiments to explain the results of ocean measurements over this Dickins Seamount reported by G. R. Ebbeson and R. G. Turner in J. Acoust. Soc. Am. 73, 143-152 (1983) and N. R. Chapman and G. R. Ebbeson in J. Acoust. Soc. Am. 73, 1979-1984 (1983). Three approximations to the actual seamount were used in the laboratory scale model experiments. A simple plane wedge, a contour wedge in which slopes vary along the wedge to express general contour features of the Dickins Seamount, and a realistic scale model based on a a detailed bathymetric survey by the Defense Research Establishment Pacific. In these laboratory measurements the contour wedge produced results in somewhat better agreement with the ocean measurements than did the simple wedge. Neither, however, was sufficiently accurate so as to provide a useful model. The authors concluded that

"...a three-dimensional wave solution is essential for correct modeling of the effect of Dickins Seamount." The authors also compared propagation loss measured in the ocean trials under specified conditions to be 97 $\pm$ 5 dB with their own hybrid model of seamount propagation in which they incorporate the wave phenomena of forward scatter at the upslope of the seamount followed by diffraction and reradiation over the crest. The hydbrid model identified three contributions to propagation loss: (1) upslope forward scattering loss, (2) diffraction loss, and (3) an additional refraction loss for the new path from the seamount to the receiving hydrophone. The hybrid model also predicts that diffraction loss is proportional to the square root of the frequency, a conclusion which appears to be supported by the ocean measurements.

Finally, this paper reports computer experiments on three models of the seamount. All models treat the seamount as rigid since, as a relatively new seamount, the Dickins Seamount has slopes containing only a very thin sedimentary deposit. Computer Model 1 calculated the diffraction loss using a two-dimensional double diffraction technique treating

the wedge as a wide contour wedge barrier with two changes of slope. Comparision with the laboratory experiments of these computer calculations showed good to excellent agreement. Model 2 naively assumed that the crest of the three-dimensional seamount is where most of the major changes of slope occur and that the crest may be approximated by crestal line segments of finite length. This model gave results for diffraction strength that were a dB or two better than those yielded by the simple wedge model in laboratory experiments. However, this crestal segment model still gave diffraction strength results that were about 10 dB too high. Therefore, this model is too naive to be useful. Model 3 used accurate changes of slope along the track between source and receiver, but did not properly account for the topography one either side of the direct track. Each time the slopes were estimated and diffraction strength calculated, the results were within 2 or 3 dB of each other and always about 2 or 3 dB too high. The clear conclusion of the computer model experiments was that the double diffraction technique permits accurate computer calculations of the diffraction

loss in the shadow of a two-dimensional seamount and approximate predictions for the three-dimensional body. The overall conclusions of the authors was that hybrid laboratory and computer models could give accurate estimates of diffraction loss and shadowing by the Dickins Seamount for sound sources from 50 to 500 Hz, that the shadow loss varies as the square root of the frequency, and that the three-dimensional diffracted signal is significantly different from the two-dimensional signal.

CONCLUSION

Most of the theories and data on diffraction of acoustic waves by wedges treat the wedges as infinite in extent. This model appears to be useful in studies of sound propagation near shores. The use of common node theory apparently permits the extension of this theory to penetrable bottoms in a straight forward, although approximate, manner. The experimental verification of the theory for the infinite wedge with pressure release boundaries gives great confidence that the theory should accurately describe sound propagation in the ocean near gently sloping beaches. Optimum processing

techniques remain to be worked out both for detection and for range and depth localization. The extension of shallow water, rectangular wave guide matched field processing techniques to the wedge should certainly prove challenging, and might decisively determine whether modal processing is superior to conventional processing. Signal estimation in this field would also profit from determination of the non-orthogonality of the modal functions for wedges with various bottoms as they have been determined by Rayborn, G. Ioup, and J. Ioup for the rectangular problem.

However, the work of Medwin et al suggests that the theory of propagation in an infinite wedge is of only limited utility in describing the diffraction over and around a finite, wedge-like seamount. Their work also indicates that reasonable prediction of the effect of such seamounts on propagation loss and their shadowing may be made if detailed laboratory models and extensive computer simulations are made.

In conclusion, then, the problem of propagation past wedge-shaped seamounts is a difficult one, and much work remains to be done in this field if general inferences about the effect of such seamounts on acoustic propagation are to be made.